

**Investigation of Near Field Effects on Retrieval of
Electromagnetic Properties of Chiral
Metamaterials and Coupling Effects of Nearby
Metamaterials**

**Ph.D. Thesis
in
Electrical and Electronics Engineering
Gaziantep University**

**Supervisor
Prof. Dr. Uğur Cem HASAR**

**By
Musa BUTE
December 2018**



© 2018 [Musa BUTE]

REPUBLIC OF TURKEY
GAZIANTEP UNIVERSITY
GRADUATE SCHOOL OF
NATURAL AND APPLIED SCIENCES
ELECTRICAL AND ELECTRONICS ENGINEERING

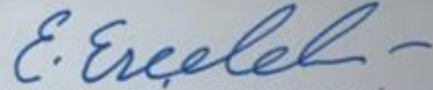
Name of the Thesis : Investigation of Near Field Effects on Retrieval of Electromagnetic Properties of Chiral Metamaterials and Coupling Effects of Nearby Metamaterials
Name of the Student : Musa BUTE
Exam Date : 21.12.2018

Approval of the Graduate School of Natural and Applied Sciences.



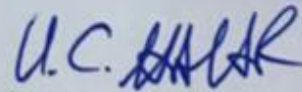
Prof. Dr. Ahmet Necmeddin YAZICI
Director

I certify that this thesis satisfies all the requirements as a thesis for the degree of Doctor of Philosophy.



Prof. Dr. Ergun ERÇELEBİ
Head of Department

This is to certify that we have read this thesis and that in our opinion it is fully adequate, in scope and quality, as a thesis for the degree of Doctor of Philosophy.



Prof. Dr. Uğur Cem HASAR
Supervisor

Examining Committee Members:

Prof. Dr. Gölge ÖĞÜCÜ YETKİN

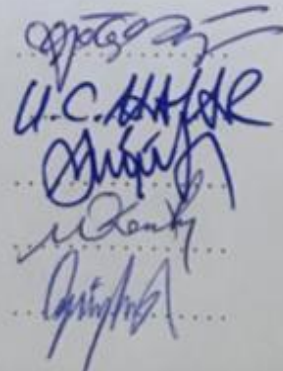
Prof. Dr. Uğur Cem HASAR

Assoc. Prof. Dr. Kemal DELİHACIOĞLU

Assoc. Prof. Dr. Muharrem KARAASLAN

Asst. Prof. Dr. Oğuzhan AKGÖL

Signature



I hereby declare that all information in this document has been obtained and presented in accordance with academic rules and ethical conduct. I also declare that, as required by these rules and conduct, I have fully cited and referenced all material and results that are not original to this work.

Musa BUTE

ABSTRACT

INVESTIGATION OF NEAR FIELD EFFECTS ON RETRIEVAL OF ELECTROMAGNETIC PROPERTIES OF CHIRAL METAMATERIALS AND COUPLING EFFECTS OF NEARBY METAMATERIALS

BUTE, Musa

Ph.D. in Electrical and Electronics Engineering

Supervisor: Prof. Dr. Uğur Cem HASAR

December 2018

102 pages

For accurate retrieval of electromagnetic properties of metamaterials (MMs), two subjects have been investigated throughout this thesis. The first subject involves a robust and accurate retrieval method for chiral MMs by taking into account the near-field effects which might be present around the borders of MMs due to high order Bloch modes. The second subject is about investigation of coupling phenomenon between nearby and adjacent MM slabs via considering substrate loss. Toward this end, to achieve investigated two subjects first the fundamental characteristics of chiral MMs are introduced. Then, classification of bi-isotropic media was described and the concept of chirality properties was clarified in detail. Next, the importance of near-field effects for chiral MMs was discussed. Moreover, the special properties of chiral MMs which are circular dichroism and optical activity were demonstrated. Furthermore, a new type of crescent-shaped chiral MM configuration was proposed in the framework of our analysis. In order to check the properties of crescent-shaped MM structure, different U-shaped and cross-shaped chiral configurations commonly utilized in the literature have been examined for comparison. On the other hand, to validate the coupling phenomenon between the resonating MM slabs, a conventional dielectric sample (polyethylene-nonresonant) was first considered. Then, the effect of distance between the resonating MM slabs and the effect of loss inside substrate on the strength of coupling effects were examined. Simulations were performed by CST-Microwave Studio at X-band (8.12 - 12.4 GHz) to support our analysis.

Key words: Chiral metamaterial, near-field effects, crescent shaped, chirality, dichroism, optical-activity, coupling analysis.

ÖZET

KİRAL METAMALZEMELERİN ELEKTROMANYETİK ÖZELLİKLERİNİN BELİRLENMESİNDE SINIR ETKİLERİNİN VE BİRBİRİNE KOMŞU OLAN METAMALZEMELERDE KUPLAJ ETKİSİNİN İNCELENMESİ

BUTE, Musa

Doktora Tezi, Elektrik ve Elektronik Mühendisliği Bölümü

Tez Yöneticisi: Prof. Dr. Uğur Cem HASAR

Aralık 2018

102 sayfa

Bu tezde metamalzemelerin elektromanyetik özelliklerinin düzgün ve doğru olarak belirlenmesi için iki konu incelenmiştir. Birincisi, kiral metamalzemelerin sınırlarındaki yüksek seviye Bloch modlar nedeniyle oluşan yakın alan etkilerini dikkate alıp, elektromanyetik parametrelerinin çıkarımını yapan güçlü bir yöntemi içermektedir. İkincisi ise metamalzeme alt taşının kaybı dikkate alınarak bitişik veya yakın olan metamalzemeler arasındaki kuplaj etkisi analiz edilmiştir. Bu doğrultuda, bu iki analizin başarılması için metamalzemelerin temel özellikleri hakkında bilgiler verilmiştir ve özellikle de kiral metamalzemelerin karakteristiği sunulmuştur. Bununla birlikte, bi-isotropik malzemelerin sınıflandırılması tanımlanmıştır ve kiral malzemelerin konsepti detaylı bir şekilde tartışılmıştır. Sonra, kiral metamalzemelere has çembersel dikroizm ve optiksel aktivite özellikleri gösterilmiştir. Ayrıca, bu tez çerçevesi kapsamında hilal şekilli yeni bir kiral metamalzeme konfigürasyonu önerilmiştir ve bu hilal şekilli metamalzemenin özellikleri literatürde iyi bilinen ve yaygın olan U-şekilli ve kros-şekilli kiral metamalzemelerle karşılaştırılıp, sınanmıştır. Diğer yandan, rezonatör metamalzemeler arasındaki kuplaj etkisini göstermek için ilk önce normal dielektrik (polietilen-rezonansız) bir malzeme ile doğrulanmıştır. Sonrada, metamalzeme hücreleri arasındaki mesafe ve dielektrik alt taşının kaybı dikkate alınarak kuplaj etkisinin seviyeleri analiz edilmiştir. Yaptığımız çalışmaları desteklemek için CST-Mikrodalga kütüphanesi kullanılarak X-bandında (8.2-12.4GHz) benzetimler yapılmıştır.

Anahtar kelimeler: Kiral metamalzemeler, değişken sınır etkileri, hilal şekilli, kiralite, dikroizm, optik-aktivite, kuplaj analizi.



To my family...

ACKNOWLEDGEMENTS

Firstly, I would like to express my best wishes to my supervisor Prof. Dr. Uğur Cem HASAR, for his guidance, advice, understandings, encouragements, and criticism throughout this study.

I also wish to thank most sincerely to my family especially to my wife for her patience and support during my studies.

This work also was supported by TÜBİTAK - ARDEB under the Project Number 112R032 and 114E495. In addition, financial support for buying CST simulation software was given by TÜBİTAK through 112R032 and 114E495 projects.

Finally, I acknowledge Technological Research Council of Turkey (TÜBİTAK) - BİDEB for supporting my studies with scholarship number 2211-C.

TABLE OF CONTENTS

	Page
ABSTRACT	v
ÖZET	vi
ACKNOWLEDGEMENTS	viii
TABLE OF CONTENTS	ix
LIST OF TABLES	xii
LIST OF FIGURES	xiii
LIST OF SYMBOLS	xix
CHAPTER 1	1
INTRODUCTION	1
1.1 Background and Scope of Study	1
1.2 Literature Review and Motivation of Thesis	3
CHAPTER 2	7
METAMATERIALS	7
2.1 Classification of Metamaterials	8
2.1.1 Double Positive Materials (DPS)	9
2.1.2 Single Negative (SNG) Media only $\epsilon < 0$ or $\mu < 0$	10
2.1.3 ENG - Metamaterials $\epsilon < 0$	11
2.1.4 MNG - Metamaterials $\mu < 0$	12
2.1.5 Double Negative (DNG) Media $\epsilon < 0$ and $\mu < 0$	14
2.2 Background on Classical Field Theory of Electromagnetism	15
2.2.1 Vacuum Medium Case	15
2.2.2 Presence of Matter Case	16
2.3 Retrieval Method for Chiral Materials	19

2.3.1	Wave Propagation in Chiral Medium	19
2.3.2	Retrieval Parameters for Chiral Medium	22
2.3.3	Alternative Retrieval Algorithm for Chiral Materials	25
CHAPTER 3	27
ANALYSIS OF NEAR-FIELD EFFECTS FOR CHIRAL META-		
MATERIALS SLABS	27
3.1	Introduction	27
3.2	Theoretical Analysis of Chiral MMs with Near-Field Effects	29
3.3	Validation and Simulation	33
3.4	Discussion on Results of Near-Field Effects	35
CHAPTER 4	43
CHARACTERIZATION AND REALIZATION OF CHIRAL META-		
MATERIALS	43
4.1	Introduction	43
4.2	Investigation of U-shaped, Cross-shaped and Crescent-shaped Chiral MM	44
4.2.1	Sample 1: U-shaped Chiral MM	45
4.2.2	Sample 2: Cross-shaped Chiral MM	46
4.2.3	Sample 3: Crescent-shaped Chiral MM	47
4.3	Characterization of Chiral MM	48
4.3.1	Forward Transmission Coefficients (S_{21}) of Chiral Medium	48
4.3.2	Backward Transmission Coefficients (S_{12}) of Chiral Medium	50
4.3.3	Forward Reflection Coefficients (S_{11}) of Chiral Medium	50
4.3.4	Backward Reflection Coefficients (S_{22}) of Chiral Medium	53
4.3.5	Azimuth Rotation Angle (θ) of Chiral Medium	54
4.3.6	Elliptical Angle (η) of Chiral Medium	54
4.3.7	Chirality Constant (κ) of Chiral Medium	57
4.3.8	First Reflection Coefficient (Γ) of Chiral Medium	57
4.3.9	Impedance (Z) of Chiral Medium	60

4.3.10	Refractive Index for RCP Waves (n_+) of Chiral Medium	60
4.3.11	Refractive Index for LCP Waves (n_-) of Chiral Medium	63
4.3.12	Refractive Index (n) of Chiral Medium	63
4.3.13	Permittivity (ϵ) of Chiral Medium	66
4.3.14	Permeability (μ) of Chiral Medium	66
CHAPTER 5	69
COUPLING EFFECT OF NEARBY RESONATING METAMA-		
TERIAL SLABS	69
5.1	Introduction	69
5.2	Theory of Coupling Analysis	72
5.3	Computational Analysis of Coupling Analysis	76
5.3.1	Geometrical and Electrical Properties of Slabs	76
5.3.2	Simulation Details	78
5.3.3	Simulation Results	78
CHAPTER 6	87
CONCLUSIONS AND FUTURE STUDIES	87
6.1	Conclusions	87
6.1.1	Comments on Analysis of Near Field Effects for Chiral Metamaterials	89
6.1.2	Comments on Analysis of Coupling Effect of Nearby Res- onating Metamaterial Slabs	89
6.2	Future Studies	90
REFERENCES	92

LIST OF TABLES

	Page
Table 2.1 Classification of Bi-isotropic Materials	18



LIST OF FIGURES

		Page
Figure 2.1	Diagram of classification of materials depending on the permeability and permittivity values [60].	8
Figure 2.2	Configuration of conventional refraction when the both medium is DPS media [60].	9
Figure 2.3	At optical and infrared frequency ranges the noble metals behave as ENG-materials for certain frequency regions [61].	10
Figure 2.4	ENG-Structure consist of parallel long thin metal wires periodically aligned with radius r and a lattice period a [62].	11
Figure 2.5	The first proposed unit cell of the SRR to achieve MNG-Structure in round shape [60].	12
Figure 2.6	The first proposed unit cell of the SRR to achieve MNG-Structure in square shape [60].	13
Figure 2.7	Unit cell of alternative MNG-structures (a) in spiral and (b) S-shaped resonator [60].	13
Figure 2.8	Configuration of refraction when the first medium is DPS media and the second medium is DNG media (both $\epsilon < 0$ and $\mu < 0$) [60].	14
Figure 2.9	Schematics for the transmission and reflection properties of a chiral MM slab for a plane wave incidence.	22
Figure 3.1	Investigated chiral MM slab for near-field effect analysis involving semi-infinite transmission and reflection and S-parameters.	29

Figure 3.2	Simulated geometrical properties of investigated configuration for the Teflon sample in CST.	33
Figure 3.3	Simulated geometrical properties of analyzed configuration for the chiral MM cell with U-shaped split-ring-resonators.	34
Figure 3.4	Magnitudes of simulated forward and backward reflection and transmission S-parameters of the Teflon sample with length $L_1 = 1.00$ mm.	35
Figure 3.5	Magnitudes of simulated forward and backward reflection and transmission S-parameters of the Teflon sample with length $L_1 = 2.00$ mm.	36
Figure 3.6	Magnitudes of simulated forward and backward (a) transmission and (b) reflection S-parameters of the chiral MM slab with length of $L_1 = 50$ mm (5 cells).	37
Figure 3.7	Magnitudes of simulated forward and backward (a) transmission and (b) reflection S-parameters of the chiral MM slab with length of $L_1 = 60$ mm (6 cells).	38
Figure 3.8	Extracted Γ_1 (proposed), Γ_2 (proposed), and Γ [36] of the Teflon sample by using our method and the method in [36]: (a) Real part, (b) Imaginary part and (c) Magnitude.	40
Figure 3.9	Extracted Γ_1 (proposed), Γ_2 (proposed), and Γ [36] of the chiral MM slab or $L_1 = 50$ mm (5 cell) and $L_2 = 60$ mm (6 cell) by using our method and the method in [36]: (a) Real part and (b) Imaginary part.	41
Figure 3.10	Magnitudes of chiral MM slab by using our method and the method in [36] (a) Γ_1 (proposed) and Γ [36] and (b) Γ_2 (proposed) and Γ [36].	42
Figure 4.1	Geometrical properties of the examined chiral MM cell with U-shaped split-ring-resonators [37].	45

Figure 4.2	Geometrical properties of the analyzed chiral MM cell with cross-shaped split-ring-resonators [38].	46
Figure 4.3	Geometrical properties of analyzed configurations for the chiral MM cell with crescent-shaped split-ring-resonators (a) front view and (b) perspective view [41].	47
Figure 4.4	Simulated absolute forward transmission coefficients for the configuration of (a) U-shaped, (b) Cross-shaped and (c) Crescent-Shaped.	49
Figure 4.5	Simulated absolute backward transmission coefficients for the configuration of (a) U-shaped, (b) Cross-shaped and (c) Crescent-Shaped.	51
Figure 4.6	Simulated absolute forward reflection coefficients for the configuration of (a) U-shaped, (b) Cross-shaped and (c) Crescent-Shaped.	52
Figure 4.7	Simulated absolute backward reflection coefficients for the configuration of (a) U-shaped, (b) Cross-shaped and (c) Crescent-Shaped.	53
Figure 4.8	Simulated optical activity of azimuth rotation angle for the configuration of (a) U-shaped, (b) Cross-shaped and (c) Crescent-Shaped.	55
Figure 4.9	Simulated elliptical angle of circular dichroism for the configuration of (a) U-shaped, (b) Cross-shaped and (c) Crescent-Shaped.	56
Figure 4.10	Simulated real value of chirality parameter $\Re(\kappa)$ for the configuration of (a) U-shaped, (b) Cross-shaped and (c) Crescent-Shaped.	58
Figure 4.11	Simulated magnitude of first reflection coefficient $ \Gamma $ for the configuration of (a) U-shaped, (b) Cross-shaped and (c) Crescent-Shaped.	59

Figure 4.12	Simulated impedances Z for the configuration of (a) U-shaped, (b) Cross-shaped and (c) Crescent-Shaped.	61
Figure 4.13	Simulated real value of refractive index for RCP waves $\Re(n_+)$ for the configuration of (a) U-shaped, (b) Cross-shaped and (c) Crescent-Shaped.	62
Figure 4.14	Simulated real value of refractive index for LCP waves $\Re(n_-)$ for the configuration of (a) U-shaped, (b) Cross-shaped and (c) Crescent-Shaped.	64
Figure 4.15	Simulated real value of refractive index $\Re(n)$ for the configuration of (a) U-shaped, (b) Cross-shaped and (c) Crescent-Shaped.	65
Figure 4.16	Simulated real value of relative permittivity $\Re(\epsilon)$ of chiral medium for the configuration of (a) U-shaped, (b) Cross-shaped and (c) Crescent-Shaped.	67
Figure 4.17	Simulated real value of relative permeability $\Re(\mu)$ of chiral medium for the configuration of (a) U-shaped, (b) Cross-shaped and (c) Crescent-Shaped.	68
Figure 5.1	(a) A composite structure with two cascaded slabs, (b) its S-parameter equivalent, and (c) its ABCD parameter equivalent [81].	72
Figure 5.2	(a) Configuration of principal axis and geometry of a MM (split-ring-resonator-SRR) unit cell and field directions and propagation vector \bar{k} . $L_m = 2.00$ mm, $w = g = 0.30$ mm, $u_y = u_z = 2.54$ mm, $u_x = 2d + t_m$, $t_m = 35\mu\text{m}$ (metallization thickness), and $d = 1.615$ mm (substrate thickness) and (b) a MM slab composed of 4×7 unit cells within the cross section of X-band waveguide ($a = 22.86$ mm and $b = 10.16$ mm) [81].	77

Figure 5.3 (a) Simulated (Sim) and calculated (Cal) $|S_{11}^{3T}|$, $|S_{21}^{3T}|$, $|S_{12}^{3T}|$, and $|S_{22}^{3T}|$ and (b) extracted $|S_{11}^{(c)}|$, $|S_{21}^{(c)}|$, $|S_{12}^{(c)}|$, and $|S_{22}^{(c)}|$ for cascaded two polyethylene slabs with overall length $2L_d$. Solid blue and dashed red curves show simulated and calculated dependencies, respectively. In calculation, we used $S_{11}^{(c)} = S_{22}^{(c)} = 0$ and $S_{21}^{(c)} = S_{12}^{(c)} = 1$ [81]. 79

Figure 5.4 Simulated (a) $|S_{11}^{(1)}|$, $|S_{21}^{(1)}|$, $|S_{12}^{(1)}|$, and $|S_{22}^{(1)}|$ and (b) $|S_{11}^{3T}|$, $|S_{21}^{3T}|$, $|S_{12}^{3T}|$, and $|S_{22}^{3T}|$ of the 4×7 MM slab with different substrate losses. Solid and dashed curves denote S-parameters for $\delta_s = 0.025$ and $\delta_s = 0.005$, respectively [81]. 81

Figure 5.5 (a) Simulated (Sim) and calculated (Cal) $|S_{11}^{3T}|$, $|S_{21}^{3T}|$, $|S_{12}^{3T}|$, and $|S_{22}^{3T}|$ for cascaded two 4×7 MM slabs ($\delta_s = 0.025$) [In the calculation, we used $S_{11}^{(c)} = S_{22}^{(c)} = 0$ and $S_{21}^{(c)} = S_{12}^{(c)} = 1$], and (b) extracted $|S_{11}^{(c)}|$, $|S_{21}^{(c)}|$, $|S_{12}^{(c)}|$, and $|S_{22}^{(c)}|$ for cascaded two 4×7 MM slabs ($\delta_s = 0.025$) [81]. 82

Figure 5.6 (a) Magnitude of magnetic field intensity over the SSRs for a cascade connection of two 4×7 MM slabs [Here, the dependencies are recorded when the highest field value is observed at resonance frequency 10.485 GHz. Red and blue colors on the color bar denote maximum (0 dB A/m) and minimum values (-40 dB A/m)], and (b) simulated (Sim) and calculated (Cal) $|S_{11}^{3T}|$, $|S_{21}^{3T}|$, $|S_{12}^{3T}|$, and $|S_{22}^{3T}|$ for (a) cascaded two 4×7 MM slabs ($\delta_s = 0.025$) when the slabs are separated by a 12 mm distance (filled by a FR4 sample) [Solid and dashed curves show simulated and calculated dependencies, respectively. In the calculation, we used $S_{11}^{(c)} = S_{22}^{(c)} = 0$ and $S_{21}^{(c)} = S_{12}^{(c)} = 1$] [81]. 84

Figure 5.7 Extracted $|S_{11}^{(c)}|$, $|S_{21}^{(c)}|$, $|S_{12}^{(c)}|$, and $|S_{22}^{(c)}|$ for cascaded two 4×7 MM slabs ($\delta_s = 0.025$) when the slabs are separated by (a) a 12 mm distance (filled by a FR4 sample) and (b) a 4 mm distance (filled by a FR4 sample) [81]. 86



LIST OF SYMBOLS

MM : Metamaterials
SRR : Split-Ring-Resonator
LHM : Left Handed Material
RHM : Right Handed Material
LCP : Left Circularly Polarized
RCP : Right Circularly Polarized
DNG : Double Negative
DPS : Double Positive
ENG : Epsilon Negative
SNG : Single Negative
MNG : Mu Negative
NIM : Negative Index Material
TRL : Thru-Reflect-Line
SOLT : Short-Open-Load-Thru
TRM : Thru-Reflect-Match
S- : Scattering
CST : Computer Simulation Technology
ABCD : Transmission Matrix
WCM : Wave Cascading Matrix
SGF : Signal Graph Technique

\vec{E} : Electric Field
 \vec{H} : Magnetic Field
 \vec{M} : Magnetization
 \vec{B} : Magnetic Flux Density
 \vec{D} : Displacement Electric Field
 \vec{P} : Polarization
 \vec{k} : Wave Propagation Vector
 \vec{S} : Poynting Vector
 κ : Chirality Parameter
 θ : Azimuth Rotation Angle
 η : Elliptical Angle
 ρ : Charge Density
 \vec{J} : Current Density
 ζ, ξ : Coupling Terms
 χ : Tellegen Parameter
 ϵ : Permittivity of Medium
 μ : Permeability of Medium
 ϵ_0 : Permittivity of Free Space
 μ_0 : Permeability of Free Space
 ϵ_r : Relative Permittivity
 μ_r : Relative Permeability
 T : Transmission Coefficient
 R : Reflection Coefficient
 w : Angular Frequency
 c : Speed of Light
 n : Refractive Index
 n_+ : Refractive Index for RCP
 n_- : Refractive Index for LCP
 Z : Impedance

S_{11} : Forward Reflection Coefficient

S_{21} : Forward Transmission Coefficient

S_{22} : Backward Reflection Coefficient

S_{12} : Backward Transmission Coefficient

$\hat{a}_x, \hat{a}_y, \hat{a}_z$: Unit vectors along x -, y -, and z -, axis

Γ : Fresnel Reflection Coefficient

Γ_1, Γ_2 : First Reflection Coefficients

t_1, t_2 : Propagation Factors



CHAPTER 1

INTRODUCTION

1.1 Background and Scope of Study

Material science advances day by day and increases its importance rapidly in today's technology age. Therefore, desired physical, chemical or technological design properties of materials can determine the expected life of the product or its functionality. For that reason, material characterization is becoming more and more important in today's scientific community. Therefore, determining the exact properties of material directly contributes to developments of science and technology. In this thesis, the electrical properties of electromagnetic materials will be discussed especially for the metamaterials (MMs). In addition, research discipline of MMs finds a place at the intersection of optics, nanoscience, and photonics. Due to their exotic properties, MMs have attracted attention of today's scientific community with a growing interest since 2000, at the dawn of the new century. Moreover, MMs are artificially designed materials that demonstrate properties of negative refraction and negative refractive index [1], which are not present in naturally occurring materials.

In addition, unlike conventional materials that are present in nature, MMs are electromagnetic materials that can be used via their engineering design to manipulate electromagnetic properties and wave-matter interaction. Furthermore, MMs are artificial electromagnetic materials which can be engineered in periodic or non-periodic forms. Their periodic or non-periodic sequences, their composition and geometry overall play an important role on their unique properties not attainable by conventional materials. However, most MMs gain their exotic properties from their structural sequences rather than their composition.

The pioneer concept of MM was invented by the Russian physicist Victor Georgievich Veselago in 1967 [2] (which is translated into English in 1968). He theoretically demonstrated that electromagnetic properties of materials with

electrical permittivity (ϵ) and magnetic permeability (μ) can simultaneously be negative at the same frequency [2]. Then, nearly 30 years later after the Veselago's suggestion, in 1996 J.B. Pendry et al. (from Imperial College at UK) experimentally illustrated the negative ϵ by using artificial metallic wires [3]. Afterwards, in 1999 again J.B. Pendry et al. practically showed the negative μ by using split ring resonators (SRRs) without using any magnetic charge effect [4]. Until 2000, both electrical permittivity (ϵ) and magnetic permeability (μ) had been experimentally verified separately by the group of J.B. Pendry. However, in 2000 Smith et al. experimentally realized the double negative (DNG) material; that is, both ϵ and μ practically achieved by the construction of split rings and wires together [5].

As it has been mentioned above, based on the extraordinary properties of MM, it is not easy to find a suitable definition for the MM term to describe it. So what is metamaterial?

In the first times of MM around the years 2000, it was defined as a composite medium involving a periodic array of interspaced conducting non-magnetic SRRs and continuous wires [5]. Afterwards, definitions have been gradually expanded and around 2005, it is defined as 'an arrangement of artificial elements designed to obtain extraordinary electromagnetic properties'. Then, the progress has continued on MM around 2010 leading to its definition as artificial medium composed elements at a smaller size than the wavelength of the external stimuli [6]. Later, in 2015 the concept of MM changed into as 'arrangement on desired electromagnetic properties for mankind's requirements which artificially possessed by man-made media' [7]. Today, MMs are now seen as a set of engineering materials and rapidly expands beyond electromagnetics for potential novel wave phenomena.

There are various measurement techniques developed for characterization of MM in the literature such as free space [8, 9], coaxial [9–11], waveguide [9, 12–15] and resonator methods [9] for the examination of materials. According to the criterion of desired frequency ranges, flexibility of measurement set-up and sample preparation, each measurement technique has different advantages. These methods can be classified into either as a resonant or non-resonant category. However, except resonator methods, remaining other three techniques are called as non-resonant methods which mostly used in broadband measurements, while resonator method is commonly preferred for narrow band measurements with precise results [9]. On the other hand, non-resonant methods provide convenience of flexibility in broadband measurements and applicabilities are more suitable than the resonant methods. Since MMs are engineering materials compatible with

broadband frequency ranges, non-resonant methods provide more advantageous.

In addition, microwave non-resonant methods are divided into two groups: calibration-dependent and calibration-independent methods. As the name suggests for calibration-dependent technique, calibration kits and some kind of calibration standards are necessary before carrying measurements. There are several well-known calibration standards in literature such as, thru-reflect-line (TRL) [16], short-open-load-thru (SOLT), thru-reflect-match (TRM) and full two port [9]. Besides calibration-dependent methods, calibration independent methods were proposed by the researchers in recent years to eliminate the calibration kits and reduce the overall measurement time [10, 11, 17–23].

The scope of the study is the characterization of electromagnetic properties of MMs especially the chiral MMs over microwave region. Toward this end, we will first design a new structure called crescent shaped which demonstrate unique optical activity and circular dichroism. In that manner, we preferred to study on chiral MMs with proposing a new design of crescent shaped chiral MM configuration. As a second, near-field effect of chiral MMs are investigated by using S-parameters. Thirdly, coupling effects of nearby isotropic MM slabs are analyzed to retrieve accurate properties of MMs.

1.2 Literature Review and Motivation of Thesis

When Dr. Veselago opened the concept of artificial materials in 1967 [2], and he put forward an idea of materials that can have both a negative relative electrical permittivity (ϵ) and magnetic permeability (μ) simultaneously over a specific frequency range. These materials are then called as double negative (DNG) metamaterials (MMs) or left-handed materials (LHM) in literature. In LHM the wave vector \vec{k} is in the direction of cross product of magnetic (\vec{H}) and electric (\vec{E}) fields that is $(\vec{k} \times \vec{H} \times \vec{E})$ in which \vec{k} is in the direction of $\vec{H} \times \vec{E}$. As a result, both the time-averaged Poynting vector $\vec{S} = (1/2) \Re(\vec{E} \times \vec{H}^*)$ and the wave vector \vec{k} are in opposite directions leading to $\vec{k} \cdot \vec{S} < 0$.

Based on the theory of plasma, thin metallic wire arrays were proposed to demonstrate the ϵ negative media in 1996 [3]. In addition, by the same group (Pendry et al.), they practically illustrated the μ negative media by utilizing SRRs printed on circuit boards composed of conventional metallic inclusions in 1999 [4]. Then the outcomes of these studies led to numerous potential applications in many diverse areas, some of which show significant breakthrough applications

such as negative index materials [1], electromagnetic cloaks [24], sensors [25], perfect lens [26], absorbers [27], tunable devices [28–30], enhancement on antenna directivity [31], solar cells [32, 33] and etc.

For such applications, depending on the specification of electromagnetic properties, there are several geometrical designs for MMs in literature which can be fabricated in various different forms such as : π -shaped [34], U-shaped [35], cross shaped [36], Ω -shaped [39], S-shaped [40], crescent-shaped [41], V-shaped [42], and etc.

The response behaviour of MMs can be arranged or manipulated by depending on some conditions of charges on the metallic structures. For example, initially, accumulation of opposite charges at the corners and edge of a MM which induced by electrically dipole. As a second, electric fields impinging on the SRRS which generate surface current circulation as a result of magnetic dipoles. Thirdly, due to interaction of between electric and magnetic fields, this coupling or mutual effect can alter the behaviour of materials from isotropic to asymmetric transmission chiral case [35, 36, 41] or asymmetric reflection bi-anisotropic feature [34, 43–46].

For that reason, anisotropic, bi-anisotropic, and chiral MMs were engineered to obtain different electromagnetic properties. From this point of view, our concern in this thesis is about a chiral MM which has lack of mirror symmetry lead to extraordinary properties like circular dichroism, giant optical activity, different transmission scattering (S-) parameters, different responses for right circularly polarized waves (RCP) and left circularly polarized waves (LCP), different negative refractive index for RCP and LCP, as contrary to other MM types. In this manner, the electromagnetic response of chiral MMs must be retrieved correctly in order to investigate these uncommon properties.

Any object lacking of geometric symmetry between its mirror image can be called as a chirality medium. Therefore, the mirror of a chiral object cannot be obtained by any operation like rotation or translations [47]. In other words, if a chiral object is right handed, then its mirror image will be left handed. The interaction of electromagnetic waves in chiral medium leads to the rotation of the plane of the polarization. Therefore, a linearly polarized wave impinges on a chiral slab splits into two (left and right) circularly polarized waves with different phase velocities and this is defined as an optical activity. Therefore, by using polarization transformers, incident polarization can be transformed into any other polarizations with a certain angles [48].

In addition, the level of chirality determines the amount of rotation and attenuation of the wave through the medium [47]. For that reason, chiral media have tremendous applications in microwave engineering requiring optical activity and chirality. Initially, in 1811 Arago [49] discovered the rotation of the plane of a linearly polarized light for chiral molecule structures. On the other hand, in 1920 Lindman [50] used wire spirals and microwaves instead of chiral molecules and light signals to demonstrate optical activity. Later, this model was verified and applied by many scientists in the literature [51]. The fundamental phenomena of the chiral MMs are emerging from that model and depending on this wire spirals proposed by Lindman.

After surveying the literature extensively we noted that various studies were performed to examine electromagnetic properties of chiral MMs [35, 36, 52–56]. These methods are effective and well-established; however, they do not pay attention to near-field effects that might be present around the MMs boundaries. Recently, near-field effects on electromagnetic properties of isotropic and bi-anisotropic MMs were investigated through the studies [43, 44, 57–59]. To our best knowledge, near-field effects have not been investigated for retrieval of chiral MMs in literature. For that reason, in the first part of this thesis, we propose a new retrieval method for determining transmission and reflection coefficients of chiral MMs accurately by considering the near-field effects. On the other hand, in the second part of this thesis, we propose a new crescent shaped chiral designs that developed and implemented during this thesis. Results are compared with other suggested unit cell configurations in the literature such as u-shaped [35] and cross shaped [36]. In addition, as a third part, throughout this dissertation coupling phenomena between the adjacent MM unit cells are investigated. Since, nearby MM cells can affect each other and this coupling interactions leading to a change in the overall response of MMs indirectly.

The remaining part of this thesis is as follows:

In Chapter 2, retrieval of electromagnetic properties of MMs are investigated, especially the chiral MM. The most important contribution of such investigation is the derivation of all electromagnetic parameters forward and backward refractive index “ n_{\mp} ”, relative electrical permittivity constant “ ϵ_r ”, relative magnetic permeability “ μ_r ”, impedance “ z ”, reflection coefficient “ Γ ” and transmission coefficient “ T ”, chirality constant “ κ ”, and etc. Moreover, new crescent shaped chiral MM designs are investigated.

The aim of Chapter 3 is about retrieval algorithm of semi-infinite reflection

and transmission coefficients of chiral MMs involving near-field effects. This chapter also explicitly explains the S-parameters easily for the concept of MM structures. Moreover, through the this Chapter the investigation of near-field effects on chiral MMs are analyzed in detail.

In the Chapter fourth, a new type of crescent-shaped chiral MM structure has been proposed and its optical activity and chirality properties are examined with comparing the parameters of the U-shaped [37] and cross-shaped [38] MMs known in the literature.

The main goal of Chapter 5 is to study the coupling behaviour of nearby MM cells. The major contribution of this Chapter is to provide understanding of coupling phenomena by using S- parameters and application of signal graph technique (SGF). Additionally, the concept of electromagnetic propagation through the resonating structures are demonstrated. Toward this end, by handling each individual MM cell and whole cascaded structures, the evidence of coupling effects are described through overall response.

In the Chapter sixth, we briefly summarized the studies have been done during this thesis and mentioned about the some contributions to the scientific literature. In addition, by using proposed methods we give information about the further studies that can be done for potential issues in the future.

CHAPTER 2

METAMATERIALS

In this chapter, we will discuss characterization and realization of chiral metamaterials (MMs). Toward this end, we will first present the general literature review about material classification and then restrict this general review to the special material type of chiral MMs. Next, we will briefly explain the types of MMs and their compositions to get more information about the realization of MMs.

In addition, in the forward sections beginning from Maxwell's Equations we retrieved all equations necessary for characterization of chiral MM and its properties in detail. Furthermore, classification of bi-isotropic media such as Tellegen medium, Pasteur medium, Simple Isotropic medium and bi-isotropic medium are described in conjunction with reciprocity and chirality properties.

Moreover, retrieval parameters of chiral MM such as chirality parameters (κ), refractive index (n) for RCP and LCP, wave vector (k), azimuth rotation angle (θ), circular dichroism (η), transmission (T), reflection (R), impedance (Z), permittivity (ϵ) and (μ) are defined exactly in detail.

2.1 Classification of Metamaterials

In this part, we mention preconditions of MMs to achieve the exotic properties of such structures in detail. Before investigating specific MM types and designs, it is suitable to begin with the classification of materials from general perspective as shown in the diagram of Fig. 2.1. Classifying materials into four quadrant on a diagram with respect to permittivity and permeability can be a useful tool to gain more insight on MMs.

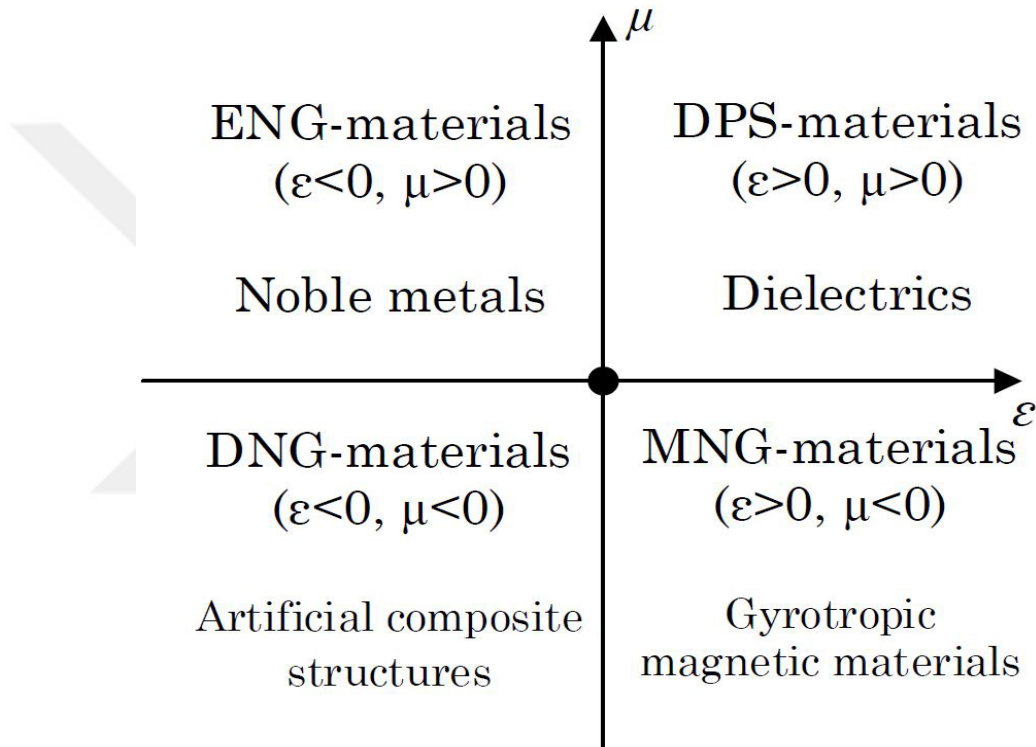


Figure 2.1 Diagram of classification of materials depending on the permeability and permittivity values [60].

The first quadrant is for conventional isotropic materials (double positive materials) where ϵ and μ are simultaneously greater than zero. The second quadrant is allocated for epsilon-negative materials (ENG-materials) where $\epsilon < 0$ and $\mu > 0$. The third quadrant is composed of materials having $\epsilon < 0$ and $\mu < 0$ where our main focus point is artificial structures which can not be found in nature but can be produced by engineering processes. Finally, the last quadrant is about μ negative materials which have $\epsilon > 0$ and $\mu < 0$ observed in some magnetic materials.

2.1.1 Double Positive Materials (DPS)

Generally, nearly all conventional materials existing in nature have positive permittivity and permeability values greater than unity ($\epsilon > 0$ and $\mu > 0$). For that reason, they are defined as double positive (DPS) materials with refraction property is illustrated as in the Fig. 2.2.

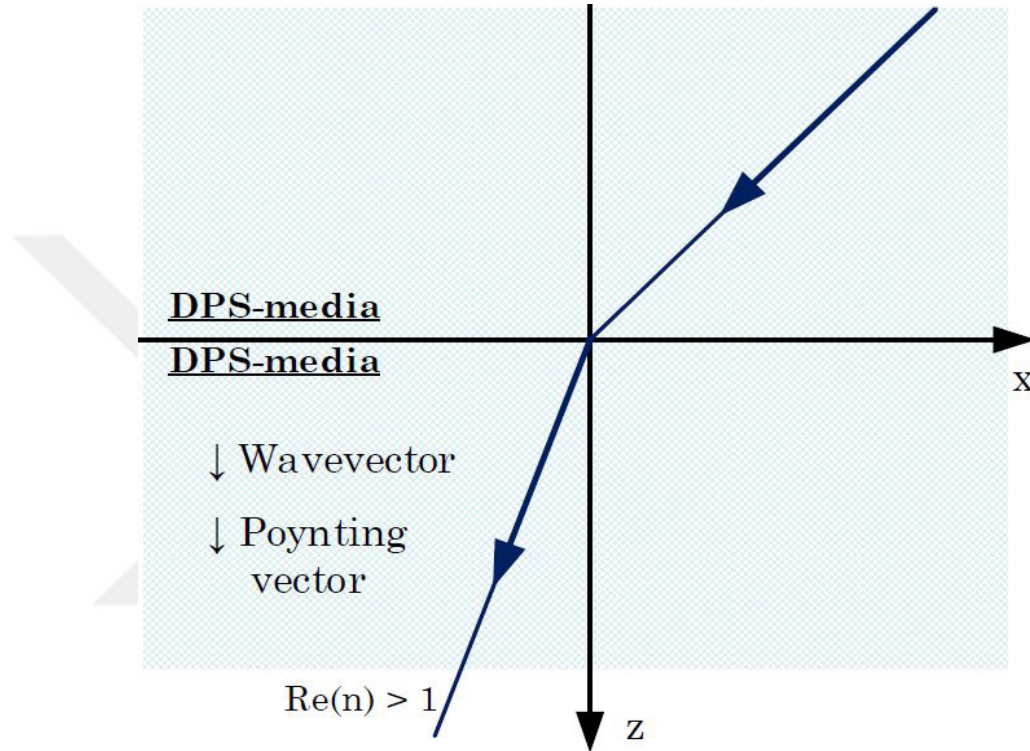


Figure 2.2 Configuration of conventional refraction when the both medium is DPS media [60].

In DPS medium the wavevector and Poynting vector are in the same direction and also the real part of the refractive index is greater than unity. Refraction takes place at the boundary of first quadrant to third quadrant as shown in the Fig. 2.2. DPS materials also described as right handed materials (RHM) because the direction of propagation of wave follows the right-hand rule.

2.1.2 Single Negative (SNG) Media only $\epsilon < 0$ or $\mu < 0$

There are also materials, called as single-negative (SNG) materials, demonstrating negative ϵ or μ values. They can be classified into two parts according to which constitutive parameters is negative as Epsilon-Negative (ENG) and Mu-Negative (MNG) materials. In these materials, due to having one of the constant value as negative then the imaginary part of the refractive index will be negative as a consequence of ENG or MNG property so that only evanescent electromagnetic waves can propagate through the material [60]. For example, when we describe dielectric constant vs. frequency in Drude model and below the plasma frequency, the metal has negative ϵ as shown in Fig. 2.3.

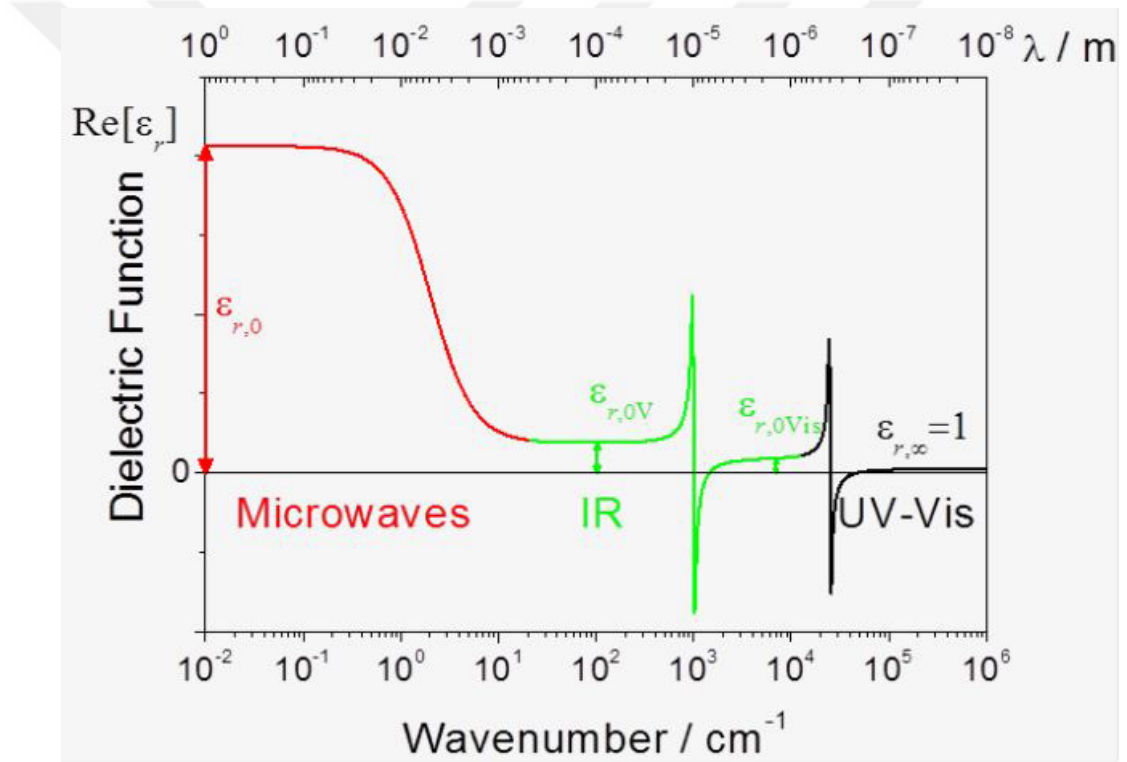


Figure 2.3 At optical and infrared frequency ranges the noble metals behave as ENG-materials for certain frequency regions [61].

In addition, at optical and infrared frequency ranges the noble metals behave as ENG-materials and plasma known as famous ENG-material for certain frequency regions. Furthermore, the property of $\mu < 0$ and $\epsilon > 0$ for MNG materials can be seen at gyrotropic materials especially in certain frequency regions.

2.1.3 ENG - Metamaterials $\epsilon < 0$

The firstly proposed and mostly known ENG-MM is realized by thin metallic wires by J. B. Pendry in 1998 [63]. The structure consists of periodically aligned parallel thin metal wires over which electric field lines are parallel as shown in Fig. 2.4 [62] to obtain effective permittivity less than zero at some certain frequency band.

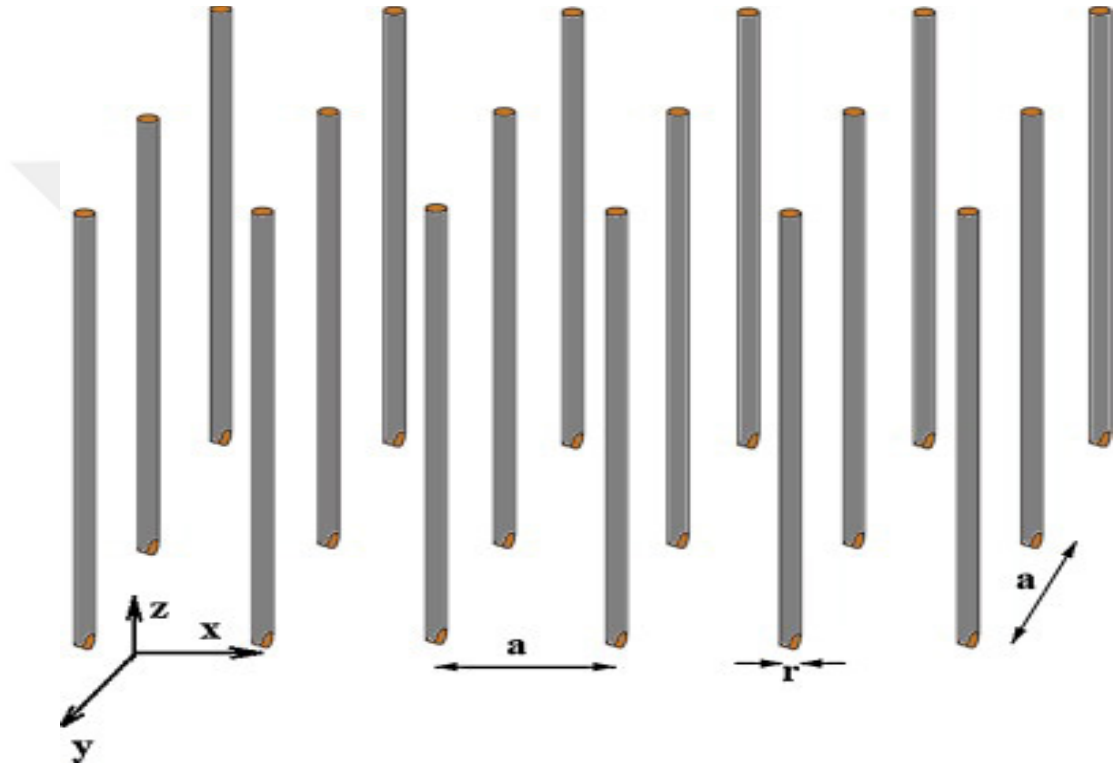


Figure 2.4 ENG-Structure consist of parallel long thin metal wires periodically aligned with radius r and a lattice period a [62].

The propagation in this kind of structure is similar to plasma and its frequency depends on radius and periodicity of consisting long wires. Below the plasma frequency of the structure effective permittivity of materials is negative. The extension of the parallel-wire geometry to three dimension is also possible in the literature [64].

2.1.4 MNG - Metamaterials $\mu < 0$

The split ring resonator (SRR) structure is the first MNG-MM widely studied in the literature [4]. SRRs can be composed of geometrically both in square or round rings shapes. In addition, SRRs are high conductive resonant structures and this resonance balances the inductance of the structure by occurred capacitance between the rings. Applying time-varying field on SRRs leads to circulating currents on the surface of the rings. Figs. 2.5 and 2.6 demonstrate the geometry and topology of one cell of round and square MNG-MMs, respectively.

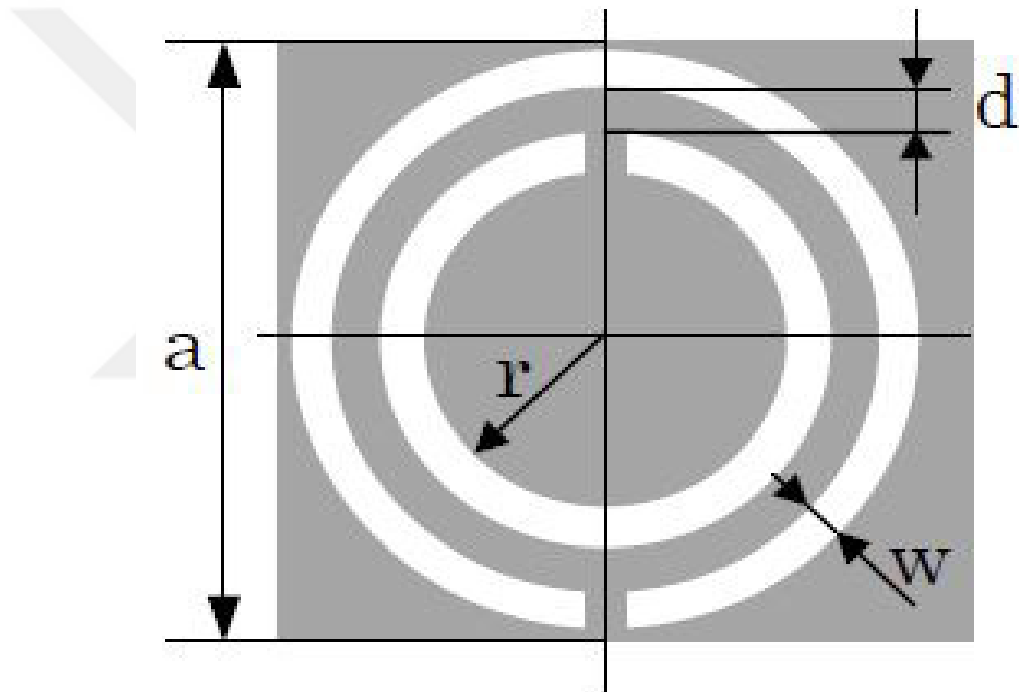


Figure 2.5 The first proposed unit cell of the SRR to achieve MNG-Structure in round shape [60].

To obtain effective permeability μ to be negative, the magnetic field of incident plane wave must be perpendicular to the SRR. On the other hand, if the magnetic field of incident plane wave is parallel to the SRR, then induced circulating currents are not effective in producing negative effective μ .

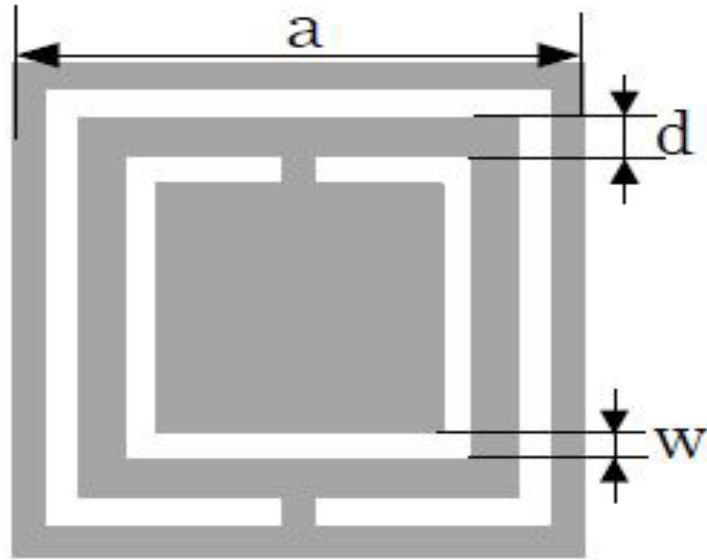


Figure 2.6 The first proposed unit cell of the SRR to achieve MNG-Structure in square shape [60].

There are many form of MMs alternative to SRRs were proposed in the literature to obtain MNG-structures some of which are in the form of spiral and S-shaped resonators illustrated in Fig. 2.7.

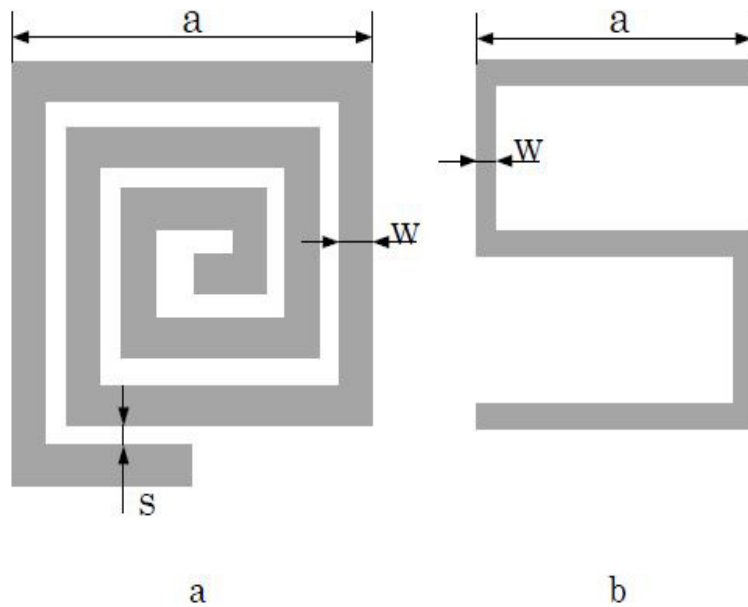


Figure 2.7 Unit cell of alternative MNG-structures (a) in spiral and (b) S-shaped resonator [60].

2.1.5 Double Negative (DNG) Media $\epsilon < 0$ and $\mu < 0$

Double-negative (DNG) materials (simultaneously $\epsilon < 0$ and $\mu < 0$) can not be found in nature, but they can be artificially produced. From the beginning of this century, the research and experiments toward realization of these materials have been very popular and scientists have extensively studied to find applications areas for them. DNG-materials were theoretically proposed in 1967 by the Russian scientist V. G. Veselago [2] and the simultaneously negative ϵ and μ are compatible and did not denied by the the Maxwell's equations. In these materials, due to having negative refractive index value, electromagnetic waves passing through the medium not only in the direction of as usual (as in the DPS-materials) but also in the symmetric of normal to the usual direction as illustrated in the Fig. 2.8.

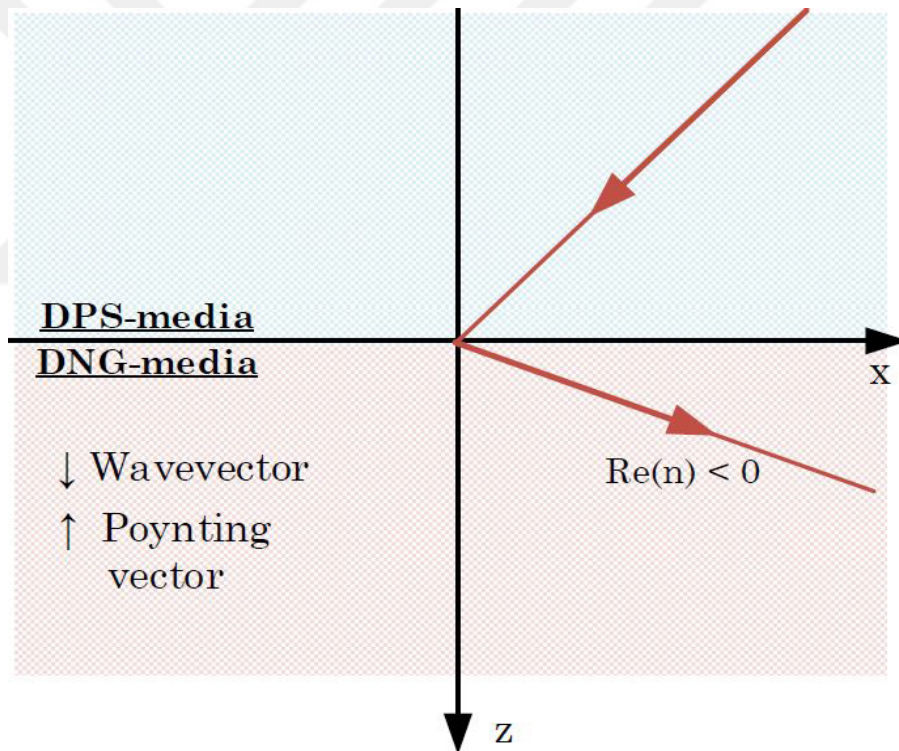


Figure 2.8 Configuration of refraction when the first medium is DPS media and the second medium is DNG media (both $\epsilon < 0$ and $\mu < 0$) [60].

Moreover, DNG-materials are sometimes described as Left-Handed materials (LHM) due to propagation of waves following the left thumb rule or negative index materials (NIM). For that reason, the wavevector and Poynting vector are propagating in the opposite directions.

2.2 Background on Classical Field Theory of Electromagnetism

In this section, the expressions underlying the basics of the properties necessary for chiral MMs will be reviewed. Toward this end, our analysis starts from basic Maxwell's equations which is known as the first consistent field theory. Unifying classical laws of electricity and magnetism, the Maxwell's equations describe the relation between electromagnetic sources (charges and currents) and the electric and magnetic fields in one general frame. In this thesis, main emphasize will be given on the interaction of electromagnetic wave with a chiral MM medium.

2.2.1 Vacuum Medium Case

The differential or point form of Maxwell's equations in free space can be written as:

$$\vec{\nabla} \cdot \vec{E} = 0, \quad (2.1)$$

$$\vec{\nabla} \times \vec{E} = -\mu_0 \frac{\partial \vec{H}}{\partial t}, \quad (2.2)$$

$$\vec{\nabla} \cdot \vec{B} = 0, \quad (2.3)$$

$$\vec{\nabla} \times \vec{B} = \epsilon_0 \mu_0 \frac{\partial \vec{E}}{\partial t}. \quad (2.4)$$

where \vec{E} and \vec{B} represent the electric and magnetic fields, $\epsilon_0 = c^2/\mu_0 \simeq 10^{-9}/36\pi$ (F/m) and $\mu_0 = 4\pi 10^{-7}$ (H/m) are the vacuum permittivity and permeability respectively, t denotes the time, and c is the speed of light in vacuum $c = 1/\sqrt{\epsilon_0 \mu_0} \simeq 2.99792458 \times 10^8$ (m/s).

2.2.2 Presence of Matter Case

Under the investigation of presence of the matter, the Maxwell's equations must contain volume charge density (ρ) and current density (\vec{J}) reading as:

$$\vec{\nabla} \cdot \vec{D} = \rho, \quad (2.5)$$

$$\vec{\nabla} \times \vec{E} = -\frac{\partial \vec{B}}{\partial t}, \quad (2.6)$$

$$\vec{\nabla} \cdot \vec{B} = 0, \quad (2.7)$$

$$\vec{\nabla} \times \vec{H} = \vec{J} + \frac{\partial \vec{D}}{\partial t}. \quad (2.8)$$

where \vec{D} is the displacement electric field and \vec{H} is the magnetic field intensity, ρ and \vec{J} are the (volume) charge density and (volume) current density respectively.

\vec{D} and \vec{H} are described in terms of \vec{E} and \vec{B} by constitutive parameters for the isotropic and uniform materials as:

$$\vec{D} = \epsilon \vec{E} = \epsilon_0 \vec{E} + \vec{P}, \quad (2.9)$$

$$\vec{H} = \vec{B}/\mu = \vec{B}/\mu_0 - \vec{M}. \quad (2.10)$$

where, \vec{P} indicates the polarization and \vec{M} represents the magnetization. Under external field, response of the matter is determined directly by dielectric permittivity and permeability.

The relations between relative permittivity and the relative permeability are also associated with $\epsilon = \epsilon_0 \epsilon_r$ and $\mu = \mu_0 \mu_r$, where the subscript “ r ” demonstrates the quantities relative to air (vacuum).

Contrary to the homogeneous and isotropic material with constitutive relations approximatively characterized by their permittivity and permeability, in recent years, a great variety of novel and exotic bi-isotropic and inhomogeneous

materials have been developed for promising practical applications. To characterize these special materials, it has been understood that the electric and magnetic fields for these complex materials can not be described with standard constitutive parameters. Since, bi-isotropic materials such as bi-anisotropic or chiral materials are involving cross coupling between strengths of electric and magnetic fields. For example, rotation of polarity of light either in transmission or refraction can be observed as a special optical property of bi-isotropic materials and represented by:

$$\vec{D} = \epsilon\vec{E} + \xi\vec{H}, \quad (2.11)$$

$$\vec{B} = \mu\vec{H} + \zeta\vec{E}. \quad (2.12)$$

Here, ζ and ξ are the intrinsic coupling terms whose values depend on the properties of the matter. Furthermore, ζ and ξ can be associated with Tellegen χ and chirality κ parameters

$$\chi - i\kappa = \frac{\xi}{\sqrt{\epsilon\mu}}, \quad (2.13)$$

$$\chi + i\kappa = \frac{\zeta}{\sqrt{\epsilon\mu}}. \quad (2.14)$$

Toward this end, among these particular materials we may consider reciprocal, chiral (Pasteur media) MM case in this thesis because asymmetric transmission propagation occurs in chiral medium.

After substitution of the above equations into the constitutive relations, the constitutive parameters for bi-isotropic chiral medium are described by following expressions:

$$\vec{D} = \epsilon\vec{E} + (\chi - i\kappa)\sqrt{\epsilon\mu}\vec{H}, \quad (2.15)$$

$$\vec{B} = \mu\vec{H} + (\chi + i\kappa)\sqrt{\epsilon\mu}\vec{E}. \quad (2.16)$$

A general bi-isotropic media can be classified depending on their χ and κ values shown in Table 2.1.

	Non-Chiral ($\kappa = 0$)	Chiral ($\kappa \neq 0$)
Reciprocal ($\chi = 0$)	Simple Isotropic Medium	Pasteur Medium
Non-Reciprocal ($\chi \neq 0$)	Tellegen Medium	General Bi-isotropic Medium

Table 2.1 Classification of Bi-isotropic Materials

From the Table 2.1, it is noted that bi-isotropic media and regular isotropic media differ from each other by additional terms of constitutive relations. χ is a dimensionless magneto-electric coupling constant and indicates the reciprocity of materials; that is, for non-reciprocal materials $\chi \neq 0$. In addition, κ is also another dimensionless chirality parameter demonstrating the chiral property of material. For the brevity it is demonstrated in Table 2.1.

Our aim in this thesis is to investigate the reciprocal-chiral medium (or Pasteur Medium) in microwave frequency regions. Toward this end, in the case of reciprocal chiral medium, the real part of χ will be equal to 0 and the equation of (2.15) - (2.16) will reduce to below relations as:

$$\begin{pmatrix} \vec{D} \\ \vec{B} \end{pmatrix} = \begin{pmatrix} \epsilon & -i\kappa/c \\ +i\kappa/c & \mu \end{pmatrix} \begin{pmatrix} \vec{E} \\ \vec{H} \end{pmatrix} \quad (2.17)$$

To validate above equation (2.17), we can substitute 0 in stead of κ , then the equation (2.17) will reduce to classical constitutive relations for the non-chiral traditional material case. On the other hand, we are interested in the interaction of plane wave propagation with chiral materials. For that reason, to obtain electric field in chiral materials, we utilize above constitutive equations with frequency domain source-free Maxwell's Equations.

2.3 Retrieval Method for Chiral Materials

2.3.1 Wave Propagation in Chiral Medium

Hereafter, our aim is to derive refractive index n and chirality constant κ for left-handed circularly polarized (LCP) and right-handed circularly polarized (RCP) waves for chiral materials. From source-free Maxwell's equations, we know that

$$\vec{k} \times \vec{E} = \omega \vec{B}, \quad \vec{k} \times \vec{H} = -\omega \vec{D}. \quad (2.18)$$

Substituting the constitutive relations in the equation of (2.17) into the equation (2.18) reduces to:

$$\vec{D} = \epsilon \vec{E} - \frac{i\kappa}{c} \vec{H}, \quad \vec{B} = \mu \vec{H} + \frac{i\kappa}{c} \vec{E}. \quad (2.19)$$

By using the equation (2.18) we can write,

$$\vec{k} \times (\vec{k} \times \vec{E}) = \vec{k} \times (\omega \vec{B}) = \omega (\vec{k} \times \vec{B}), \quad (2.20)$$

where \vec{k} is the wave vector and ω is the angular frequency of the plane wave impinging into a chiral material. From this step, we can combine the equation (2.19) and (2.20) into one expression and obtain,

$$\vec{k} \times \vec{H} = -\omega \vec{D} = -\omega \left(\epsilon \vec{E} + \frac{i\kappa}{c} \vec{H} \right) = \frac{1}{\mu} \left(\frac{\vec{k} \times (\vec{k} \times \vec{E})}{\omega} + \frac{i\kappa}{c} (\vec{k} \times \vec{E}) \right). \quad (2.21)$$

Applying some algebraic process over the equation (2.21) to remove the dependence of \vec{B} and \vec{H} parameters, reduces it an expression involving \vec{E} field only as

$$\left[\frac{\vec{k} \times (\vec{k} \times \vec{E})}{\omega} + \frac{i\kappa}{c} (\vec{k} \times \vec{E}) \right] = \left[-\omega \mu \epsilon \vec{E} + \omega \frac{\kappa^2}{c^2} \vec{E} - \frac{i\kappa}{c} (\vec{k} \times \vec{E}) \right]. \quad (2.22)$$

From the equation (2.22), we can obtain the equation varying refractive index constant,

$$\vec{k} \times (\vec{k} \times \vec{E}) = -k_0^2(n^2 - \kappa^2)\vec{E} - 2i\kappa k_0(\vec{k} \times \vec{E}). \quad (2.23)$$

Assuming that the plane wave is propagating through a chiral medium and $\vec{E} = (\hat{a}_x E_{0x} + \hat{a}_y E_{0y} + \hat{a}_z E_{0z})$, equation (2.23) can be organized to determine κ as

$$\begin{aligned} \frac{1}{2i\kappa k_0 k} [k_0^2(\kappa^2 - n^2) + k^2] (\hat{a}_x E_{0x} + \hat{a}_y E_{0y} + \hat{a}_z E_{0z}) \\ = \hat{a}_z \times (\hat{a}_x E_{0x} + \hat{a}_y E_{0y} + \hat{a}_z E_{0z}), \end{aligned} \quad (2.24)$$

where $n = \sqrt{\mu_r \epsilon_r}$. After performing some algebraic operations the equation of (2.24) can be written as

$$\frac{E_{0y}}{E_{0x}} = \frac{1}{2i\kappa k_0 k} [k_0^2(n^2 - \kappa^2) - k^2]. \quad (2.25)$$

The equation (2.25) is a second order equation with two unknowns leading to the index of refraction for RCP and LCP defined as:

$$n^2 - 2n\kappa - (n^2 - \kappa^2) = 0, \quad n_{\mp} = n \mp \kappa. \quad (2.26)$$

By the same algorithm which we extracted n and κ , we can assume that wave is propagating in \hat{a}_z direction in a chiral medium, for simplicity the derivation of the wave vector k will not be given but it is illustrated shortly as:

$$k^2 \mp 2\kappa k_0 k - k_0^2(n^2 - \kappa^2) = 0, \quad k_{\mp} = k_0(n \mp \kappa). \quad (2.27)$$

From the equations (2.26) and (2.27), we can note that if we constitute high chirality κ values greater than the n value then n_- will be negative so that the negative index chiral materials can be realized by this approach. In addition to above equations, κ values can be calculated as:

$$\kappa = \frac{k_+ - k_-}{2k_0} \quad or \quad \kappa = \frac{n_+ - n_-}{2}. \quad (2.28)$$

The two important properties of chiral materials are optical activity and circular dichroism. When a linearly polarized plane wave passes through a chiral medium its polarization rotates resulting in a optical activity. This polarization azimuth rotation angle of a elliptically polarized light is mathematically defined as:

$$\theta = \frac{1}{2}[\arg(T_+) - \arg(T_-)]. \quad (2.29)$$

where T_+ and T_- indicate the transmission coefficients for RCP and LCP waves. The second important property of a chiral medium is the circular dichroism which arises from the different absorption and distortion of RCP and LCP waves while interaction with chiral particles. Circular dichroism is defined in terms of the difference of transmitted powers as:

$$\eta = \frac{1}{2} \tan^{-1} \left(\frac{|T_+|^2 - |T_-|^2}{|T_+|^2 + |T_-|^2} \right). \quad (2.30)$$

2.3.2 Retrieval Parameters for Chiral Medium

In the past, researchers investigated the effective media extensively being characterized by electromagnetic properties via experimental and numerical techniques. Toward this end, to retrieve exact electromagnetic parameters of a chiral MM, a slab of reciprocal (Pasteur) chiral material will be investigated

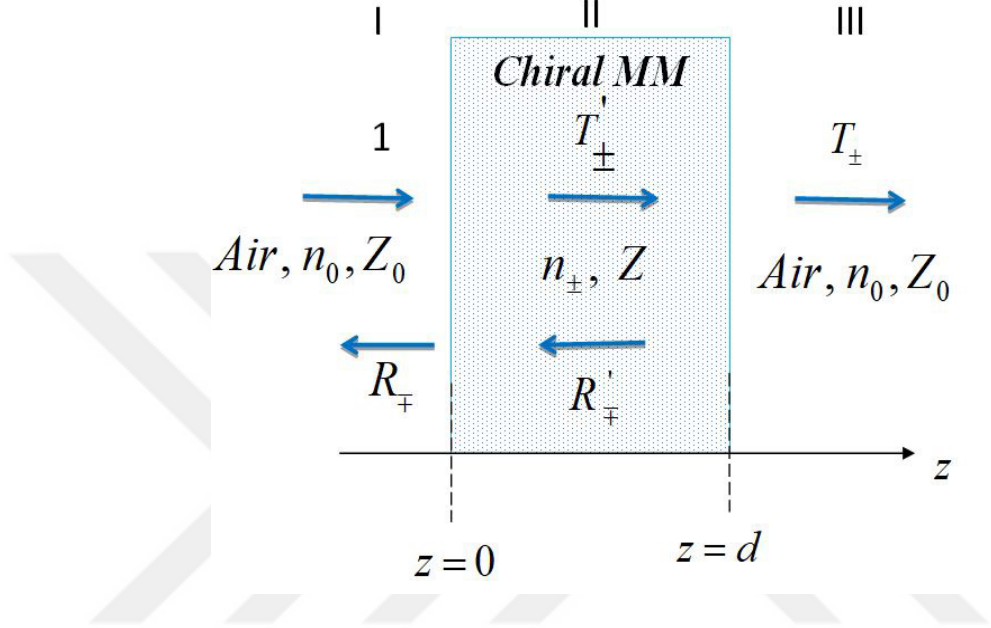


Figure 2.9 Schematics for the transmission and reflection properties of a chiral MM slab for a plane wave incidence.

To describe macroscopic behaviour of a chiral MM slab, we consider the problem in Fig. 2.9. The intrinsic properties ϵ , μ and n of a homogeneous medium is independent of its thickness. However, MMs structures are inhomogeneous structure whose thickness is limited by the unit cell size of the MM.

Retrieval procedure of chiral MMs is very similar to the retrieval procedure of regular MMs except that appropriate branch indices must be determined for each refractive index n_+ and n_- for RCP and LCP waves. Assume that a circularly polarized plane wave normally impinges on a homogeneous chiral MM slab in vacuum with a thickness of d and has refractive index of n_{\mp} and impedance of Z (note that Z 's are identical) for RCP and LCP waves as seen in Fig. 2.9.

The wave vector is in the \hat{z} direction so that all electric and magnetic fields are tangential to interfaces. Incident and reflected electric fields for a normally impinging circular polarized wave will be as:

$$\mathbf{E}_{\mp}(z) = (\hat{a}_x \mp i\hat{a}_y)E'_0 e^{-ikz}, \quad (\text{incident}) \quad (2.31)$$

$$\mathbf{E}_{\mp}(z) = (\hat{a}_x \mp i\hat{a}_y)E'_0 e^{ikz}. \quad (\text{reflected}) \quad (2.32)$$

It is assumed that amplitude of incident wave is to be unity and reflection coefficient in medium (I) is R_{\mp} and transmission coefficients in (III) interface is T_{\mp} where \mp denotes forward and backward term. Moreover, inside the chiral slab the forward and backward waves are R'_{\mp} and T'_{\mp} for RCP and LCP waves. The impedance Z is defined as:

$$Z = \sqrt{\mu/\epsilon} \quad \text{and} \quad Z_0 = \sqrt{\mu_0/\epsilon_0}. \quad (2.33)$$

By applying the boundary condition of the continuity at the first interface $z = 0$, the tangential electric and magnetic fields have following equations:

$$1 + R_{\mp} = T'_{\mp} + R'_{\mp}, \quad (2.34)$$

$$1 - R_{\mp} = \frac{T'_{\mp} - R'_{\mp}}{Z}. \quad (2.35)$$

Similarly applying the boundary condition of the continuity at the second interface of $z = d$ yields

$$T'_{\mp} e^{ik_{\mp}d} + R'_{\mp} e^{-ik_{\mp}d} = T_{\mp}, \quad (2.36)$$

$$\frac{T'_{\mp} e^{ik_{\mp}d} - R'_{\mp} e^{-ik_{\mp}d}}{Z} = T_{\mp}. \quad (2.37)$$

where k_{\mp} is defined as the wave vector for forward and backward waves. Then, the relation for the wave vectors will be $k_+ + k_- = 2nk_0$. Toward this end, by eliminating T' and R' in equations (2.34) to (2.37), we can obtain the transmission and reflection coefficients as following [36]:

$$T_{\mp} = \frac{4Ze^{ik_{\mp}d}}{(1+Z)^2 - (1-Z)^2e^{2ink_0d}}, \quad (2.38)$$

$$R_{\mp} = \frac{(1-Z)^2(e^{2ink_0d} - 1)}{(1+Z)^2 - (1-Z)^2e^{2ink_0d}}. \quad (2.39)$$

As seen from the equation (2.39), R_+ and R_- are equal to each other due to identical impedances for RCP and LCP waves. By applying some algebraic manipulations on the equations (2.38) and (2.39), the impedance Z and refractive index n_{\mp} are given as:

$$Z = \mp \sqrt{\frac{(1+R)^2 - T_+T_-}{(1-R)^2 - T_+T_-}}, \quad (2.40)$$

$$n_{\mp} = \frac{i}{k_0d} \left[\ln \left(\frac{1}{T_{\mp}} \left(1 - \frac{Z-1}{Z+1} R \right) \mp 2im\pi \right) \right]. \quad (2.41)$$

where m is the branch index and proper m value can be found using the group delay technique [65]. The correct sign for square root in equation (2.40) and the correct branch index in logarithm of equation (2.41) should be selected carefully according to principle of energy conservation as below:

$$\Re(Z) \geq 0, \quad \Im(n) \geq 0. \quad (2.42)$$

When the parameters Z and n_{\mp} are retrieved from the equations (2.41) and (2.42), the remaining parameters can be calculated from the following equations:

$$\begin{aligned} \kappa &= (n_+ - n_-)/2, & \mu &= n \cdot Z, \\ n &= (n_+ + n_-)/2, & \epsilon &= n/Z. \end{aligned} \quad (2.43)$$

2.3.3 Alternative Retrieval Algorithm for Chiral Materials

Actually, in this section another alternative route will be demonstrated to obtain constitutive parameters. Here, we consider again the same slab as in the Fig. 2.9. Then, if we redefine $T = \sqrt{T_+ T_-}$ and $R = R_{\mp}$ according to equations (2.38) and (2.39), the transmission T and reflection R can be written as:

$$T = \frac{4Z e^{ink_0 d}}{(1+Z)^2 - (1-Z)^2 e^{2ink_0 d}}, \quad (2.44)$$

$$R = \frac{(1-Z)^2 (e^{2ink_0 d} - 1)}{(1+Z)^2 - (1-Z)^2 e^{2ink_0 d}}. \quad (2.45)$$

The equations (2.44) and (2.45) are exactly valid for ordinary nonchiral materials. For that reason, traditional retrieval algorithm can be applied to obtain the retrieval parameters of n , κ , ϵ and μ as determined from the equation (2.43) [66]. Then, by using equation (2.38), we can derive κ as:

$$\kappa = \frac{-i}{2k_0 d} \ln \left(\frac{T_+}{T_-} \right) = \frac{-i}{2k_0 d} \ln \left(\frac{|T_+| e^{i\phi_+}}{|T_-| e^{i\phi_-}} \right), \quad (2.46)$$

where ϕ_{\mp} denote the phases of transmission T_{\mp} .

After explicitly determining the κ values using the equation (2.46), the refractive index can be computed readily from the equation below:

$$n_{\mp} = n \mp \kappa. \quad (2.47)$$

In addition, with the equation (2.46) at hand, it is understood that the real and imaginary parts of κ are respectively related to optical activity (azimuth rotation) angle θ and circular dichroism η as retrieved from the equations of (2.29) and (2.30). They can be defined as below:

$$\Re(\kappa) = \frac{\phi_+ - \phi_- + 2m\pi}{2k_0 d}, \quad (2.48)$$

$$\Im(\kappa) = \frac{\ln|T_-| - \ln|T_+|}{2k_0 d}, \quad (2.49)$$

where m is any integer defined by the condition of $-\pi < \phi_+ - \phi_- + 2m\pi < \pi$.

To summarize what we have done until here is: starting from classical electromagnetic relations and Maxwell's Equations, we theoretically derived all parameters related to the chiral phenomena for a plane wave (Fig. 2.9). Retrieval parameters of chiral MMs such as chirality parameters (κ), refractive index (n) for RCP and LCP, wave vector (k), azimuth rotation angle (θ), circular dichroism (η), transmission (T), reflection (R), impedance (Z), permittivity (ϵ) and (μ) are revisited over which our new algorithmic extraction including near-field effects can be constructed.

As mentioned in Chapter 1, the forward and backward transmission of chiral materials are different while reflections are the same verified by the previous equations contrary to bi-anisotropic materials which have non-identical forward and backward reflection S-parameters. To realize negative refractive index in chiral materials the value of κ should be $\kappa > n$ to satisfy the equation (2.47). In addition, for desiring more optical activity and less circular dichroism in chiral MMs azimuth rotation angle (θ) and ellipticity angle of circular dichroism (η) should be arranged appropriately. As mentioned previously, the impedance of chiral material does not differ for RCP and LCP waves however, refractive indices are changing so they are described as n_+ and n_- .

CHAPTER 3

ANALYSIS OF NEAR-FIELD EFFECTS FOR CHIRAL METAMATERIALS SLABS

3.1 Introduction

Metamaterials (MMs) attain their special properties not just from their composition and geometrical shape but also their periodic structural sequences. This additional flexibility allow one to design MMs in various forms having anisotropic, bi-anisotropic, and chiral properties [57, 44, 43, 59, 36, 35] demonstrating exotic electromagnetic properties not attainable by natural materials. Among other MM types, our concern in this thesis is chiral MMs with lack of mirror symmetry showing extraordinary properties like circular dichroism and optical activity.

In the previous chapter, we have examined a retrieval procedure for chiral MMs well-known in the literature [36] and derived expressions for chirality and optical activity. Although explicit in form, this retrieval procedure has the disadvantage that it does not take into account the near field effects. In this chapter, a new retrieval procedure will be proposed considering the near field effects especially important for MMs at their resonances.

A retrieval method for determining electromagnetic properties of chiral MMs has been proposed by Dr. Zhao and his colleagues [36]. Even though this proposed technique is effective and well-established, the near-field effects which might be present around the MMs borders have not been considered.

Near-field effects for determining the electromagnetic properties of isotropic and bi-anisotropic MMs were examined through the studies [57, 44, 43, 59] in recent years. However, to our best knowledge, a retrieval method for chiral MMs by taking into account near-field effects has not been incorporated until now. Therefore, in this thesis, a new retrieval method for determining the semi-infinite reflection coefficients of chiral MMs considering the near-field effects is proposed via using scattering (S-) parameters.

Toward this end, we propose a method for accurate electromagnetic characterization of chiral MM slabs by taking into account the near field effects which is caused by high order modes at borders of materials for determining the exact reflection coefficients.

Simulations were performed in the microwave frequency range, specifically from 3.5 GHz to 7.5 GHz. To compile simulations, frequency domain solver and free space conditions were chosen. Unit cell boundary conditions were selected in the electric and magnetic field directions. Time dependence in this chapter was assumed to be in time harmonic form $e^{j\omega t}$ and propagation direction was selected in the \hat{z} direction. To validate the derived expressions taking into account the near field effects, a chiral MM with U-shaped structure [37] was considered.

3.2 Theoretical Analysis of Chiral MMs with Near-Field Effects

The problem statement is investigation of near field effects of a chiral MM slab placed in free space medium is considered. In order to investigate the electromagnetic response of chiral MMs correctly, the retrieval procedure should be extracted correctly. By considering the near-field effects for correct retrieval of electromagnetic properties of chiral MMs, a configuration of Fig. 3.1 is examined to determine the correct S-parameters and other necessary parameters.

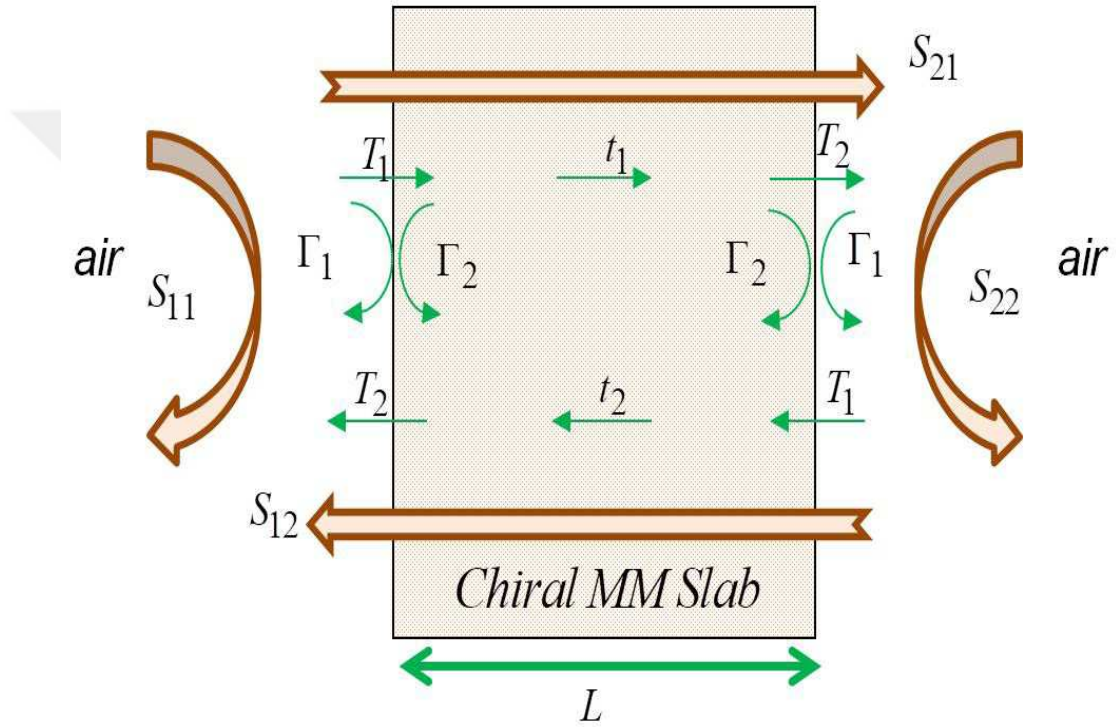


Figure 3.1 Investigated chiral MM slab for near-field effect analysis involving semi-infinite transmission and reflection and S-parameters.

While forward and backward semi-infinite reflection coefficients are different in bi-anisotropic MMs [43], in chiral MMs forward and backward propagation factors (t_1 and t_2) are expected to be different as shown in Fig. 3.1 due to properties of circular dichroism and optical activity.

Following the studies [57, 43], the ray-tracing method is useful for us to determine the relation between scattering parameters and reflection and transmission coefficients.

Application of the ray-tracing method for determining the forward and backward S-parameters for chiral MMs is as follows:

The S-parameters for forward transmission is:

$$\begin{aligned}
 S_{21} &= T_1 T_2 t_1 + T_1 T_2 t_1^2 t_2 \Gamma_2^2 + T_1 T_2 t_1^3 t_2^2 \Gamma_2^4 + T_1 T_2 t_1^4 t_2^3 \Gamma_2^6 + \dots \\
 S_{21} &= T_1 T_2 t_1 (1 + (t_1 t_2 \Gamma_2^2) + (t_1 t_2 \Gamma_2^2)^2 + \dots) = \frac{T_1 T_2 t_1}{1 - t_1 t_2 \Gamma_2^2}.
 \end{aligned} \tag{3.1}$$

The S-parameters for backward transmission is:

$$\begin{aligned}
 S_{12} &= T_1 T_2 t_2 + T_1 T_2 t_2^2 t_1 \Gamma_2^2 + T_1 T_2 t_2^3 t_1^2 \Gamma_2^4 + T_1 T_2 t_2^4 t_1^3 \Gamma_2^6 + \dots \\
 S_{12} &= T_1 T_2 t_2 (1 + (t_2 t_1 \Gamma_2^2) + (t_2 t_1 \Gamma_2^2)^2 + \dots) = \frac{T_1 T_2 t_2}{1 - t_2 t_1 \Gamma_2^2}.
 \end{aligned} \tag{3.2}$$

The S-parameters for forward reflection is:

$$\begin{aligned}
 S_{11} &= \Gamma_1 + T_1 T_2 t_2 t_1 \Gamma_2 + T_1 T_2 t_2^2 t_1^2 \Gamma_2^3 + T_1 T_2 t_2^4 t_1^4 \Gamma_2^5 + \dots \\
 S_{11} &= \Gamma_1 + T_1 T_2 t_2 t_1 \Gamma_2 (1 + t_1 t_2 \Gamma_2^2 + \dots) = \Gamma_1 + \frac{T_1 T_2 t_1 t_2 \Gamma_2}{1 - t_2 t_1 \Gamma_2^2}.
 \end{aligned} \tag{3.3}$$

The S-parameters for backward reflection is:

$$\begin{aligned}
 S_{22} &= \Gamma_1 + T_2 T_1 t_1 t_2 \Gamma_2 + T_2 T_1 t_1^2 t_2^2 \Gamma_2^3 + T_2 T_1 t_1^4 t_2^4 \Gamma_2^5 + \dots \\
 S_{22} &= \Gamma_1 + T_2 T_1 t_1 t_2 \Gamma_2 (1 + t_2 t_1 \Gamma_2^2 + \dots) = \Gamma_1 + \frac{T_2 T_1 t_2 t_1 \Gamma_2}{1 - t_1 t_2 \Gamma_2^2}.
 \end{aligned} \tag{3.4}$$

In equations (3.1)-(3.4), Γ_1 and Γ_2 are the semi-infinite reflection coefficients from air to MM slab and from MM slab to air, respectively, T_1 and T_2 are the boundary transmission coefficients, and t_1 and t_2 represent the propagation factors given as

$$t_1 = e^{-jk_0 n_+ L}, \quad t_2 = e^{-jk_0 n_- L}, \quad n_{\mp} = n \mp \kappa, \quad (3.5)$$

where n_+ and n_- illustrate the effective refractive indices for right hand circular polarization (RCP) and left hand circular polarization (LCP), L is the thickness of the chiral MM, and κ is the dimensionless chirality parameter.

As it is seen from equations (3.1)-(3.4) that S_{11} and S_{22} are the same whereas S_{21} and S_{12} are different due to different propagation factors of t_1 and t_2 as a consequence of chirality coefficient κ . When $\kappa = 0$, the expressions of S_{21} and S_{12} become identical and reduce to those in (13) and (14) in [57], verifying the forward problem.

In this study, our purpose is to extract Γ_1 and Γ_2 from equations (3.1)-(3.4). Toward this end, as was done in [43, 57], we consider two identical chiral MM slabs with different lengths L_1 and L_2 and derive Γ_1 as

$$\Gamma_1^2 (S_{11}^{L_1} - S_{11}^{L_2}) + \Gamma_1 X_1 + Y_1 = 0, \quad (3.6)$$

$$X_1 = (S_{11}^{L_2})^2 - (S_{11}^{L_1})^2 + S_{12}^{L_1} S_{21}^{L_1} - S_{12}^{L_2} S_{21}^{L_2}, \quad (3.7)$$

$$Y_1 = S_{11}^{L_2} [(S_{11}^{L_1})^2 - S_{12}^{L_1} S_{21}^{L_1}] - S_{11}^{L_1} [(S_{11}^{L_2})^2 - S_{12}^{L_2} S_{21}^{L_2}], \quad (3.8)$$

$$\Gamma_1 = \frac{-X_1 \mp \sqrt{X_1^2 - 4Y_1(S_{11}^{L_1} - S_{11}^{L_2})}}{2(S_{11}^{L_1} - S_{11}^{L_2})}. \quad (3.9)$$

Considering $\kappa = 0$ reduces the expressions in equations (3.5)-(3.8) to those equations (16) and (17) in [57], verifying the expression of Γ_1 . Once Γ_1 found for the chiral MM, Γ_2 can be determined as

$$\Gamma_2 = \frac{S_{11}^{L_1} - \Gamma_1}{t_1^{L_1} S_{12}^{L_1}} = \frac{S_{11}^{L_2} - \Gamma_1}{t_2^{L_2} S_{21}^{L_2}}, \quad (3.10)$$

where

$$t_1^{L_1(2)} = e^{-jk_0 u_1 [\ln(u_2 u_3) + j2\pi m] L_1(2)}, \quad (3.11)$$

$$t_2^{L_1(2)} = e^{-jk_0 u_1 [\ln(u_2 u_4) + j2\pi m] L_1(2)},$$

$$u_1 = \frac{j}{k_0(L_1 - L_2)}, \quad u_2 = \frac{S_{11}^{L_1} - \Gamma_1}{S_{11}^{L_1(2)} - \Gamma_1}, \quad (3.12)$$

$$u_3 = \frac{S_{12}^{L_2}}{S_{12}^{L_1}}, \quad u_4 = \frac{S_{21}^{L_2}}{S_{21}^{L_1}}.$$

The parameter m is the branch index (integer) value in equation (3.11) that can be determined using [65].

3.3 Validation and Simulation

In order to validate the proposed retrieval method, two different analyses were considered. In the first case, two identical isotropic and homogeneous Teflon samples are considered as shown in Fig. 3.2. The properties of Teflon sample are: complex permittivity is $\epsilon_{rT} = 2.01 - i0.001$ with lengths $L_1 = 1.00$ mm and $L_2 = 2.00$ mm. For the computational volume dimensions, the height and width of the Teflon sample were selected as $a_x = 11.25$ mm and $a_y = 11.25$ mm.

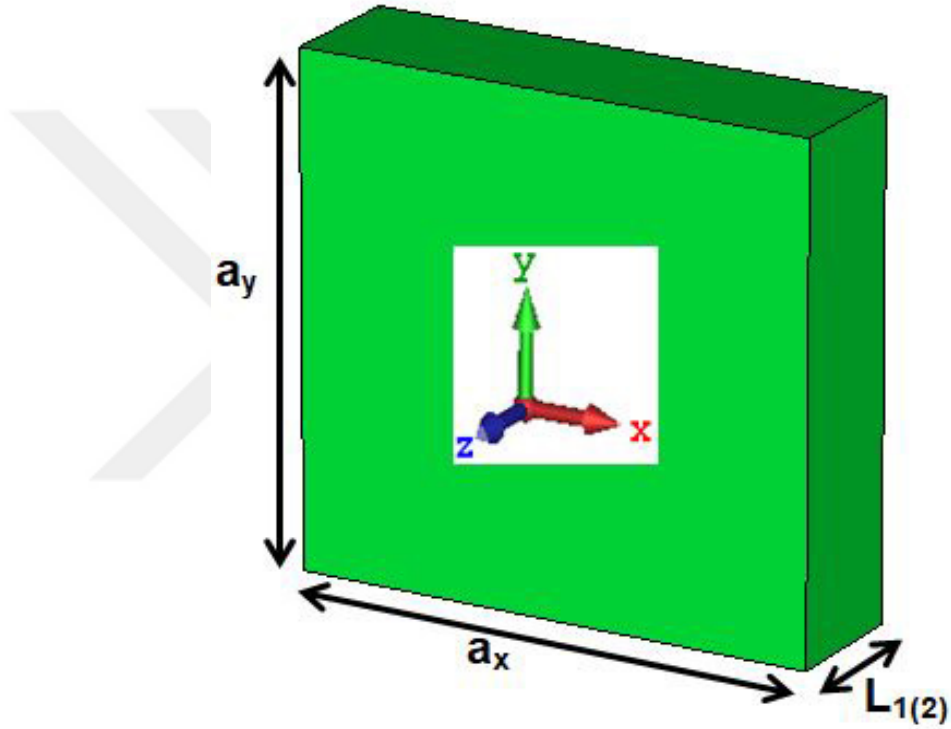


Figure 3.2 Simulated geometrical properties of investigated configuration for the Teflon sample in CST.

In the second case, an U-shaped MM structure was considered as demonstrated in Fig. 3.3. The volume dimensions of the MM cell are $a_x = 15$ mm, $a_y = 15$ mm, and $a_z = 10$ mm. The dielectric constant of substrate is $\epsilon_r = 4$ and has a thickness of $d = 1.6$ mm with loss tangent of 0.025. The geometrical length of outer ring is $m = 6$ mm, linewidth of each ring is $w = 0.7$ mm, the separation between the rings is $s = 1.5$ mm, and the copper used for SRRs has a thickness of 0.03 mm. Nearly all dimensions of the MM cell are taken from according to study of in [35].

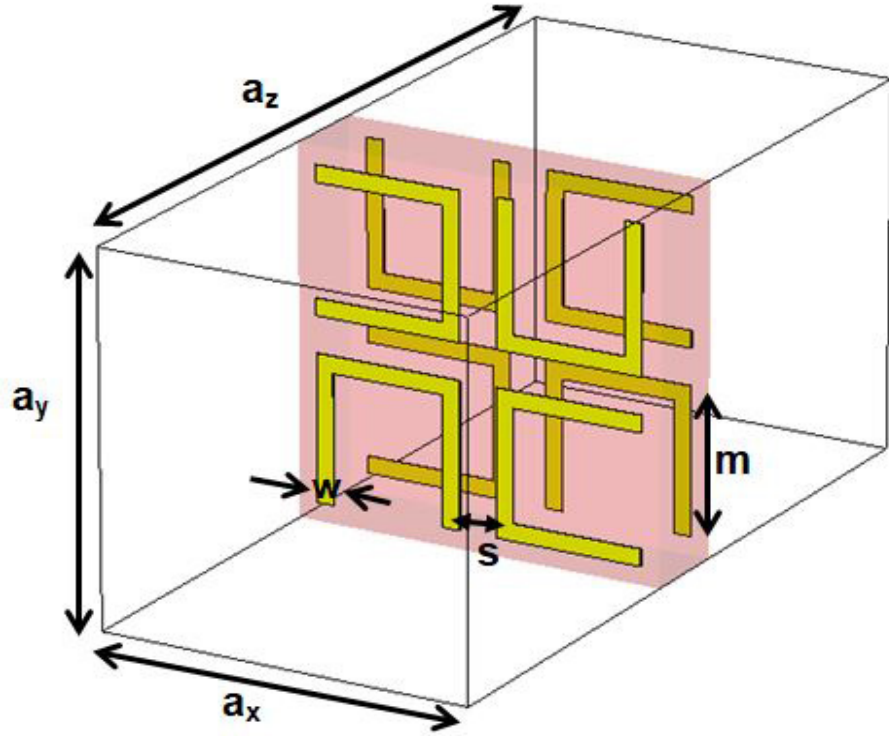


Figure 3.3 Simulated geometrical properties of analyzed configuration for the chiral MM cell with U-shaped split-ring-resonators.

S-parameters of both Teflon sample and MM slab were simulated by the 3-D electromagnetic simulator program-CST Microwave Studio. In simulations, frequency domain solver and “unit cell” boundary conditions over $x - y$ plane were taken by assuming that the wave is propagating in the \hat{z} direction.

3.4 Discussion on Results of Near-Field Effects

The magnitudes of simulated S-parameters of the Teflon sample with length $L_1 = 1.00$ mm and $L_2 = 2.00$ mm and the analyzed MM slab with length $L_1 = 50$ mm (5 cells) and $L_2 = 60$ mm (6 cells) are demonstrated in Figs. 3.4 - 3.7. Although the Teflon sample is reflection symmetric ($S_{11} = S_{22}$) and transmission-symmetric ($S_{21} = S_{12}$), the analyzed MM slab demonstrates reflection-symmetric and transmission-asymmetric property ($S_{21} \neq S_{12}$) which can be noted from from Figs. 3.4 - 3.7. This property can be associated with cross coupling effect between the electric and magnetic fields (chirality phenomena) inside the MM slab.

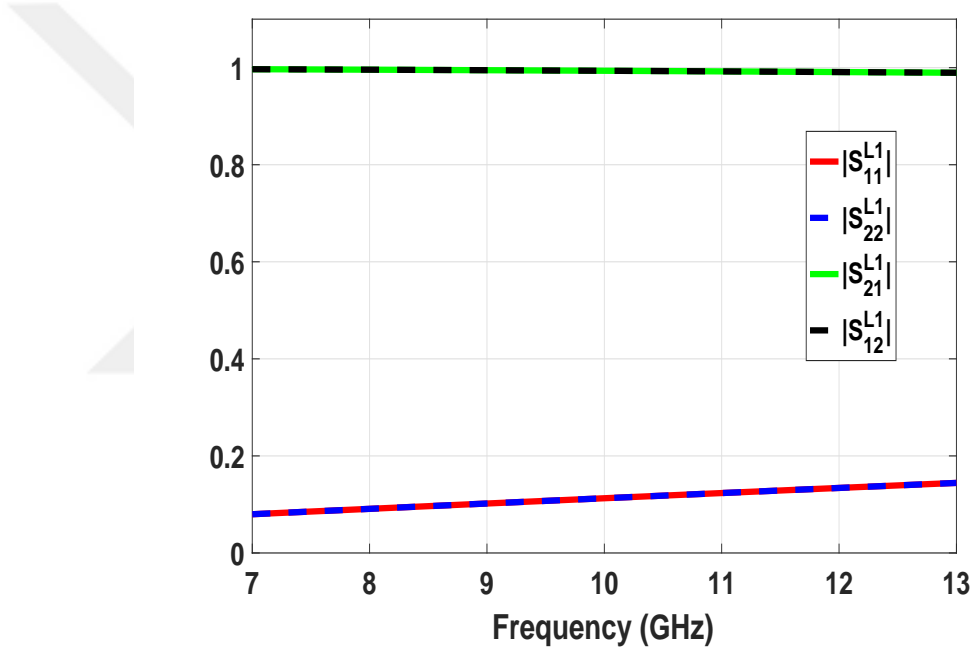


Figure 3.4 Magnitudes of simulated forward and backward reflection and transmission S-parameters of the Teflon sample with length $L_1 = 1.00$ mm.

Moreover, it is noted from Fig. 3.6(a) and Fig. 3.7(a) that the magnitudes of S_{21} and S_{12} considerably reduce to zero around frequency regions 4.50 – 5.30 GHz and 5.85 – 6.65 GHz which indicates the resonance behaviour of the chiral MM slab. Then, from the obtained simulated S-parameters of the two different configurations in Figs. 3.4 and 3.7, the proposed extraction algorithm incorporating near-field effects was applied to retrieve Γ_1 and Γ_2 using equations (3.5)-(3.11).

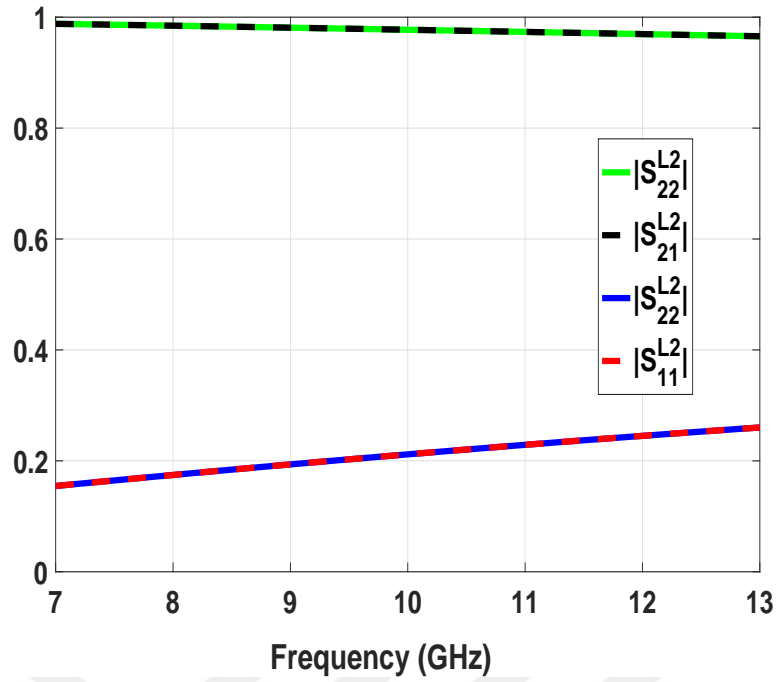


Figure 3.5 Magnitudes of simulated forward and backward reflection and transmission S-parameters of the Teflon sample with length $L_1 = 2.00$ mm.

Figs. 3.8 illustrate the real, imaginary and magnitude parts of the retrieved Γ_1 and Γ_2 coefficients for the Teflon sample. To validate accuracy of our proposed method, the Fresnel reflection coefficient Γ (from air to MM slab) was also retrieved by using the extraction method [36], which assumes that $\Gamma = \Gamma_1 = -\Gamma_2$ and does not take into account the near-field effects.

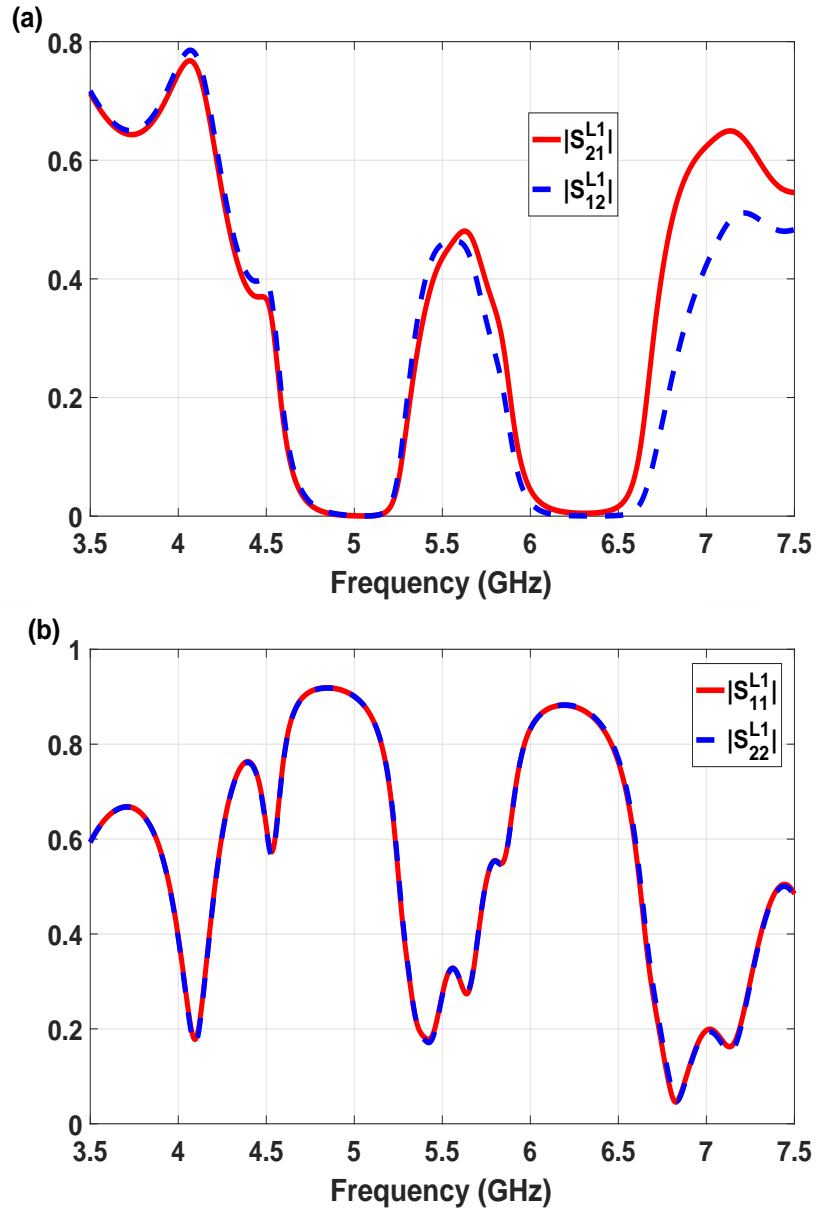


Figure 3.6 Magnitudes of simulated forward and backward (a) transmission and (b) reflection S-parameters of the chiral MM slab with length of $L_1 = 50$ mm (5 cells).

The real and imaginary parts of the extracted Γ by the method [36] are also shown in Fig. 3.9(a) and 3.9(b). From the dependencies in Figs. 3.9(a) and 3.9(b), the following conclusions can be extracted. Initially, although the real and imaginary parts of Γ_1 of the Teflon sample are identical to those of Γ , real and imaginary parts of Γ_2 are negative of those of Γ . This property validates the our proposed method because near-field effects does not appear around the surface of the Teflon sample.

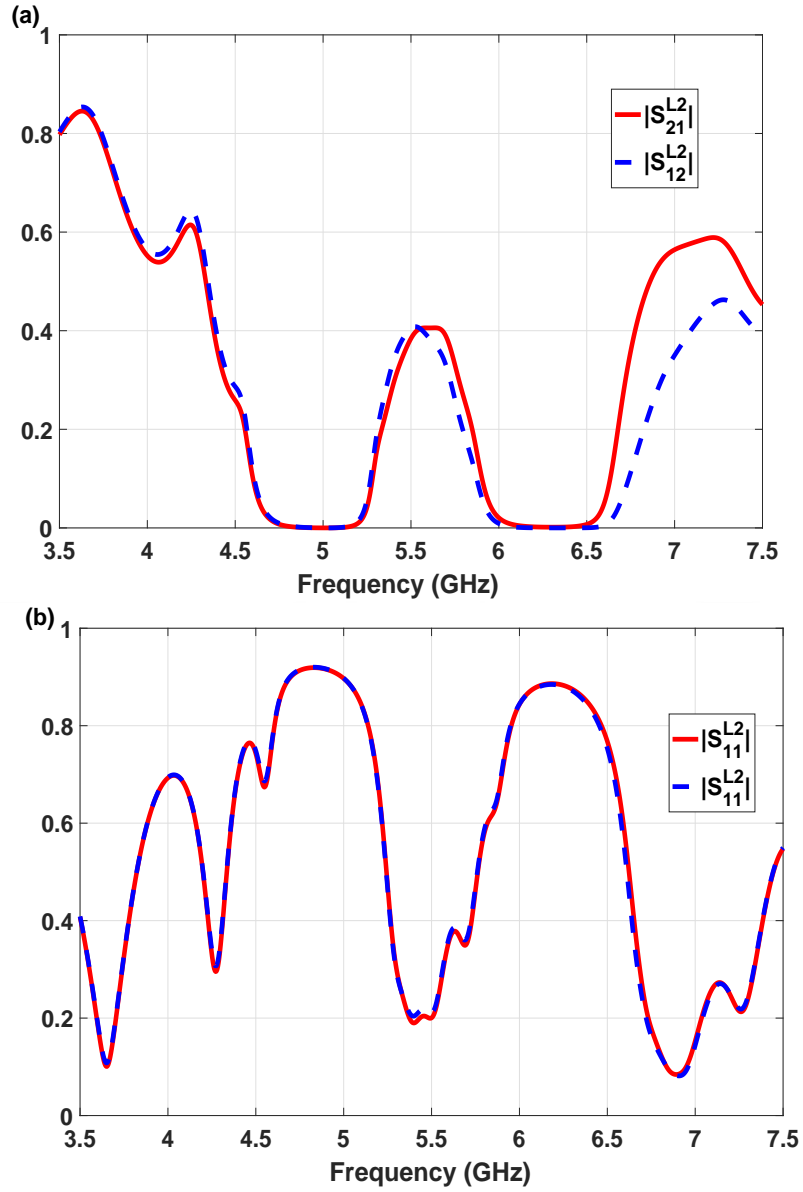


Figure 3.7 Magnitudes of simulated forward and backward (a) transmission and (b) reflection S-parameters of the chiral MM slab with length of $L_1 = 60$ mm (6 cells).

Second, it is noted from Fig. 3.9 that the real and imaginary parts of Γ_1 of the chiral MM slab are nearly the same with Γ over the whole analyzed frequency bands. Nevertheless, the real and imaginary parts of Γ_2 of the chiral MM slab are different and independent from the coefficient Γ especially away from the resonance regions (4.50 – 5.30 GHz and 5.85 – 6.65 GHz).

In addition, in the study of isotropic and bi-anisotropic MM slabs similar effect was also noted as in [43, 44, 57, 59]. This can be explained by the accumulation of surface currents around the left and right surfaces of the analyzed chiral MM slab. For that reason, the importance of near-field effect appears clearly on the extraction of electromagnetic properties of chiral MM slabs.

Third, while over the whole frequency band magnitudes of Γ_1 and Γ are similar for the chiral MM slab, magnitudes of Γ_2 and Γ are different especially away from the resonance regions which can be seen in Fig. 3.10(b).

Fourth, it is noted from Fig. 3.10 that $|\Gamma_1|$ and $|\Gamma_2|$ should be less than unity over the whole band; however, in Fig. 3.10(b) $|\Gamma_2|$ is larger than unity over the resonance regions. The circumstance that $|\Gamma_2| > 1$ over resonance regions can be explained by the fact that the chiral MM slab is a resonating structure and at its resonance regions higher Bloch modes inside and over the surface of chiral MM slab can be present.

Finally, from the Fig. 3.9(b) and Fig. 3.10(b) one can realize that the value of $|\Gamma_2|$ greater than unity. It seems that this is the violation of the passivity principle; but $|S_{21}|$, $|S_{12}|$, S_{11} and $|S_{22}|$ in Fig. 3.6 and Fig. 3.7 are both less than unity, verifying the forward problem.

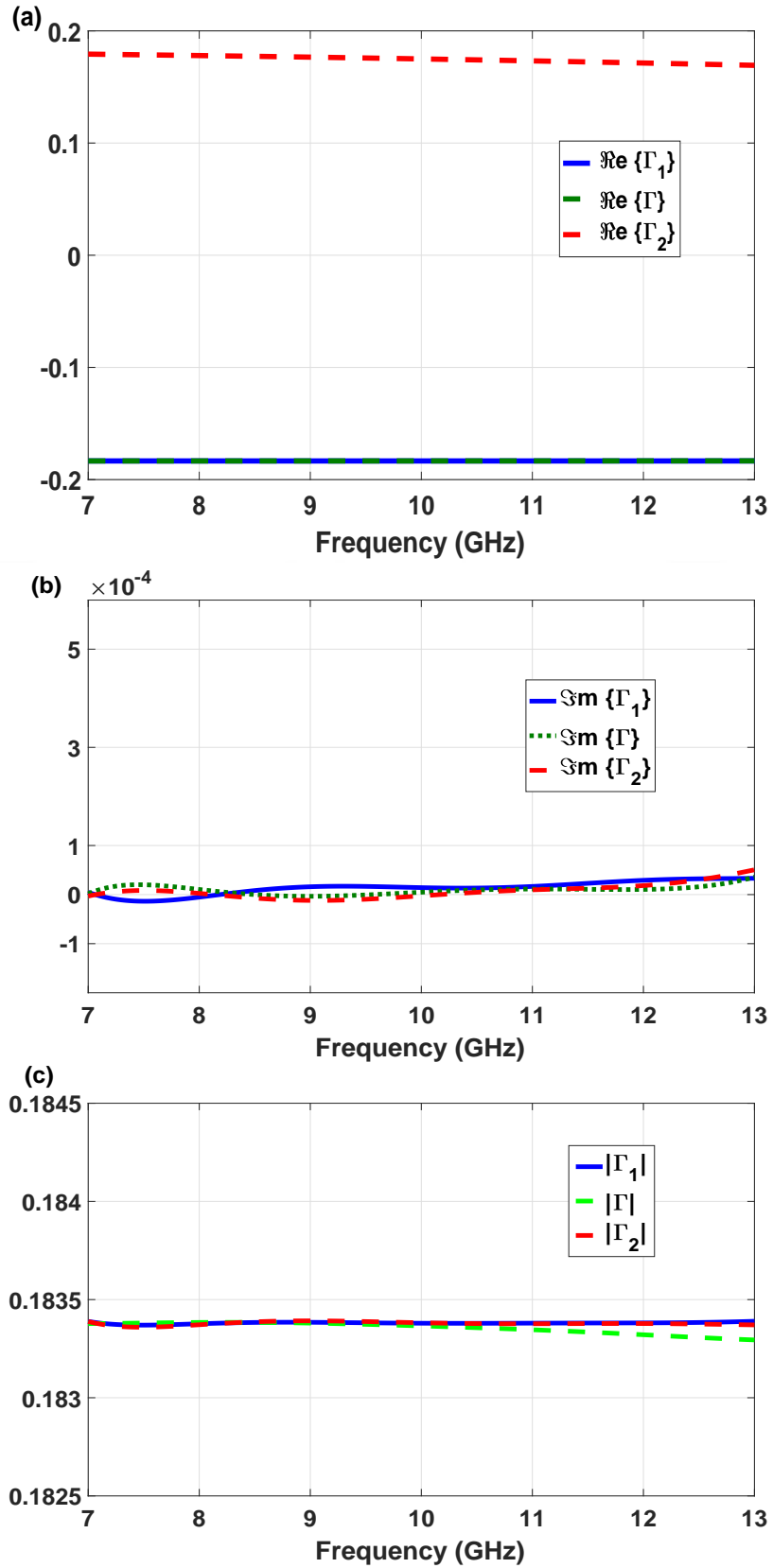


Figure 3.8 Extracted Γ_1 (proposed), Γ_2 (proposed), and Γ [36] of the Teflon sample by using our method and the method in [36]: (a) Real part, (b) Imaginary part and (c) Magnitude.

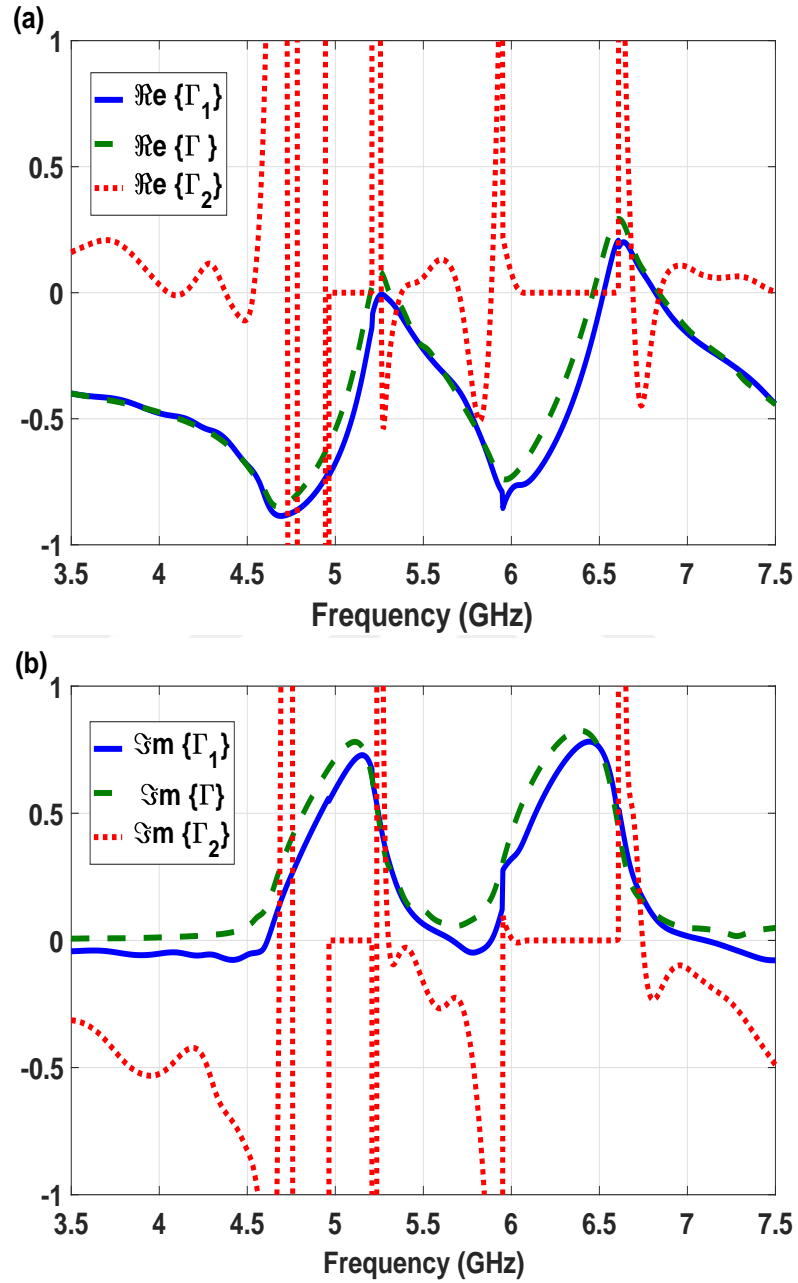


Figure 3.9 Extracted Γ_1 (proposed), Γ_2 (proposed), and Γ [36] of the chiral MM slab or $L_1 = 50$ mm (5 cell) and $L_2 = 60$ mm (6 cell) by using our method and the method in [36]: (a) Real part and (b) Imaginary part.

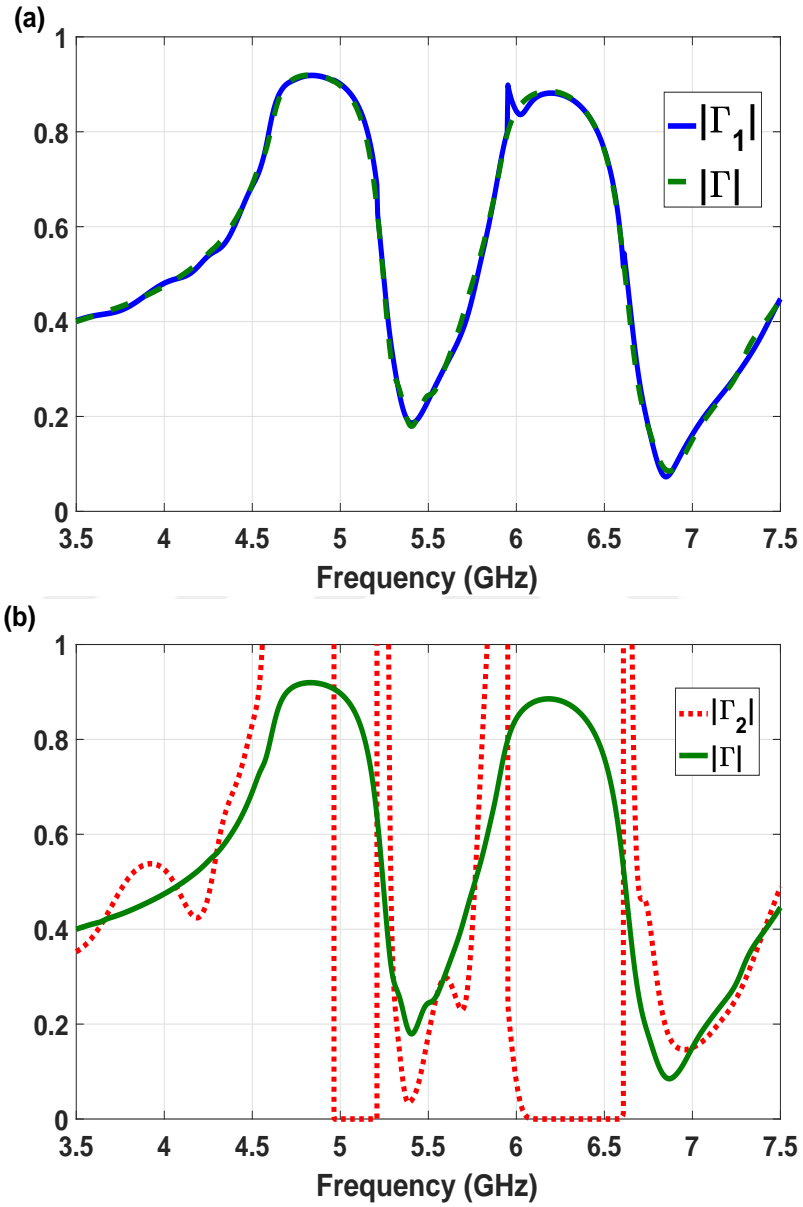


Figure 3.10 Magnitudes of chiral MM slab by using our method and the method in [36] (a) Γ_1 (proposed) and Γ [36] and (b) Γ_2 (proposed) and Γ [36].

CHAPTER 4

CHARACTERIZATION AND REALIZATION OF CHIRAL METAMATERIALS

4.1 Introduction

In addition to study of near-field effects in the previous chapter, a new type of crescent-shaped chiral MM structure has been proposed and its optical activity and chirality properties are examined with comparing the parameters of the U-shaped [37] and cross-shaped [38] MMs known in the literature. In order to validate the derived equations, we will use different chiral unit cells for comparisons such as U-shaped [37], cross-shaped [38] and the proposed crescent shaped [41]. These configurations will be utilized in detail for exact their characterization and realization.

Simulations were performed in the microwave frequency range, specifically from 2 GHz to 13 GHz. To compile simulations, frequency domain solver and free space conditions were chosen. Unit cell boundary conditions were selected in the electric and magnetic field directions. Time dependence in this chapter was assumed to be the time harmonic form $e^{j\omega t}$ and the propagation direction was selected in the \hat{z} direction.

In obtaining simulation results for the U-shaped chiral MM, the geometrical arrangement and dimensions in the study of [37] were taken. Furthermore, simulation results for the cross-shaped chiral MM, the geometrical arrangement and dimensions in [38] were considered throughout in this thesis.

4.2 Investigation of U-shaped, Cross-shaped and Crescent-shaped Chiral MM

We will first describe the U-shaped, cross-shaped, and crescent-shaped configurations briefly in next subsections and give some geometrical and constructional details that we have used in our simulation study. Simulations for each MM slab were performed by 3-D electromagnetic simulator program-CST Microwave Studio (frequency domain solver).

Using the fundamental transmission and reflection scattering coefficient parameters from simulation program, all extracted parameters related to chiral MM phenomena will be demonstrated in coming subsections. The configuration mentioned and proposed in Chapter 3 in Fig. 3.1 will be analyzed. Toward this end, we will go on with detail informations about geometrical arrangements and dimensions of the examined configurations. Then, response behavior of reflection and transmission coefficients and the rest of other parameters related to chirality parameters will be supplemented step by step in coming subsections.

4.2.1 Sample 1: U-shaped Chiral MM

In our first analysis, the U-shaped MM structure in the study [37] was examined, shown here for convenience and simplicity (Fig. 3.3).

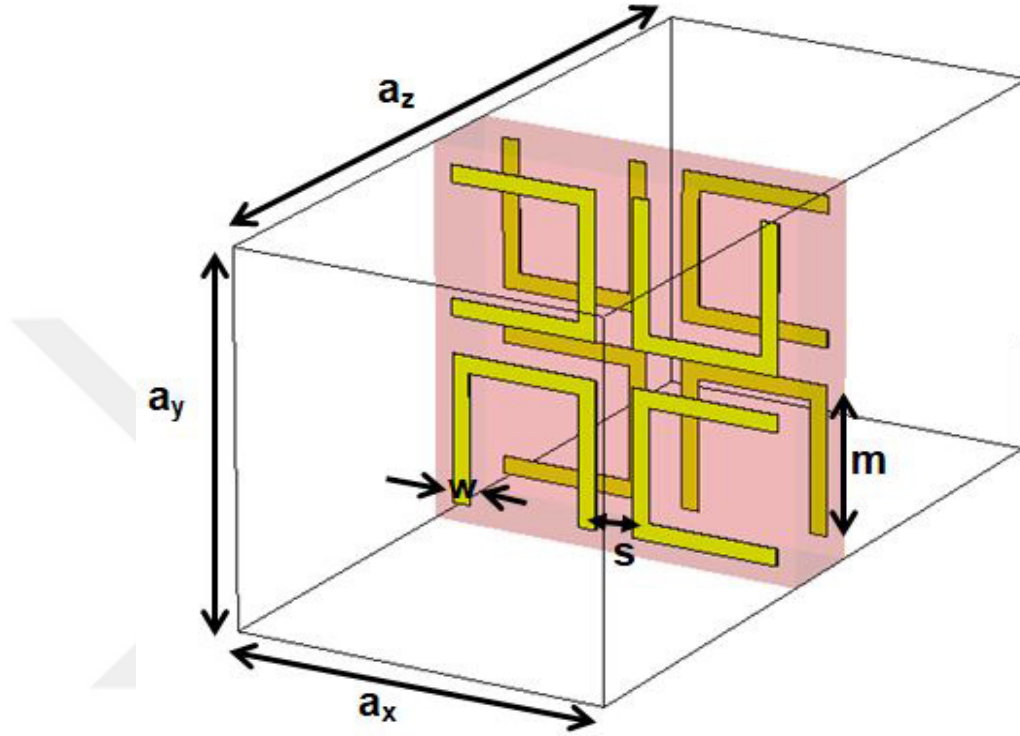


Figure 4.1 Geometrical properties of the examined chiral MM cell with U-shaped split-ring-resonators [37].

The properties of the U-shaped SRR structure are: the volume dimensions of the cell are $a_x = 15$ mm, $a_y = 15$ mm, and $a_z = 10$ mm. The length of the outer ring is $m = 6$ mm, the separation between the rings is $s = 1.5$ mm, linewidth of each ring is $w = 0.7$ mm, and the copper used for SRRs has a thickness of 0.03 mm. The thickness of the substrate is $d = 1.6$ mm and has a dielectric constant of $\epsilon_r = 4$ with a loss tangent of 0.025. All dimensions of the simulated cell are similar to those in [35].

4.2.2 Sample 2: Cross-shaped Chiral MM

In our second analysis, the cross-shaped SRR structure as shown in Fig. 4.2 was considered. That investigated cross-shaped SRR structure was taken from the study [38].

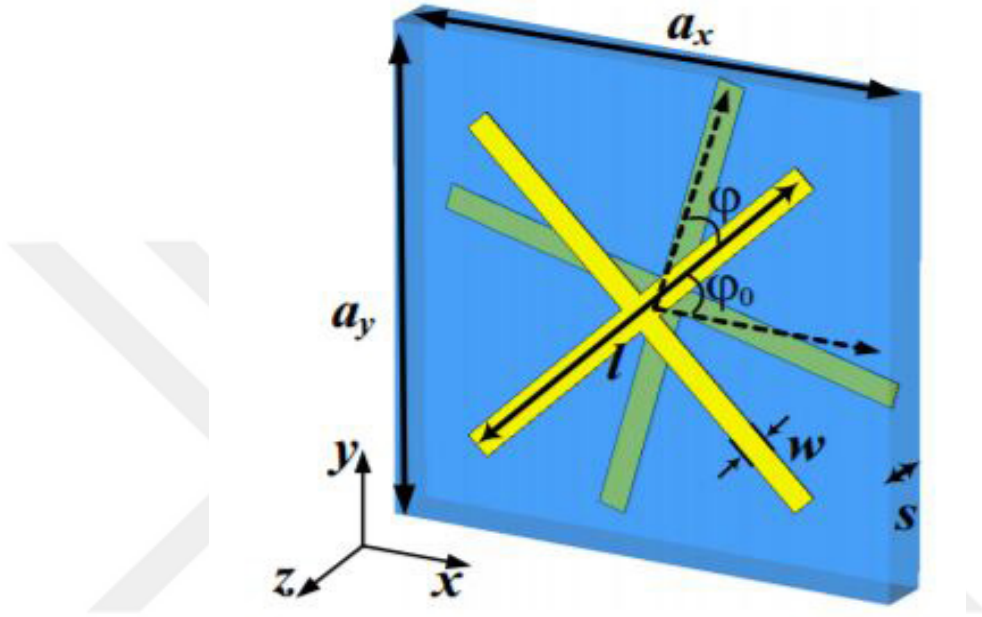


Figure 4.2 Geometrical properties of the analyzed chiral MM cell with cross-shaped split-ring-resonators [38].

The properties of cross-shaped SRR structure are: the volume dimensions of cell are $a_x = 15$ mm, $a_y = 15$ mm, and $a_z = 11.5$ mm. The length of each cross wire is $l = 14$ mm, linewidth of each line is $w = 0.8$ mm and the copper used for SRRs has a thickness of 0.03 mm. The thickness of substrate is $d = 1.6$ mm and has a dielectric constant of $\epsilon_r = 4.5$ with loss tangent of 0.033. The angle $\phi_0 = 45^\circ$ with respect to x -axis and the angle between the front and back side linewires is rotated as $\phi = 15^\circ$. All parameter dimensions of the simulated cell are similar to those in [38].

4.2.3 Sample 3: Crescent-shaped Chiral MM

Fig. 4.3 illustrates the schematic configuration of the proposed chiral MM cell which is new in the literature. It is double layered and each unit cell face consists of four crescent shaped rings without any symmetry on FR-4 board. Each crescent shaped ring is made by the difference of two circular disks; that is, smaller disk has radius of $r_{in} = 2.4$ mm and bigger disk has radius of $r_{out} = 3.0$ mm.

To obtain the crescent shaped ring, initially we put smaller disk on the inner tangent of bigger disk and then by making Boolean algebra subtraction in CST microwave studio program. Remaining small fragment slits on the tangential side are also deleted with a rectangular line of dimensions $m = 3.2$ mm x 0.5 mm in the y -direction.

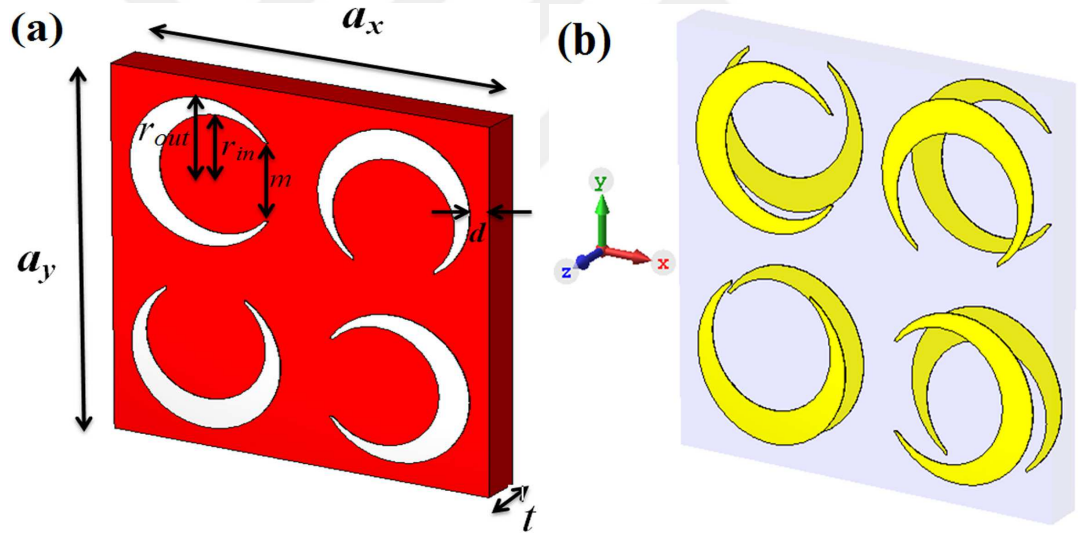


Figure 4.3 Geometrical properties of analyzed configurations for the chiral MM cell with crescent-shaped split-ring-resonators (a) front view and (b) perspective view [41].

The relative dielectric constant of the substrate is 4.3 with loss tangent of 0.025. The unit-cell dimensions are $a_x = a_y = 15.0$ mm, $a_z = 11.2$ mm, $t = 1.6$ mm, thickness of the copper is $t_m = 0.03$ mm. Each crescent shape is rotated by 90 degrees with respect to its neighbour and does not have mirror symmetry with its opposite sides. All parameter dimensions of the simulated cell are similar to that in publication [41].

4.3 Characterization of Chiral MM

In this section, our purpose is to examine chiral properties (optical activity and chirality) of the proposed crescent-shaped MM cell in reference to corresponding properties of the U-shaped and cross-shaped MM cells. Toward this end, all the equation in Chapter 2 will be applied to extract the chiral properties of these MM slabs.

4.3.1 Forward Transmission Coefficients (S_{21}) of Chiral Medium

For the proposed chiral MM structure in Fig. 3.1, the scattering parameter for forward transmission coefficient is denoted by S_{21} and its simulation results are illustrated in Fig. 4.4.

The main important property of a chiral MM is having asymmetric transmission coefficients in forward and backward directions in contrast to isotropic conventional materials with symmetrical transmissions. When we glance at the simulated figures related to transmissions in Fig. 4.4 and 4.5, especially at resonance regions transmission behaviors are different due to the property of chirality.

According to different simulated chiral configurations, the resonance frequency regions for U-shaped can be seen at 5.1 GHz and 6.35 GHz in the whole range of between 3.5-7.5 GHz. For cross-shaped the resonances are around 6.35 GHz and 7.4 GHz in the whole range of between 5-9 GHz, and for the proposed crescent-shaped configuration, resonances are nearly at 9 GHz and 11.2 GHz in the whole range of between 7-13 GHz.

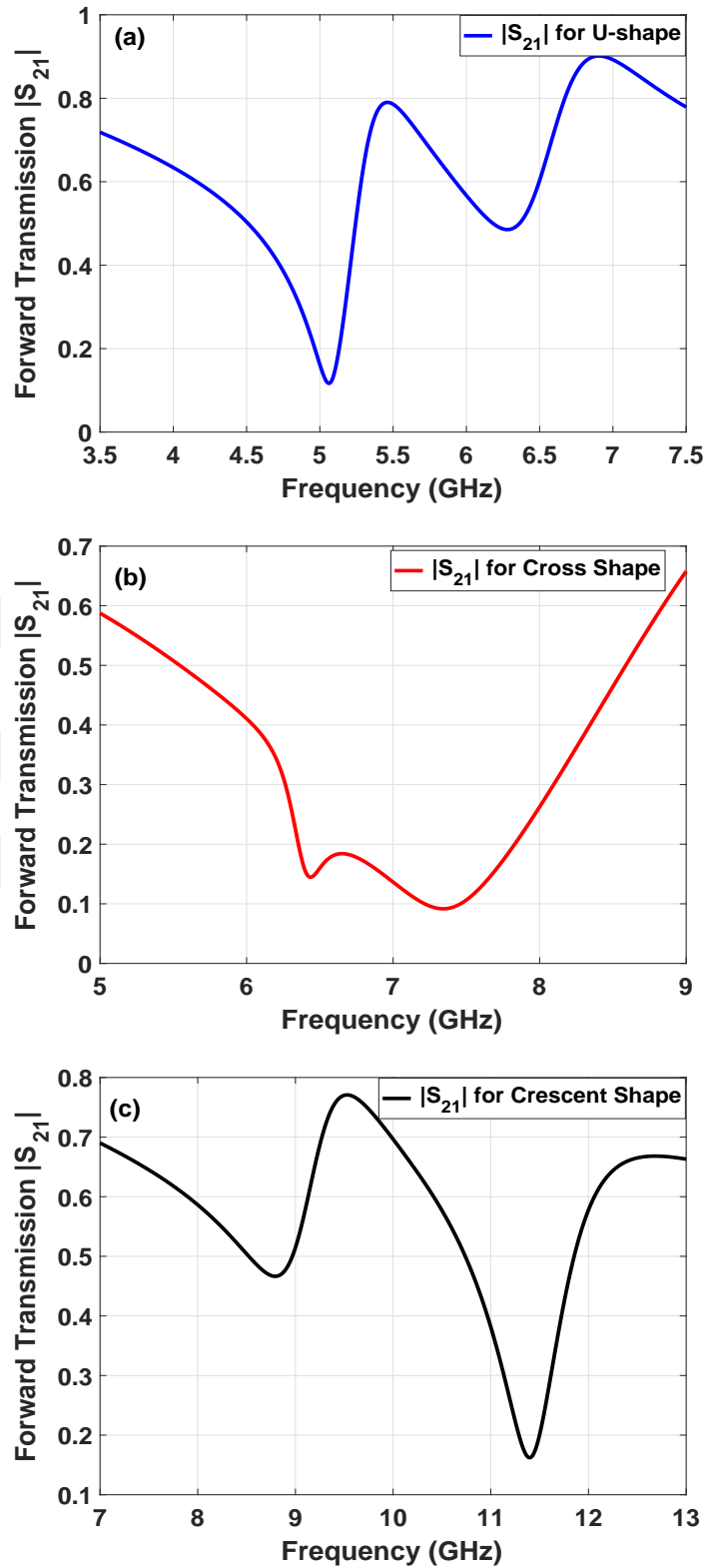


Figure 4.4 Simulated absolute forward transmission coefficients for the configuration of (a) U-shaped, (b) Cross-shaped and (c) Crescent-Shaped.

4.3.2 Backward Transmission Coefficients (S_{12}) of Chiral Medium

According to Fig. 3.1, the scattering parameter for backward transmission coefficient is denoted by S_{12} and its simulation responses are demonstrated in Fig 4.5. When we look at the simulated backward transmission coefficients in Fig. 4.5, response behaviors of transmissions have consistency with the forward transmissions simulated in Fig. 4.4. Contrary to isotropic conventional materials and bi-anisotropic MMs, backward transmissions are different than the forward transmissions which can be seen in the Fig. 4.4 and 4.5. As a result of this property, circular dichroism and optical activity can be seen in chiral structures.

4.3.3 Forward Reflection Coefficients (S_{11}) of Chiral Medium

The reflection scattering parameter for forward reflection coefficient is denoted by S_{11} and its simulation results are shown in Fig. 4.6. Generally, in chiral structures the forward and backward reflections ideally should be the same and in our simulations reflections are nearly the same except in some resonance regions where there are little differences. When we compare the simulation results of reflections from the Fig. 4.6 and 4.7, among the three configurations proposed crescent-shaped is the best one for the ideal chiral case then the cross-shaped is better than the U-shaped case.

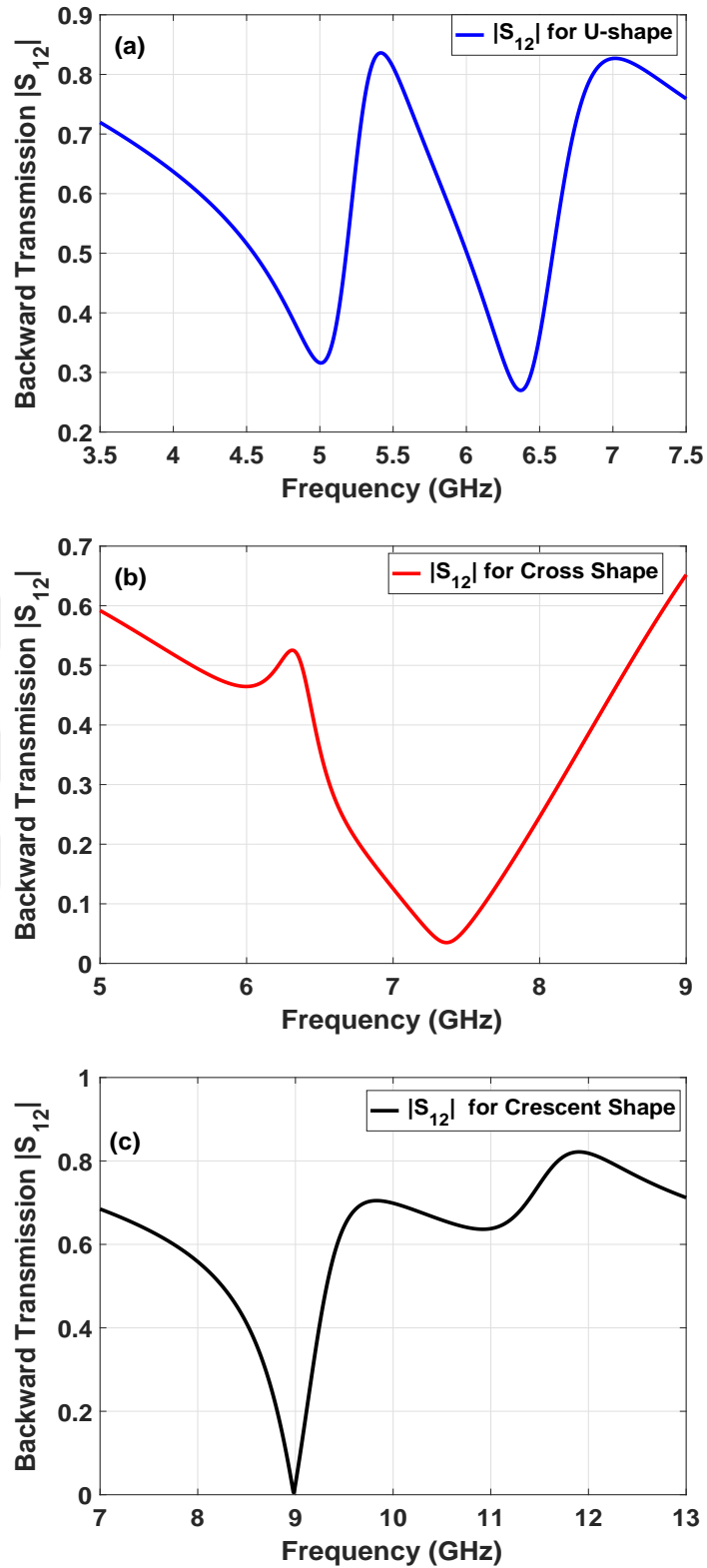


Figure 4.5 Simulated absolute backward transmission coefficients for the configuration of (a) U-shaped, (b) Cross-shaped and (c) Crescent-Shaped.

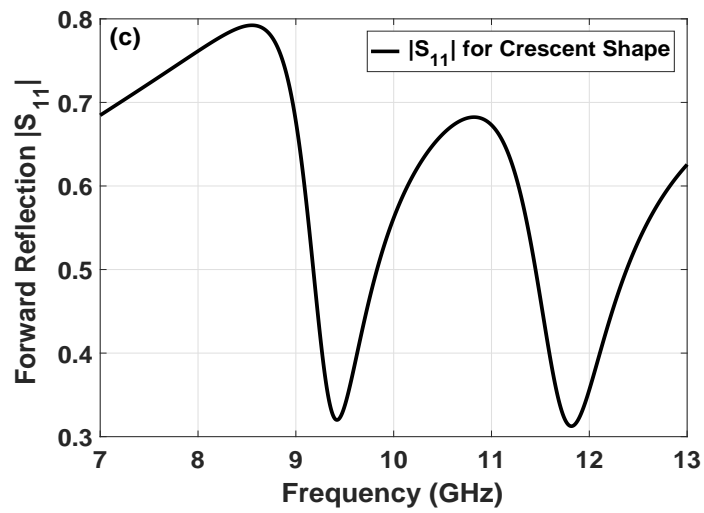
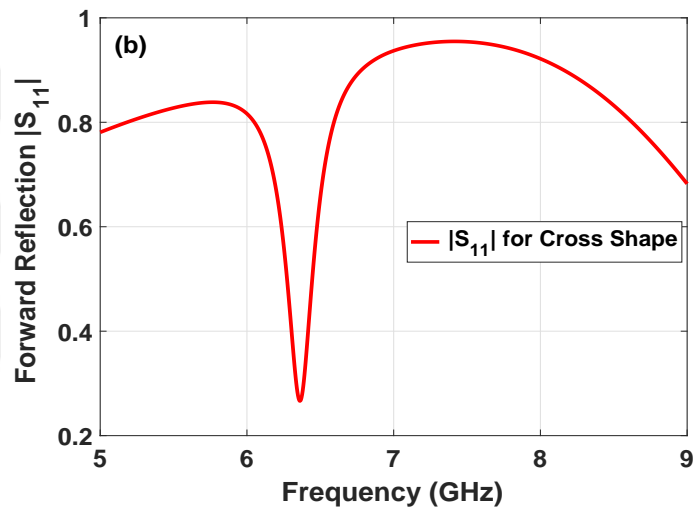
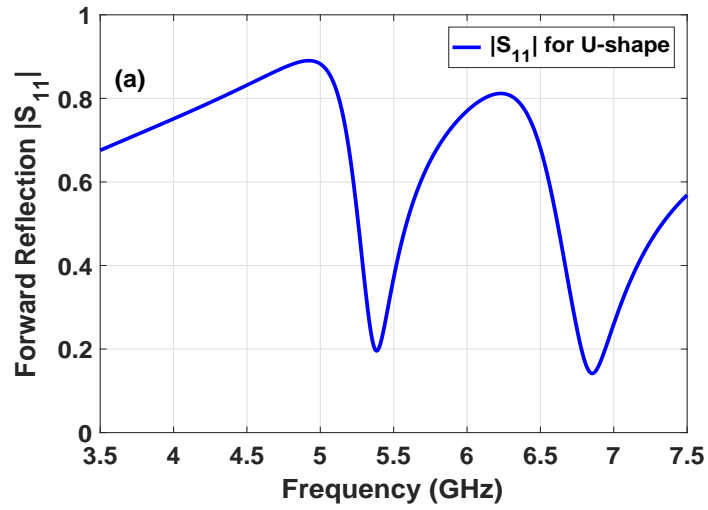


Figure 4.6 Simulated absolute forward reflection coefficients for the configuration of (a) U-shaped, (b) Cross-shaped and (c) Crescent-Shaped.

4.3.4 Backward Reflection Coefficients (S_{22}) of Chiral Medium

The scattering parameter for backward reflection is denoted by S_{22} and its response behaviors are illustrated in Fig. 4.7. If we look at the simulated backward reflection coefficients in Fig. 4.7, response behaviors of reflections have consistency with the forward reflections simulated in Fig. 4.6. Contrary to bi-anisotropic MMs, backward reflections are nearly the same with the forward reflections which can be seen in the Fig. 4.6 and 4.7.

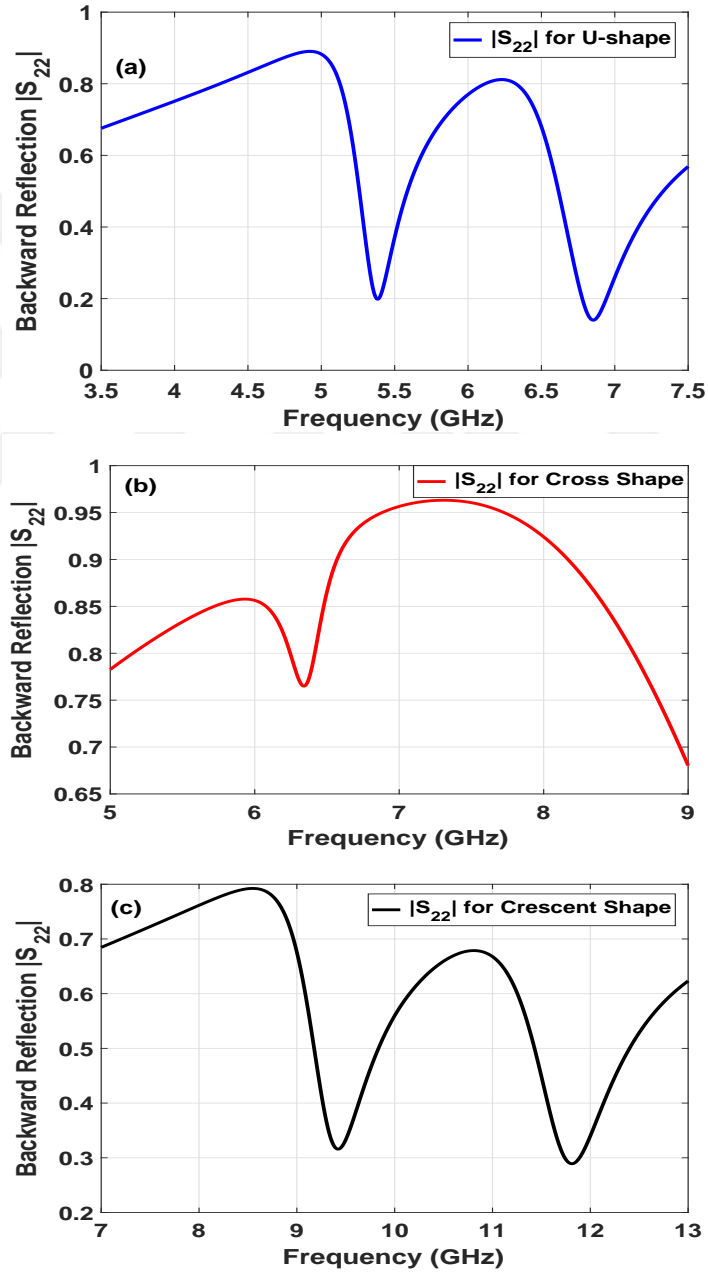


Figure 4.7 Simulated absolute backward reflection coefficients for the configuration of (a) U-shaped, (b) Cross-shaped and (c) Crescent-Shaped.

4.3.5 Azimuth Rotation Angle (θ) of Chiral Medium

The two important properties of chiral materials are optical activity and circular dichroism. When a linearly polarized plane wave passes through a chiral medium its polarization rotates and resulting in a optical activity. This polarization azimuth rotation angle of a elliptically polarized light is mathematically defined as in the equation (2.29) ($\theta = \frac{1}{2}[\arg(T_+) - \arg(T_-)]$), where T_+ and T_- indicate the transmission coefficients for RCP and LCP waves.

According to different simulated chiral configurations, the resonance frequencies for U-shaped are seen at 5.1 GHz and 6.35 GHz and for cross-shaped the resonances are around 6.35 GHz and 7.4 GHz. Next, for the proposed crescent-shaped configuration, resonances are nearly 9 GHz and 11.2 GHz. When we look at the Fig. 4.8 (c), the resonance frequency of crescent shape at 11.2 GHz is sharper than the first resonance at 9 GHz.

4.3.6 Elliptical Angle (η) of Chiral Medium

The second important property of a chiral medium is the circular dichroism which arises from the different absorption and distortion of RCP and LCP waves while interacting with chiral particles. The circular dichroism is defined in terms of the absolute difference of transmitted powers as mentioned in the equation (2.30) ($\eta = \frac{1}{2}\tan^{-1}\left(\frac{|T_+|^2 - |T_-|^2}{|T_+|^2 + |T_-|^2}\right)$).

According to simulated results in Fig. 4.9, we can extract that the response behavior of configurations are nearly the same and compatible with each other. In addition, it is seen that pure optical effect occurs at the middle of the two resonance frequencies where elliptical angle corresponds to ($\eta = 0$); that is, with a rotated azimuth angle (θ) linear incident polarization does not change through the transmission because it is still linear polarization. Moreover, from the figures, we note that the resonance points in the Fig. 4.8 have consistent with the Fig. 4.9.

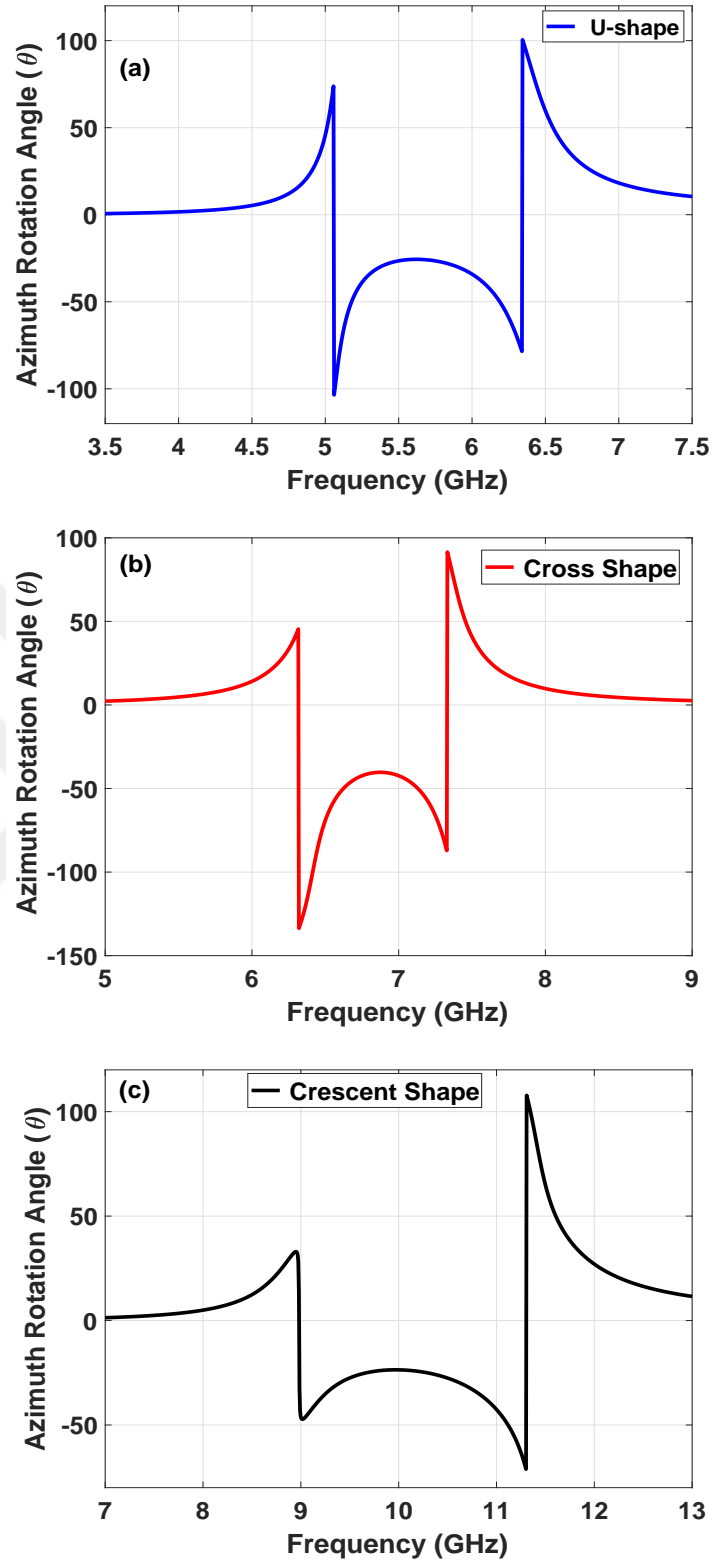


Figure 4.8 Simulated optical activity of azimuth rotation angle for the configuration of (a) U-shaped, (b) Cross-shaped and (c) Crescent-Shaped.

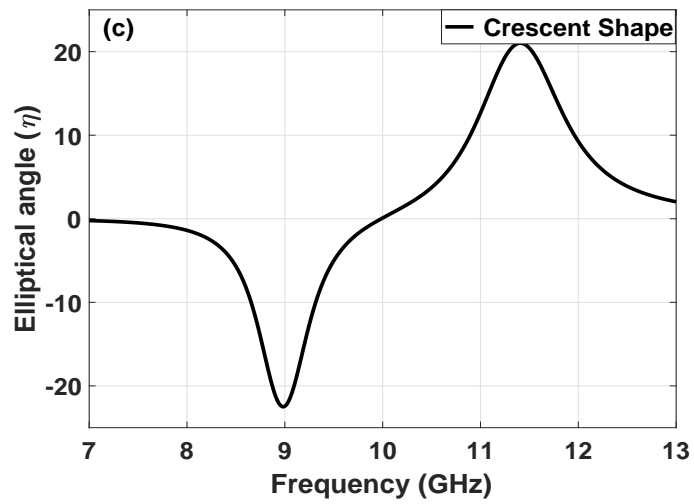
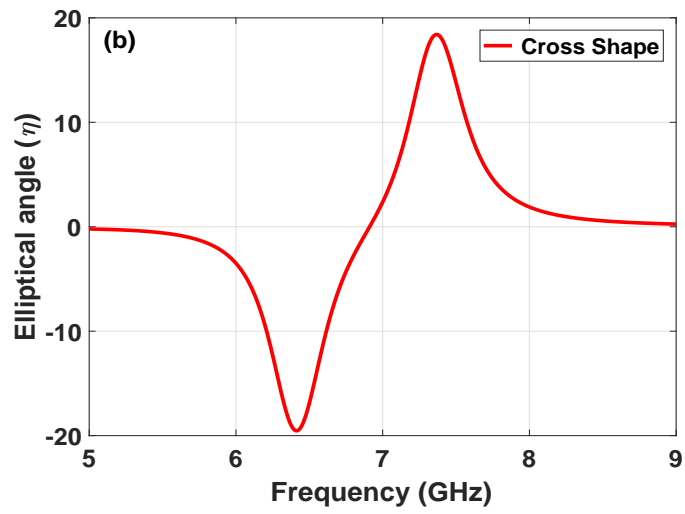
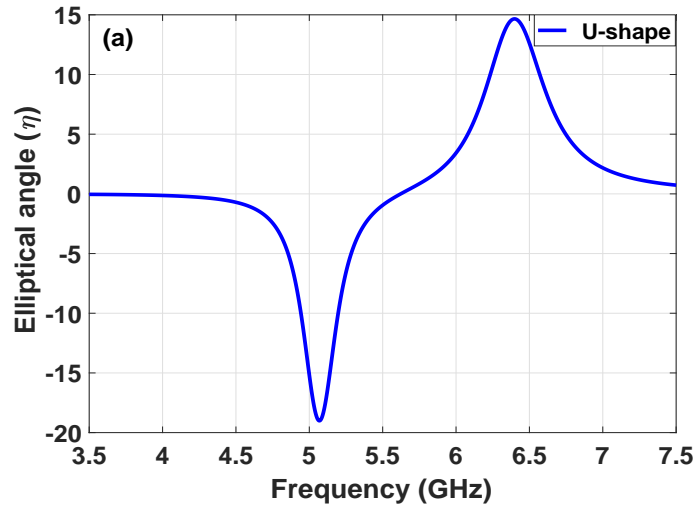


Figure 4.9 Simulated elliptical angle of circular dichroism for the configuration of (a) U-shaped, (b) Cross-shaped and (c) Crescent-Shaped.

4.3.7 Chirality Constant (κ) of Chiral Medium

The main property of chiral MM is determined by the coefficients of chirality parameter which is dependent on the forward and backward transmission variables as demonstrated in the equation (2.46). The value of chirality constant (κ) determines the robustness of the material properties. In addition, the cross-coupling between electric and magnetic fields leads to strong chirality through the medium and this can be explained by the surface current distribution at the resonance regions [55].

As seen from the Fig. 4.10, the value of chirality parameters are enough to demonstrate optical activity and circular dichroism because the value of κ is more than 1 and can be assumed to illustrate high chirality properties [54]. Furthermore, Fig. 4.10(a) and Fig. 4.10(b) have a bandwidth of approximately 1 GHz while Fig. 4.10(c) has more than 2 GHz. In addition, first and second κ values at resonance points of Fig. 4.10(a) and Fig. 4.10(b) are nearly the same whereas Fig. 4.10(c) demonstrates κ value at 11.2 GHz is two times more than the first resonance point of 9 GHz. This can be explained that chirality around 11.2 GHz is more dominant than at 9 GHz.

4.3.8 First Reflection Coefficient (Γ) of Chiral Medium

After calculating the scattering parameters S_{21} , S_{12} , S_{11} and S_{22} demonstrated in Figs. 4.4, 4.5, 4.6 and 4.7 which represent the whole response of the material transmissions and reflections. Those four parameters depend on the first reflection parameter of Γ value which also should be satisfied by the condition of passivity which is $|\Gamma| \leq 1$.

As seen from the Fig. 4.11, the whole simulated configurations satisfy the passivity condition of $|\Gamma| \leq 1$; that is, all absolute Γ values are less than unity. Furthermore, the main point for the extraction of property of materials depends on the the value of Γ . For that reason, determining the value of Γ exactly is very important for the retrieval of material properties such as refractive index, permittivity and permeability. In addition, the parameter of transmission (T) is dependent to branch index value whereas there is no any branch index ambiguity for determining the Γ value. For that reason, in the retrieval procedure of materials Γ should be first preferred than the transmission (T) parameter.

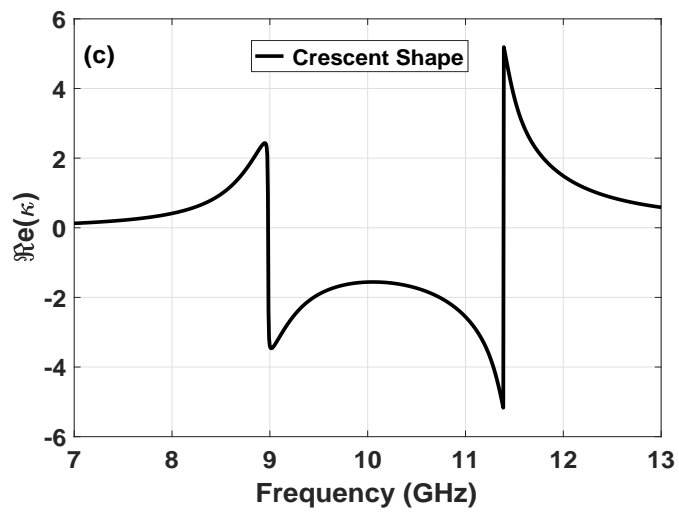
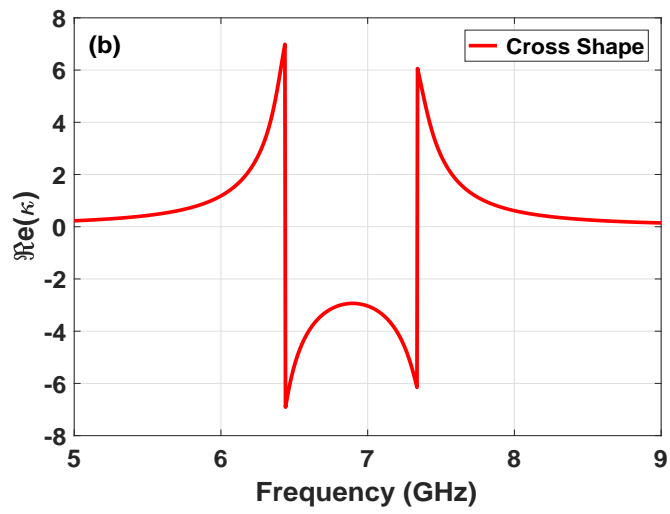
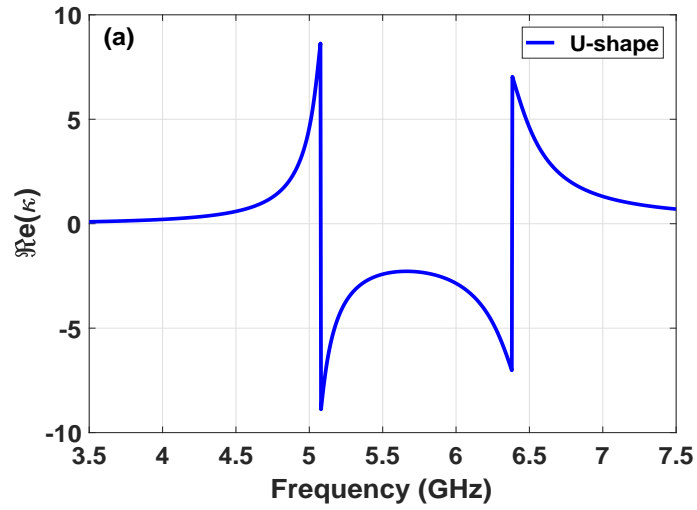


Figure 4.10 Simulated real value of chirality parameter $\Re(\kappa)$ for the configuration of (a) U-shaped, (b) Cross-shaped and (c) Crescent-Shaped.

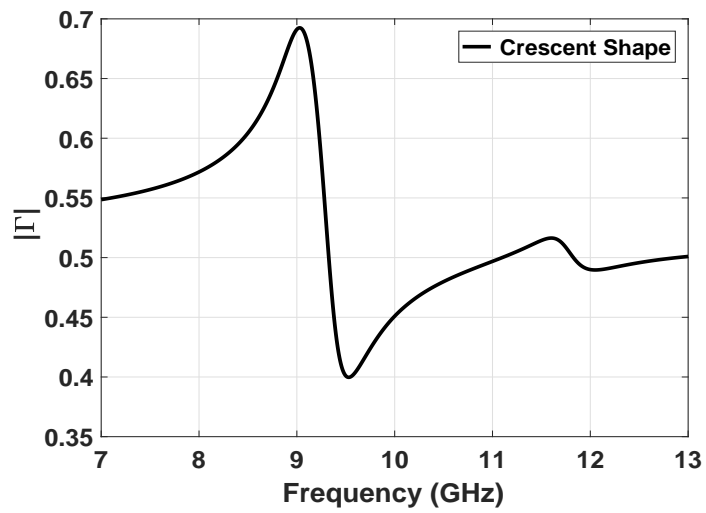
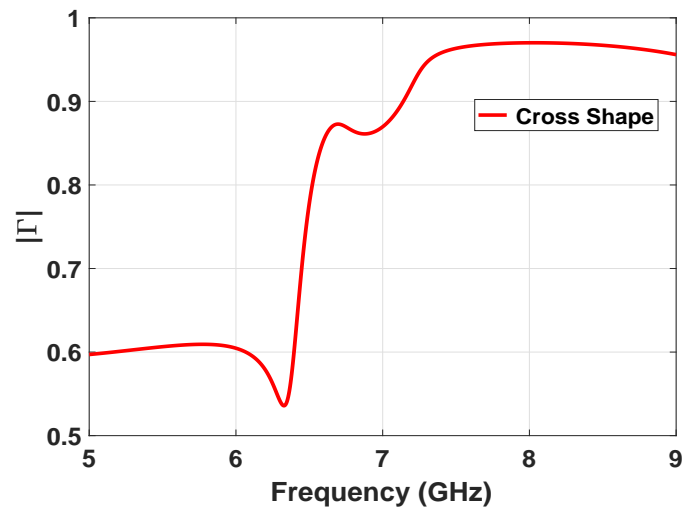
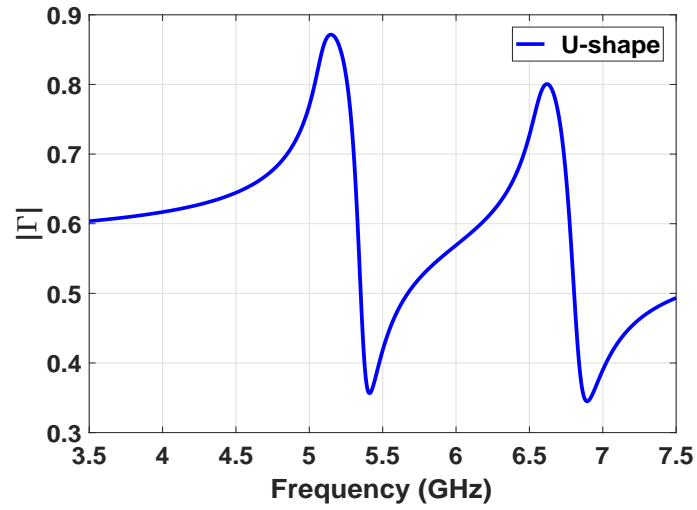


Figure 4.11 Simulated magnitude of first reflection coefficient $|\Gamma|$ for the configuration of (a) U-shaped, (b) Cross-shaped and (c) Crescent-Shaped.

4.3.9 Impedance (Z) of Chiral Medium

The impedance value is determined by the relation $Z = \frac{1+\Gamma}{1-\Gamma}$. From this relation it is seen that the first reflection Γ and impedance (Z) behaviors resemble to each other which can be seen from Fig. 4.11 and Fig. 4.12. For that reason, the impedance value is necessary for us to determine the refractive index correctly for RCP and LCP waves.

The impedance value for RCP and LCP waves is the same and does not change through the medium because forward and backward reflections are not different. In addition, the impedances can be calculated from the equation (2.40). However, the correct sign for square root in the equation (2.40) should be selected carefully according to principle of energy conservation as $\Re(Z) \geq 0$.

4.3.10 Refractive Index for RCP Waves (n_+) of Chiral Medium

In this subsection, the effective refractive index for the RCP waves is retrieved through the equation (2.41) ($n_{\mp} = \frac{i}{k_0 d} \left[\ln \left(\frac{1}{T_{\mp}} \left(1 - \frac{Z-1}{Z+1} R \right) \mp 2im\pi \right) \right]$), where m is the branch index to be determined for the plus sign of n . Furthermore, the correct branch index in the logarithm of equation (2.41) should be selected carefully according to principle of energy conservation which is $\Im(n) \geq 0$.

It is clearly seen that $\Re(n_+)$ value in Fig. 4.13 initially has a value of approximately 5 until the around the resonance region. In the resonance regions a negative refractive index is seen due to strong response of chirality parameters. In addition, as seen from the Fig. 4.13 strong chirality parameter pushes the refractive index to be zero.

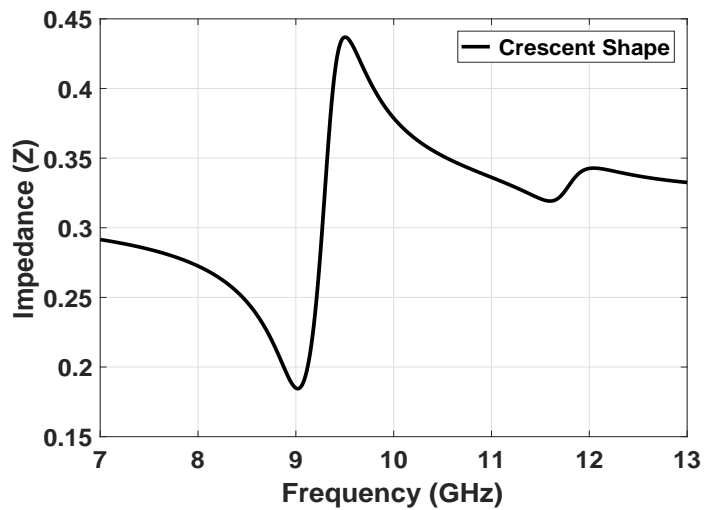
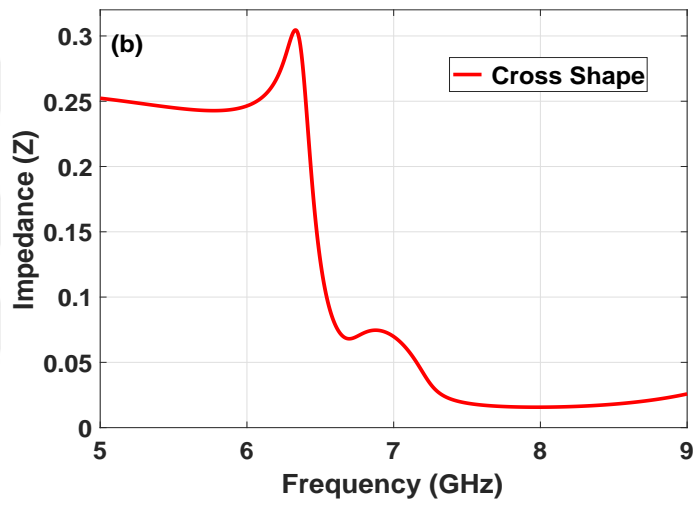
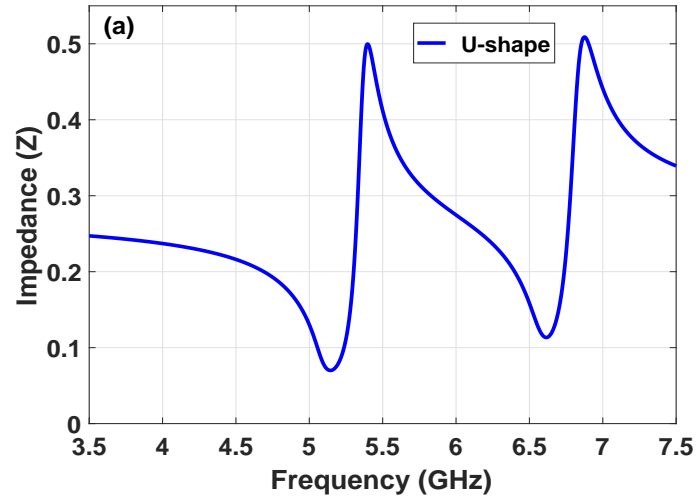


Figure 4.12 Simulated impedances Z for the configuration of (a) U-shaped, (b) Cross-shaped and (c) Crescent-Shaped.

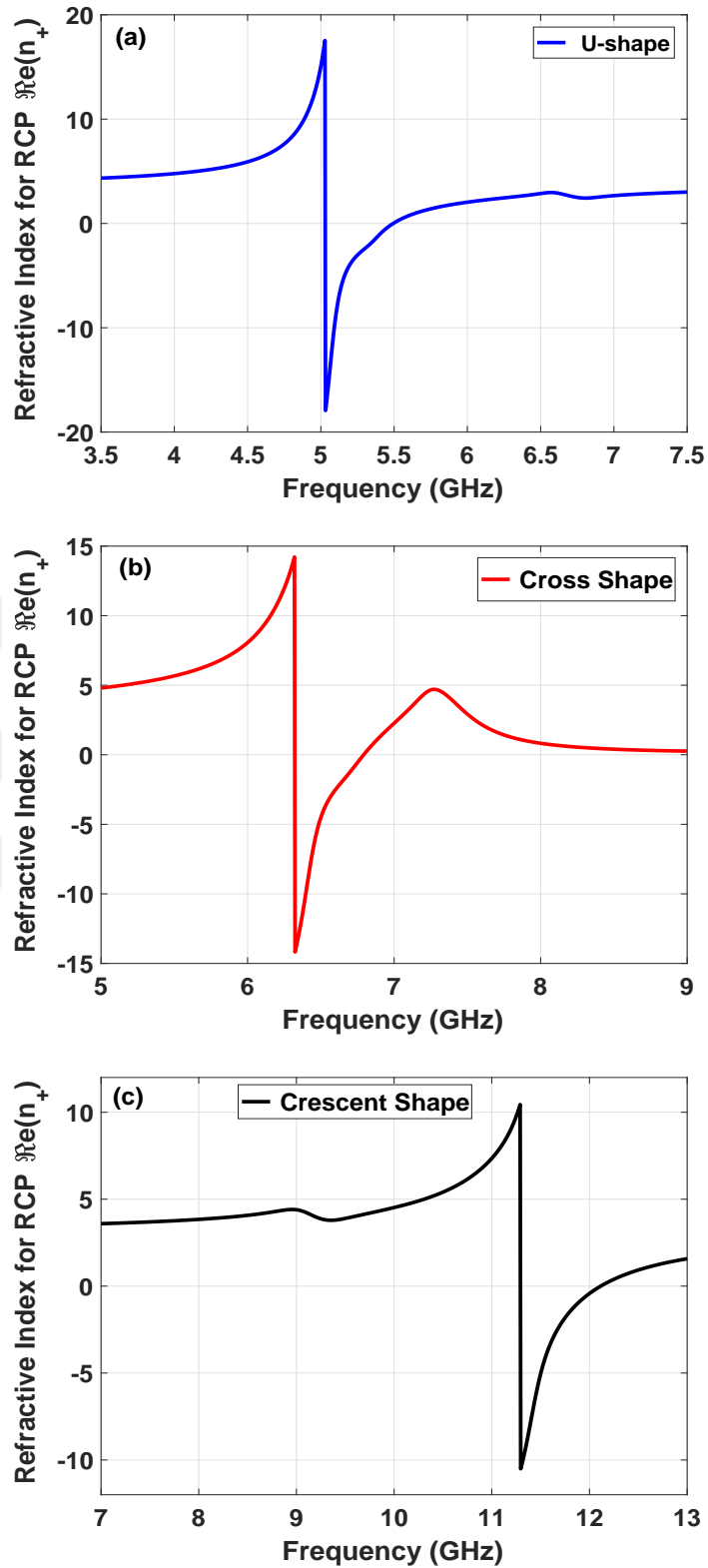


Figure 4.13 Simulated real value of refractive index for RCP waves $\Re(n_+)$ for the configuration of (a) U-shaped, (b) Cross-shaped and (c) Crescent-Shaped.

4.3.11 Refractive Index for LCP Waves (n_-) of Chiral Medium

The effective refractive indices for the LCP waves are retrieved through the equation (2.41) for the negative sign of n . As seen from the Fig. 4.14, the response behavior of refractive index for LCP waves is opposite the RCP waves shown in Fig. 4.13 with respect to resonance regions. For LCP, “ n_- ” is going to zero in the second resonance point while in RCP, “ n_+ ” is in the first resonance point. Moreover, according to RCP or LCP waves the impedance for chiral MMs does not change but refractive index is changing.

It is also noted that refractive index value for LCP and RCP are consistent with each other when the Fig. 4.13 and 4.14 are compared because the values of refractive indices are nearly the same except for resonance regions. In addition, as seen from the Fig. 4.14 that the response of n_- completes the other side of the Fig. 4.13, this demonstrates the symmetry of refractive index through the chiral medium.

4.3.12 Refractive Index (n) of Chiral Medium

In this section, the refractive index demonstrated for linearly polarization wave according to equation (2.43) ($n = (n_+ + n_-)/2$). As seen from the Fig. 4.15, the response behavior of “ n ” is total mean of Fig. 4.13 and 4.14. In addition, it can be seen that negative refractive index is achieved around the resonance regions in Fig. 4.15. Furthermore, the negative refractive indices were also achieved by the resonance regions of RCP and LCP waves as shown in Fig. 4.13 and 4.14.

Moreover, the refractive index for U-shaped and cross-shaped have two different negative value at resonance regions while crescent shape has one negative refractive index value only around 11.2 GHz. The response behavior of refractive index dependent on the value of chirality parameter (κ) because the medium has huge chirality value then the refractive index can lead to higher negative index values.

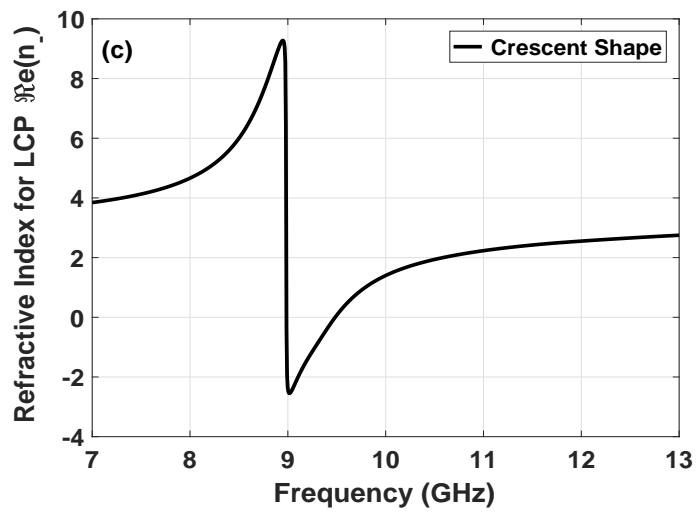
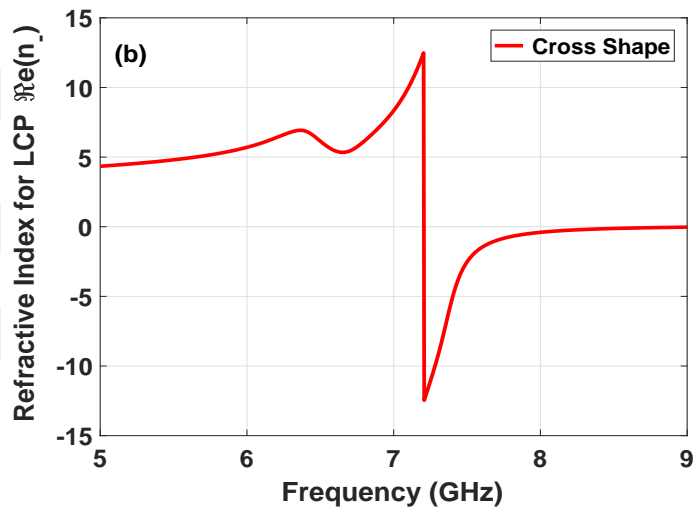
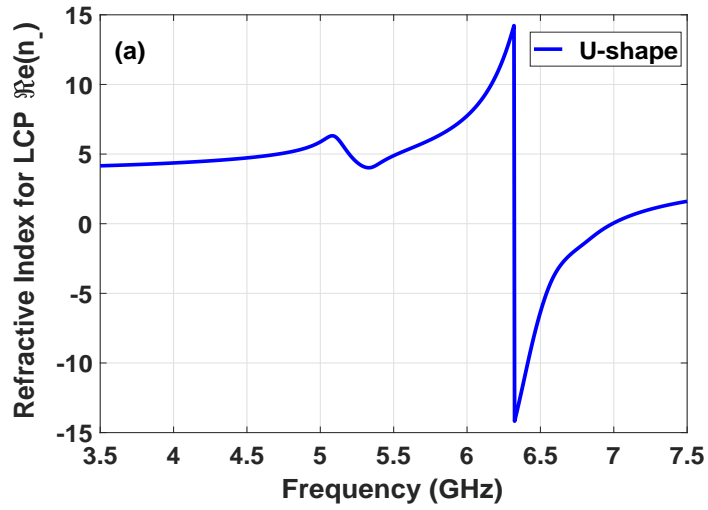


Figure 4.14 Simulated real value of refractive index for LCP waves $\Re(n_-)$ for the configuration of (a) U-shaped, (b) Cross-shaped and (c) Crescent-Shaped.

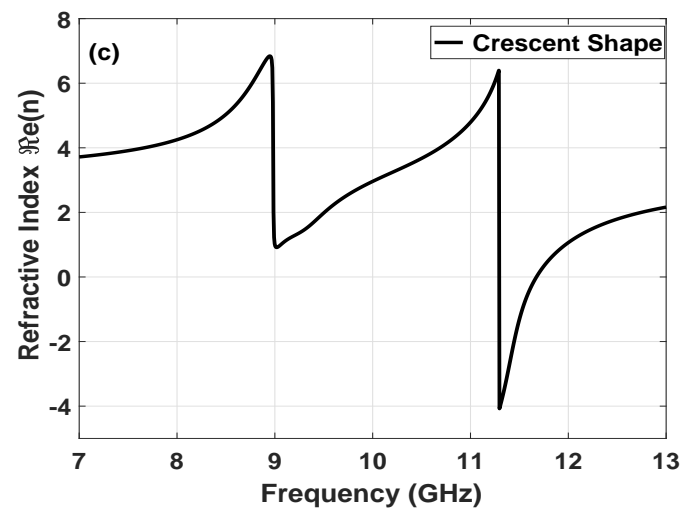
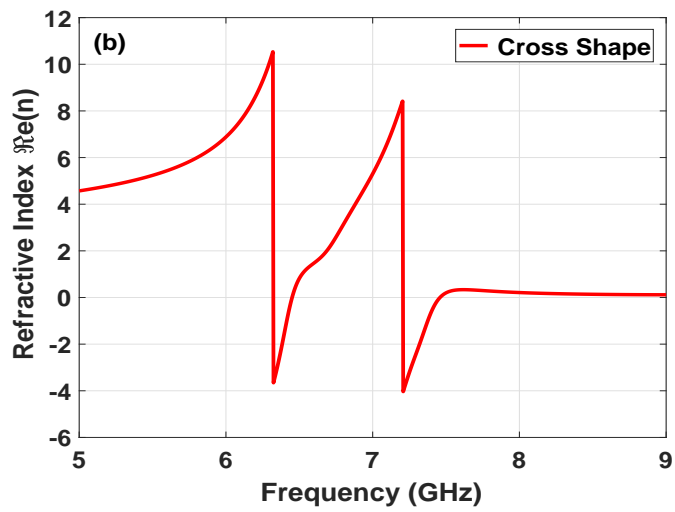
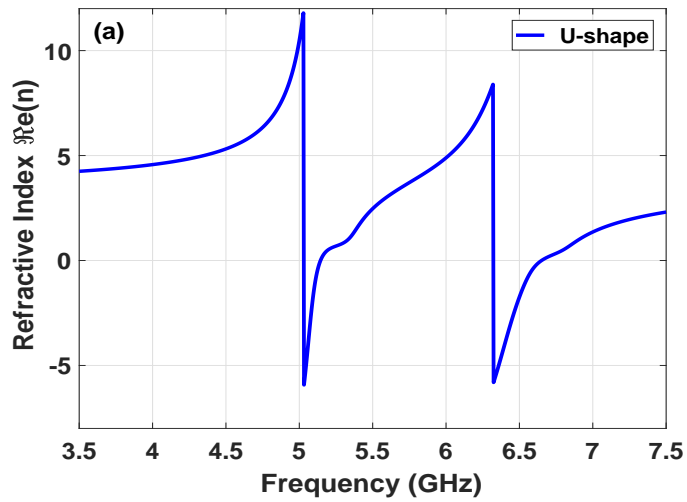


Figure 4.15 Simulated real value of refractive index $\Re(n)$ for the configuration of (a) U-shaped, (b) Cross-shaped and (c) Crescent-Shaped.

4.3.13 Permittivity (ϵ) of Chiral Medium

The responses of relative permittivity (ϵ) for three different configurations are demonstrated in the Fig. 4.16. The ϵ values for U-shaped and cross-shaped begin around the value of 20 and for crescent shape it is nearly 13. In addition, at the resonance regions permittivity values have negativity and permittivity values are decreasing towards end of the frequency range.

The permittivity of crescent-shaped has negative values at the both resonance regions which are seen in Fig. 4.16 (c); however, it has one negative refractive index in the Fig. 4.15 (c). This can be explained by the effect of impedance parameter as in the equation (2.43) ($\epsilon = n/Z$). Moreover, from the Fig. 4.16 (c) it is clearly noted that the response of proposed crescent-shaped resembles to U-shaped and cross-shaped responses. For that reason, crescent-shaped configuration is very useful for chiral structures and can lead to many potential applications.

4.3.14 Permeability (μ) of Chiral Medium

In this section the relative permeability of different chiral configurations are illustrated in Fig. 4.17. From the figures, one can get that all different configurations begins slightly over the value of unity and as expected at the resonance regions they are differ from each other . Furthermore, permeabilities have consistence when compared to other configurations.

Permeabilities are calculated from the equation (2.43) which is ($\mu = n \cdot Z$). In addition, negative permeabilities can be seen at some certain resonance regions. Next, when compared with the Fig. 4.16, it can be understand that the electrical property of those different chiral configurations are dominant than the magnetic property of that structures. Since, relative permittivity values are sufficiently high when compared with the relative permeability values.

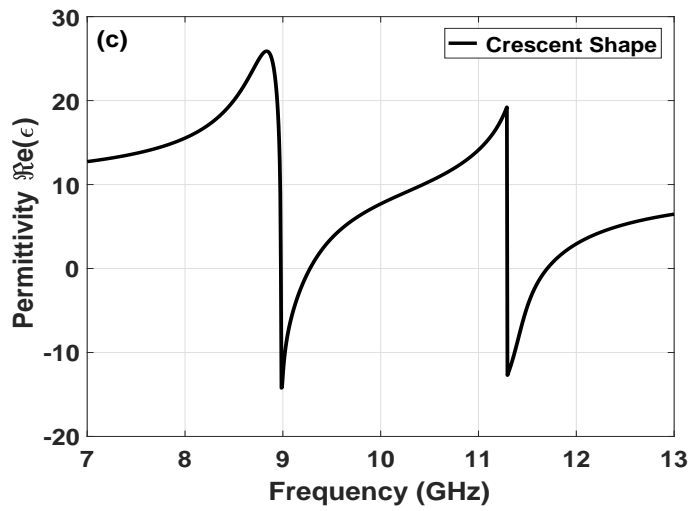
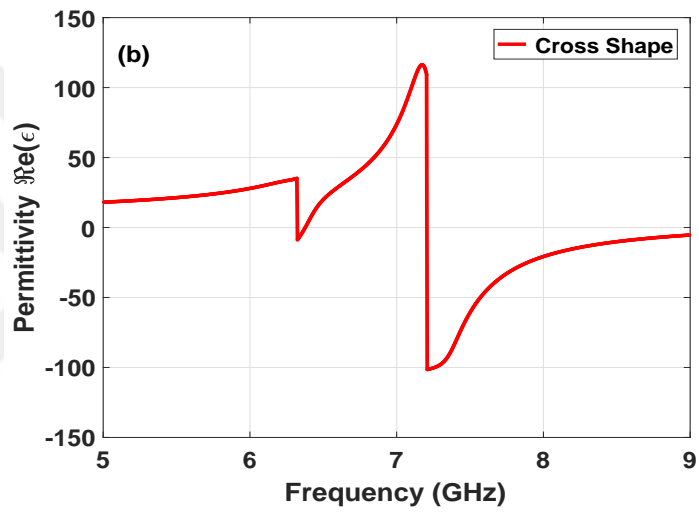
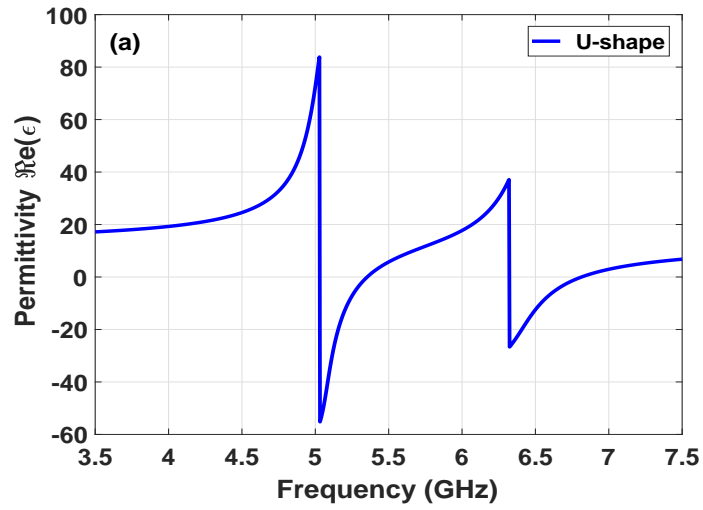


Figure 4.16 Simulated real value of relative permittivity $\Re(\epsilon)$ of chiral medium for the configuration of (a) U-shaped, (b) Cross-shaped and (c) Crescent-Shaped.

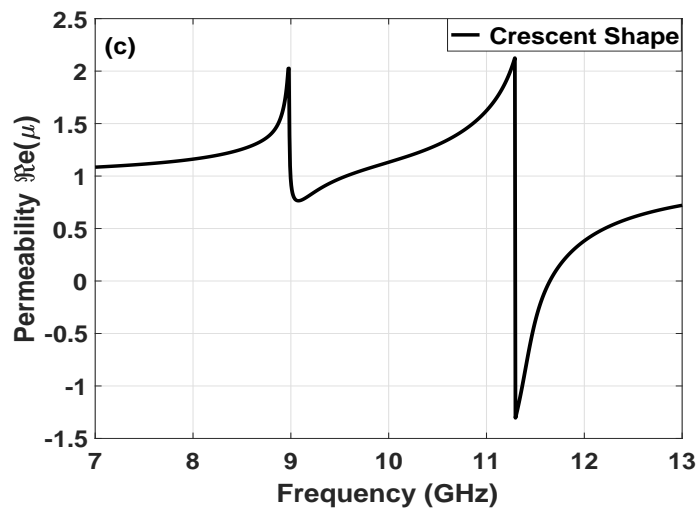
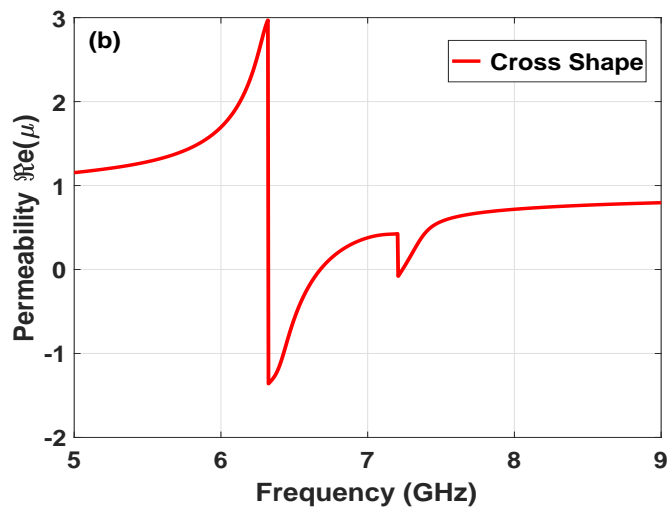
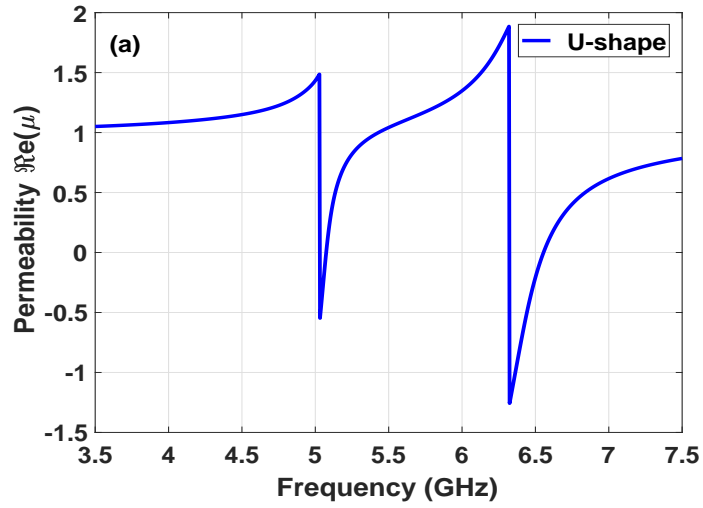


Figure 4.17 Simulated real value of relative permeability $\Re(\mu)$ of chiral medium for the configuration of (a) U-shaped, (b) Cross-shaped and (c) Crescent-Shaped.

CHAPTER 5

COUPLING EFFECT OF NEARBY RESONATING METAMATERIAL SLABS

5.1 Introduction

Until this chapter, as a former study we have investigated mainly on the near-field effects and characterization of chiral metamaterials (MMs) throughout this thesis. From now on, we will investigate coupling effect of resonating MM slabs that are adjacent to each other since, MM slabs that are close to each other may interact with one another and this interaction causes the strong coupling which consequently alter the characteristics of an individual MM cells.

In this chapter, the coupling phenomenon between MM slabs are examined by application of the signal flow graph technique (SFG). Toward this end, the scattering (S-) parameters of a whole combined MM structure composing of from individual MM slabs are utilized. The SFG technique gives us the chance to provide quantitative data about the level of coupling and relevant information about the presence of the coupling as different from other methods in literature. Using S-parameters for analysing the coupling effect of a MM slab composed of split-ring-resonators are investigated and their resonances are especially designed within X-band (8.2-12.4 GHz).

There are many retrieval methods available in the literature for determining the electromagnetic properties of MM slabs. These methods can be exemplified as measured/simulated scattering (S-) parameters [45, 66–69], averaging of field technique [63], the qualitative effective medium theory [46] and the homogenization method [70].

MM slabs are generally designed in the transverse dimensions with periodic arrangement of unit cells. Therefore, the importance of obtaining the physics and mechanisms of coupling effect among adjacent cells in the transverse direction rises especially for the some specific MM design applications [71, 72]. In addition, in some applications MM slabs are cascaded in the longitudinal direction to enhance their radiation patterns and providing extra degree of flexibility to adapt the response of MM slabs [71].

Therefore, coupling types can be classified into two groups as transverse coupling and longitudinal coupling [72]. In the literature, both of these coupling types are investigated through the studies [28–30, 71–79]. Although transverse and longitudinal couplings of MMs in the studies [72–74] are analyzed without any gap on resonating SRRs, in studies [29, 71] coupling between adjacent resonators is analysed by applying the gaps and splits on resonating SRRs at microwave frequencies.

It is noted that there are three different types of polarizations present in MM structures. These polarization types can be classified as electric excitation, magnetic excitation, and both of them together [72]. Similar to other resonating structures in the literature, in the resonance regions MMs absorb much of the energy, leading to minimum transmission properties [72]. Although individual resonating cells operate independently, they can also behave co-operatively based on coupling effect between these resonators. If separate MM resonators approach to each other, these resonators can couple with one another resulting in different total response when compared with response of each separate MM resonators.

In addition, coupling phenomenon between nearby resonating MMs are also examined at infrared and terahertz frequency regions through the studies [75, 78, 79]. Besides, the coupling effect of nearby MM resonators in the resonance frequency regions can be changed or tuned so the studies related to this concepts are analysed in detail through [28, 30, 76, 77].

However, to our best knowledge none of these studies analyses the coupling effect using the SGF technique in terms of scattering (S-) parameters. This analysis gives information about coupling effect of nearby MM resonators not only qualitatively but also quantitatively. For that reason, in this chapter our purpose is to investigate coupling phenomenon between nearby MM resonators from simulated S-parameters of individual and overall MM responses by applying the SGF technique.



5.2 Theory of Coupling Analysis

In this section, the SFG and the transfer matrix (TM) techniques [80] will be used to determine the quantitative and quality response of the coupling phenomenon between two slabs where these samples can be either conventional materials and/or MM resonators. In order to analyze overall response of composite structures composed of cascaded elements, the SFG technique is more useful for determining or examining the S-parameters of the sources, networks, and loads [80]. A composite structure composed of two slabs is demonstrated in Fig. 5.1(a).

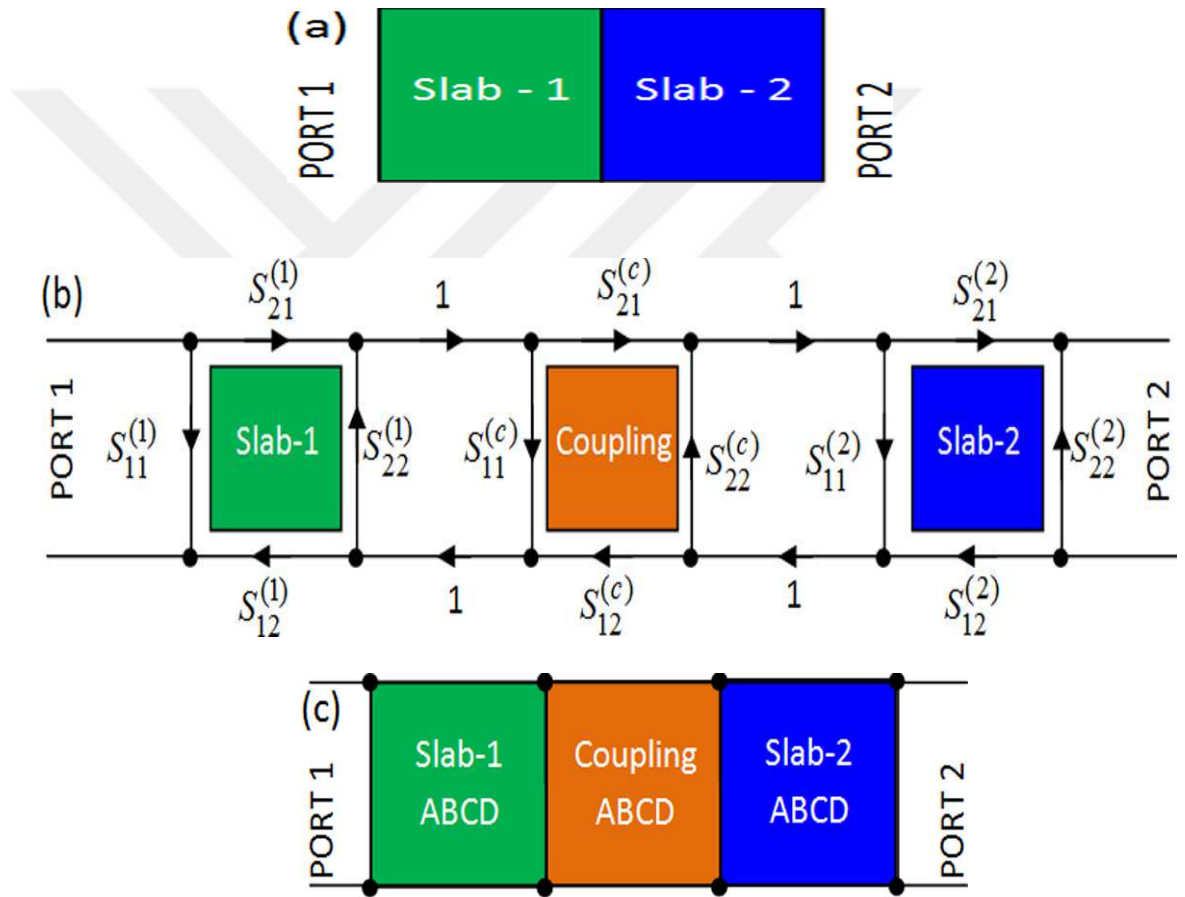


Figure 5.1 (a) A composite structure with two cascaded slabs, (b) its S-parameter equivalent, and (c) its ABCD parameter equivalent [81].

We can assume that the slabs in Fig. 5.1 are modelled as two-port circuits with their corresponding S-parameters. The overall response of this composite structure will be the individual response of each individual cascaded slab and the response of coupling between them. For considering the effect of coupling between two slabs in Fig. 5.1(a), the S-parameters representation of two-port networks is demonstrated in Fig. 5.1(b).

Here, the slabs are described by forward and backward reflection and transmission S-parameters (S_{11} , S_{21} , S_{12} , and S_{22}). The first and second slabs are specified by the superscript '1' and '2' in the parenthesis while $S_{11}^{(c)}$, $S_{21}^{(c)}$, $S_{12}^{(c)}$, and $S_{22}^{(c)}$ denote the coupling network parameters.

The three cascaded two-port networks in Fig. 5.1(b) are applied by the SFG technique and the overall response (forward and backward S-parameters) of the composite structure in Fig. 5.1(a) is obtained as [82].

$$S_{11}^{3T} = S_{11}^{2T} + \frac{S_{21}^{2T} S_{12}^{2T} S_{11}^{(2)}}{1 - S_{11}^{(2)} S_{22}^{2T}}, \quad S_{21}^{3T} = \frac{S_{21}^{(2T)} S_{21}^{(2)}}{1 - S_{11}^{(2)} S_{22}^{2T}}, \quad (5.1)$$

$$S_{22}^{3T} = S_{22}^{(2)} + \frac{S_{21}^{(2)} S_{12}^{(2)} S_{22}^{2T}}{1 - S_{11}^{(2)} S_{22}^{2T}}, \quad S_{12}^{3T} = \frac{S_{12}^{2T} S_{12}^{(2)}}{1 - S_{11}^{(2)} S_{22}^{2T}}, \quad (5.2)$$

where

$$S_{11}^{2T} = S_{11}^{(1)} + \frac{S_{21}^{(1)} S_{12}^{(1)} S_{11}^{(c)}}{1 - S_{11}^{(c)} S_{22}^{(1)}}, \quad S_{21}^{2T} = \frac{S_{21}^{(1)} S_{21}^{(c)}}{1 - S_{11}^{(c)} S_{22}^{(1)}}, \quad (5.3)$$

$$S_{22}^{2T} = S_{22}^{(c)} + \frac{S_{21}^{(c)} S_{12}^{(c)} S_{22}^{(1)}}{1 - S_{11}^{(c)} S_{22}^{(1)}}, \quad S_{12}^{2T} = \frac{S_{12}^{(1)} S_{12}^{(c)}}{1 - S_{11}^{(c)} S_{22}^{(1)}}. \quad (5.4)$$

Here, the overall response of the structure is denoted by the superscript '3T' and the response of two networks (Slab-1 and Coupling networks) at left side of the Fig. 5.1(b) corresponds to the superscript '2T'. From equation (5.1) - (5.4), we note that the overall response of the structure is affected by the coupling effect of two individual slabs shown in Fig. 5.1(a).

Using the SFG technique for determining the S-parameters of the coupling network from equation (5.1) - (5.4) requires meticulous labor force. For that reason, we get help from the TM technique (or ABCD parameters) in this study. Besides, the wave cascading matrix technique can also be an alternative way for the same purpose as mentioned in [83, 84].

The Fig. 5.1(c) is represented by the ABCD equivalent of the configuration in Fig. 5.1(b) and mathematically it can be written as

$$\begin{bmatrix} A_w & B_w \\ C_w & D_w \end{bmatrix} = \begin{bmatrix} A_1 & B_1 \\ C_1 & D_1 \end{bmatrix} \begin{bmatrix} A_c & B_c \\ C_c & D_c \end{bmatrix} \begin{bmatrix} A_2 & B_2 \\ C_2 & D_2 \end{bmatrix}, \quad (5.5)$$

where the subscripts 'w', '1', 'c', and '2' represent the overall response of the composite structure, the first two left elements, the coupling section and the last two right elements, respectively. Furthermore, by using S-parameters, ABCD parameters can be obtained easily through [85].

$$A = [(1 + S_{11})(1 - S_{22}) + S_{21}S_{12}]/2S_{21}, \quad (5.6)$$

$$B = [(1 + S_{11})(1 + S_{22}) - S_{21}S_{12}]/2S_{21}, \quad (5.7)$$

$$C = [(1 - S_{11})(1 - S_{22}) - S_{21}S_{12}]/2S_{21}, \quad (5.8)$$

$$D = [(1 - S_{11})(1 + S_{22}) + S_{21}S_{12}]/2S_{21}, \quad (5.9)$$

Via equation (5.5), the coupling section can be extracted in terms of the ABCD parameters

$$\begin{bmatrix} A_c & B_c \\ C_c & D_c \end{bmatrix} = \begin{bmatrix} A_1 & B_1 \\ C_1 & D_1 \end{bmatrix}^{-1} \begin{bmatrix} A_w & B_w \\ C_w & D_w \end{bmatrix} \begin{bmatrix} A_2 & B_2 \\ C_2 & D_2 \end{bmatrix}^{-1}. \quad (5.10)$$

Here, the operator $[\star]^{-1}$ corresponds to the inverse of the matrix $[\star]$. After determining the ABCD parameters of the coupling section from equation (5.10), S-parameters related to coupling section can be retrieved as

$$S_{11}^{(c)} = \frac{A_c + B_c - C_c - D_c}{A_c + B_c + C_c + D_c}, \quad (5.11)$$

$$S_{12}^{(c)} = \frac{2(A_c D_c - B_c C_c)}{A_c + B_c + C_c + D_c}, \quad (5.12)$$

$$S_{21}^{(c)} = \frac{2}{A_c + B_c + C_c + D_c}, \quad (5.13)$$

$$S_{22}^{(c)} = \frac{-A_c + B_c - C_c + D_c}{A_c + B_c + C_c + D_c}. \quad (5.14)$$

5.3 Computational Analysis of Coupling Analysis

In this section, ABCD and S-parameters of the coupling section will be presented by using two different types of slabs. In the first case, each sample is assumed to be a non-resonating material. However, in the second case, individual samples are assumed to be constructed by a resonating MM cell.

5.3.1 Geometrical and Electrical Properties of Slabs

The investigated conventional material for coupling analysis is the polyethylene sample. Its electric properties are dielectric constant $\varepsilon_r = 2.25$ and loss tangent $\delta_r = 0.0001$. The sample dimensions are arranged according to X-band waveguide (8.2 - 12.4 GHz) with length $L_d = 3.85$ mm, height 10.16 mm, and width 22.86 mm. On the other hand, geometrical parameters related to MM unit cell are demonstrated in Fig. 5.2(a). Its dimensions are length $u_z = 2.54$ mm and height $u_y = 2.54$ mm. Furthermore, thickness of the FR4 material is assumed to be $d = 1.615$ mm with a dielectric constant $\varepsilon_s = 4.3$, and a loss tangent $\delta_s = 0.025$ (or $\delta_s = 0.005$). In addition, metallization dimension of the SRR pattern is $L_m = 2.00$ mm, width $w = 0.30$ mm, and gap $g = 0.30$ mm with copper conductivity $\sigma = 5.8 \times 10^7$ S/m and copper thickness $t_m = 35$ μm .

Fig. 5.2(b) represents the construction of individual MM slabs composed of small MM unit cells by the sequence of 4×7 times of first unit cells. In the y direction, there are 4 unit cells ($b = 4u_y$) with a repetition ($a = 7u_x$) in the longitudinal (x) direction so that cross section of the X-band waveguide almost filled by overall MM unit cells. Furthermore, in the y direction the unit cells are reversed in order to coincidence the gaps of neighbour unit cells with each other. In the remainder of this chapter, this MM slab is called as 4×7 MM slab.

When we examine the MM slab in Fig. 5.2(b) (4×7), it has a periodicity 3.266 mm ($= u_x$) and 2.54 mm ($= u_y = u_z$) in the x and y directions. Both these periodicity dimensions are much less than the free-space wavelength of X-band (approximately 10 times) which corresponds to the mid-frequency of 10 GHz [86].

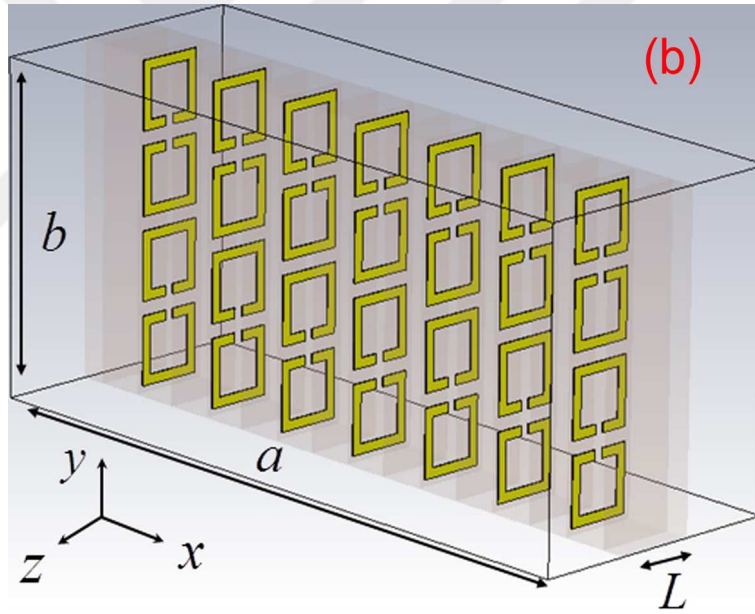
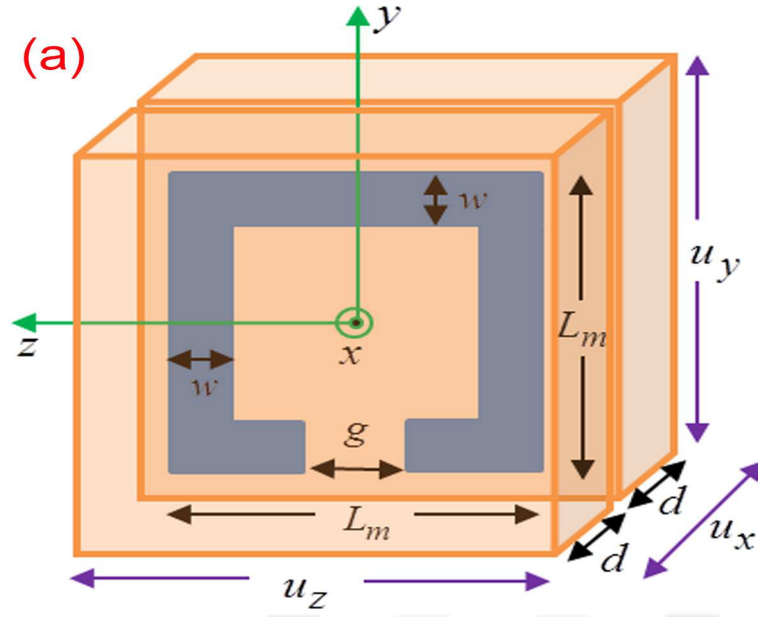


Figure 5.2 (a) Configuration of principal axis and geometry of a MM (split-ring-resonator–SRR) unit cell and field directions and propagation vector \vec{k} . $L_m = 2.00$ mm, $w = g = 0.30$ mm, $u_y = u_z = 2.54$ mm, $u_x = 2d + t_m$, $t_m = 35\mu\text{m}$ (metallization thickness), and $d = 1.615$ mm (substrate thickness) and (b) a MM slab composed of 4×7 unit cells within the cross section of X-band waveguide ($a = 22.86$ mm and $b = 10.16$ mm) [81].

5.3.2 Simulation Details

For analysis of coupling phenomenon, propagation through a metallic waveguide was considered at X-band (8.2 - 12.4 GHz). Simulations were performed by finite integration technique program of CST Microwave Studio©–2015. In simulations, boundary conditions were assumed to be perfect electric conductor ($E_t = 0$ – electric wall conditions) to construct a metallic waveguide structure over the yz surfaces at $x = \mp a/2$ and the xz surfaces at $y = \mp b/2$ Fig. 5.2(b). Furthermore, an imaging effect in the transverse plan (xy plane) are produced by the boundary conditions.

To retrieve the response of the MMs for coupling analysis, electromagnetic energy is transmitted from waveguide ports which are located at 10 mm away from the surface of the MM slab over xy planes. In addition, while we were performing the simulations on CST program, adaptive meshing features were utilized to arrange the optimum number of meshing size.

5.3.3 Simulation Results

To demonstrate coupling analysis between two slabs explicitly, firstly the conventional polyethylene sample mentioned in Subsection 5.3.1 was considered. In this case, the first polyethylene slab (which is at left side in Fig. 5.1(b)) with length L_d was simulated and its corresponding S-parameters are denoted by $S_{11}^{(1)}$, $S_{21}^{(1)}$, $S_{12}^{(1)}$, and $S_{22}^{(1)}$. Besides, for the second polyethylene slab, it is selected identical to the first sample with length L_d and its S-parameters are denoted by $S_{11}^{(2)}$, $S_{21}^{(2)}$, $S_{12}^{(2)}$, and $S_{22}^{(2)}$. Then, the cascaded polyethylene slabs with overall length $2L_d$ were simulated and its S-parameters correspond to S_{11}^{3T} , S_{21}^{3T} , S_{12}^{3T} , and S_{22}^{3T} . In the end, after obtaining necessary S-parameters to investigate coupling analysis, our algorithm was applied.

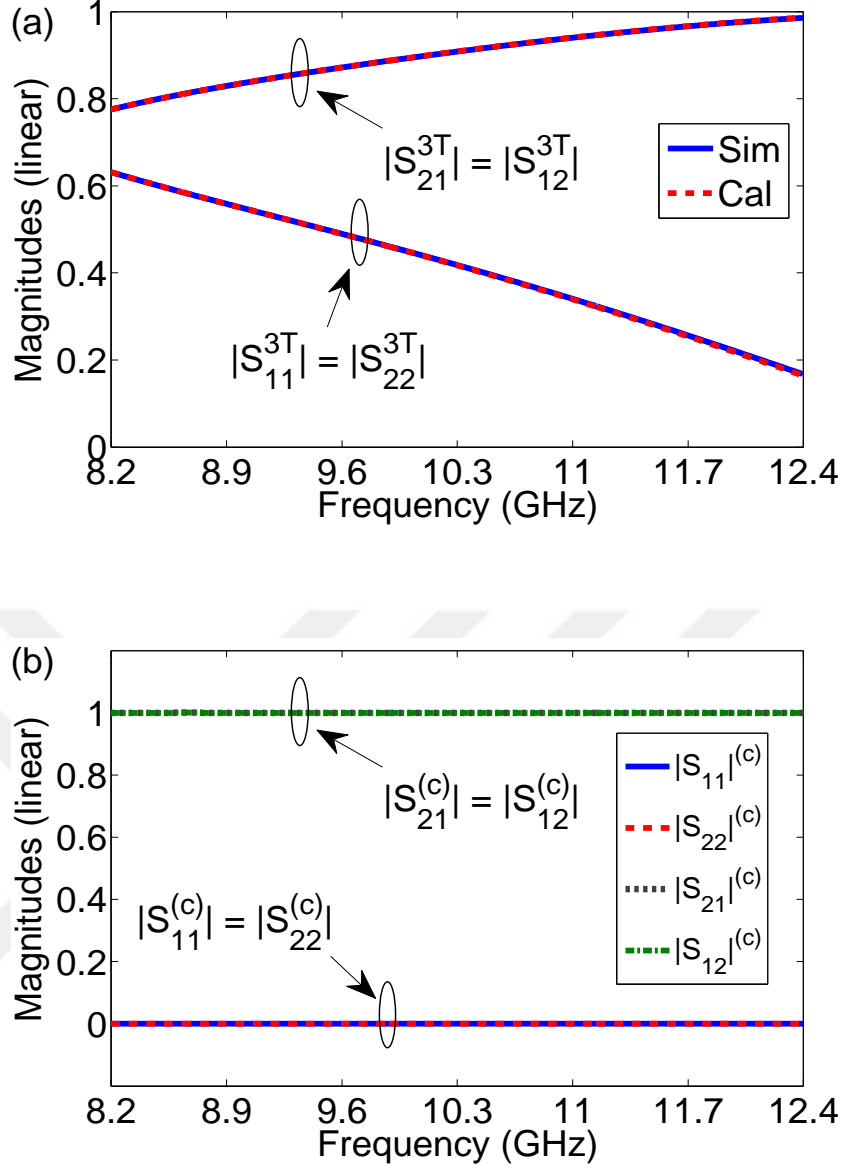


Figure 5.3 (a) Simulated (Sim) and calculated (Cal) $|S_{11}^{3T}|$, $|S_{21}^{3T}|$, $|S_{12}^{3T}|$, and $|S_{22}^{3T}|$ and (b) extracted $|S_{11}^{(c)}|$, $|S_{21}^{(c)}|$, $|S_{12}^{(c)}|$, and $|S_{22}^{(c)}|$ for cascaded two polyethylene slabs with overall length $2L_d$. Solid blue and dashed red curves show simulated and calculated dependencies, respectively. In calculation, we used $S_{11}^{(c)} = S_{22}^{(c)} = 0$ and $S_{21}^{(c)} = S_{12}^{(c)} = 1$ [81].

Toward this end, with the aid of equations (5.1) - (5.4), S_{11}^{3T} , S_{21}^{3T} , S_{12}^{3T} , and S_{22}^{3T} were calculated by using simulated S-parameters $S_{11}^{(1)}$, $S_{21}^{(1)}$, $S_{12}^{(1)}$, $S_{22}^{(1)}$, $S_{11}^{(2)}$, $S_{21}^{(2)}$, $S_{12}^{(2)}$, and $S_{22}^{(2)}$ for the condition $S_{11}^{(c)} = S_{22}^{(c)} = 0$ and $S_{21}^{(c)} = S_{12}^{(c)} = 1$. The parameters $S_{11}^{(c)}$, $S_{21}^{(c)}$, $S_{12}^{(c)}$, and $S_{22}^{(c)}$ will show us the difference between the how simulated and calculated parameters (S_{11}^{3T} , S_{21}^{3T} , S_{12}^{3T} , and S_{22}^{3T}) differ from each other.

Then, by using the simulated parameters S_{11}^{3T} , S_{21}^{3T} , S_{12}^{3T} , S_{22}^{3T} and with the aid of equation (5.6)-(5.9), the parameters related to whole cascaded polyethylene slabs A_w , B_w , C_w , and D_w were determined. Next, by using a similar approach from simulated $S_{11}^{(1)}$, $S_{21}^{(1)}$, $S_{12}^{(1)}$, and $S_{22}^{(1)}$, the ABCD parameters of the first and second polyethylene slabs were calculated after computing $S_{11}^{(c)}$, $S_{22}^{(c)}$, $S_{21}^{(c)}$, and $S_{12}^{(c)}$ from equation (5.11)-(5.14).

Dependencies of the simulated cascaded polyethylene slabs (each with has a length L_d) $|S_{11}^{3T}|$, $|S_{21}^{3T}|$, $|S_{12}^{3T}|$, and $|S_{22}^{3T}|$ are illustrated in Fig. 5.3(a) and their calculated values under the condition $S_{11}^{(c)} = S_{22}^{(c)} = 0$ and $S_{21}^{(c)} = S_{12}^{(c)} = 1$. By using the equation (5.10), the coupling responses $|S_{11}^{(c)}|$, $|S_{21}^{(c)}|$, $|S_{12}^{(c)}|$, and $|S_{22}^{(c)}|$ for cascade connection were extracted and are demonstrated in Fig. 5.3(b). Here, the magnitude sign of the corresponding S-parameter is denoted by vertical bars.

From Figs. 5.3(a) and 5.3(b), the following points can be considered. First, the polyethylene sample is a reflection-symmetric and transmission-symmetric material because $|S_{11}^{3T}| = |S_{22}^{3T}|$ and $|S_{21}^{3T}| = |S_{12}^{3T}|$ over the whole band. Second, polyethylene sample is a passive material with non-resonating property so that the coupling phenomenon can not be mentioned between cascaded polyethylene slabs. Third, it can be noted that $S_{11}^{(c)} = S_{22}^{(c)} = 0$ and $S_{21}^{(c)} = S_{12}^{(c)} = 1$ due to no-coupling between cascaded slabs [87].

After completing the analysis of coupling effects of conventional materials, results in Figs. 5.3(a) and 5.3(b) validate our proposed formalism. Next, the coupling phenomenon between two MM resonator slabs will be considered. The simulated S-parameters of the 4×7 MM slab with length 2.54 mm are demonstrated in Fig. 5.4 according to different substrate losses. The following results can be noted from the dependencies in Fig. 5.4.

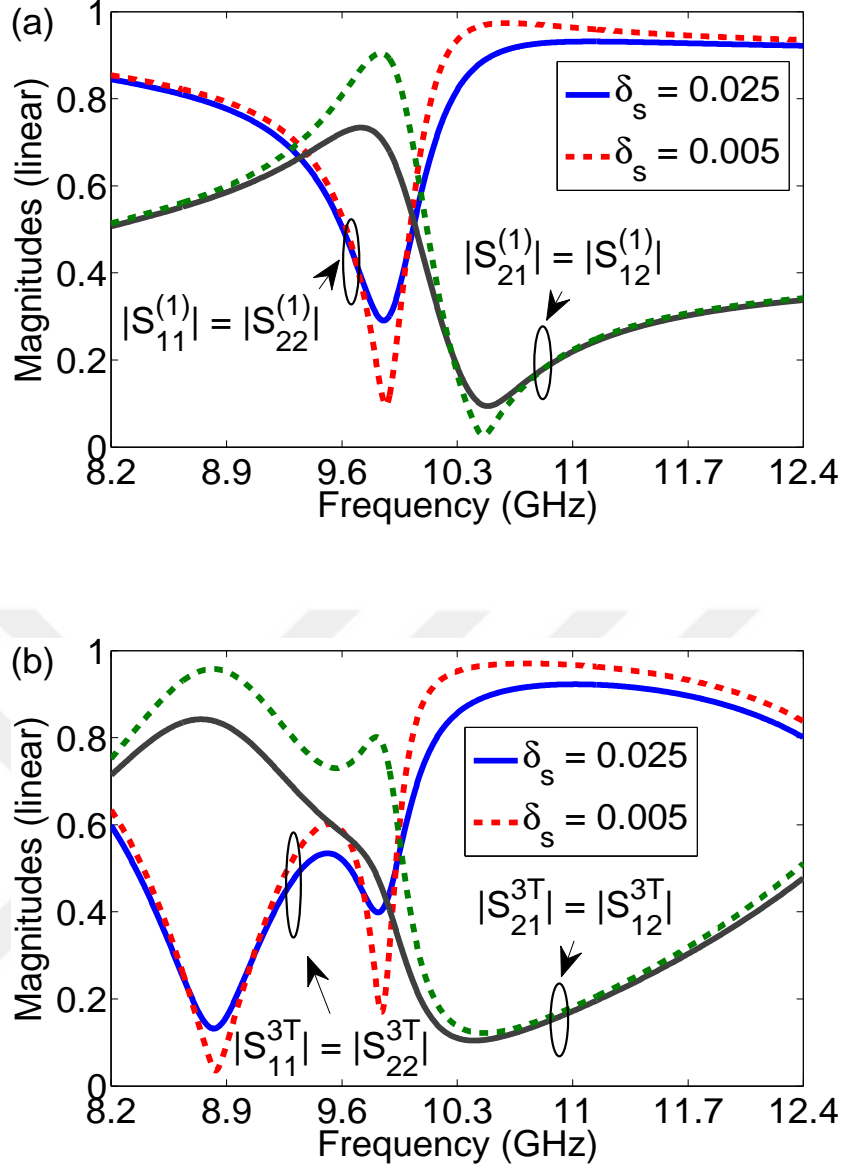


Figure 5.4 Simulated (a) $|S_{11}^{(1)}|$, $|S_{21}^{(1)}|$, $|S_{12}^{(1)}|$, and $|S_{22}^{(1)}|$ and (b) $|S_{11}^{3T}|$, $|S_{21}^{3T}|$, $|S_{12}^{3T}|$, and $|S_{22}^{3T}|$ of the 4×7 MM slab with different substrate losses. Solid and dashed curves denote S-parameters for $\delta_s = 0.025$ and $\delta_s = 0.005$, respectively [81].

First, it is noted from Fig. 5.4(a) (for the 4×7 MM slab ($\delta_s = 0.005$)) that there is a resonance frequency at 10.46 GHz for the local minimum value of transmission S-parameter. Second, due to coupling in propagation direction (z direction) [72, 71, 85] (as noted from Fig. 5.4(b)), resonance frequencies for cascade connection slabs (4×7 MM slabs) can be divided into two resonance frequency points of 9.565 GHz and 10.464 GHz. Third, eliminating the appearance of the extra resonance frequency points and producing a wider resonance region can be achieved by increasing the level of substrate loss.

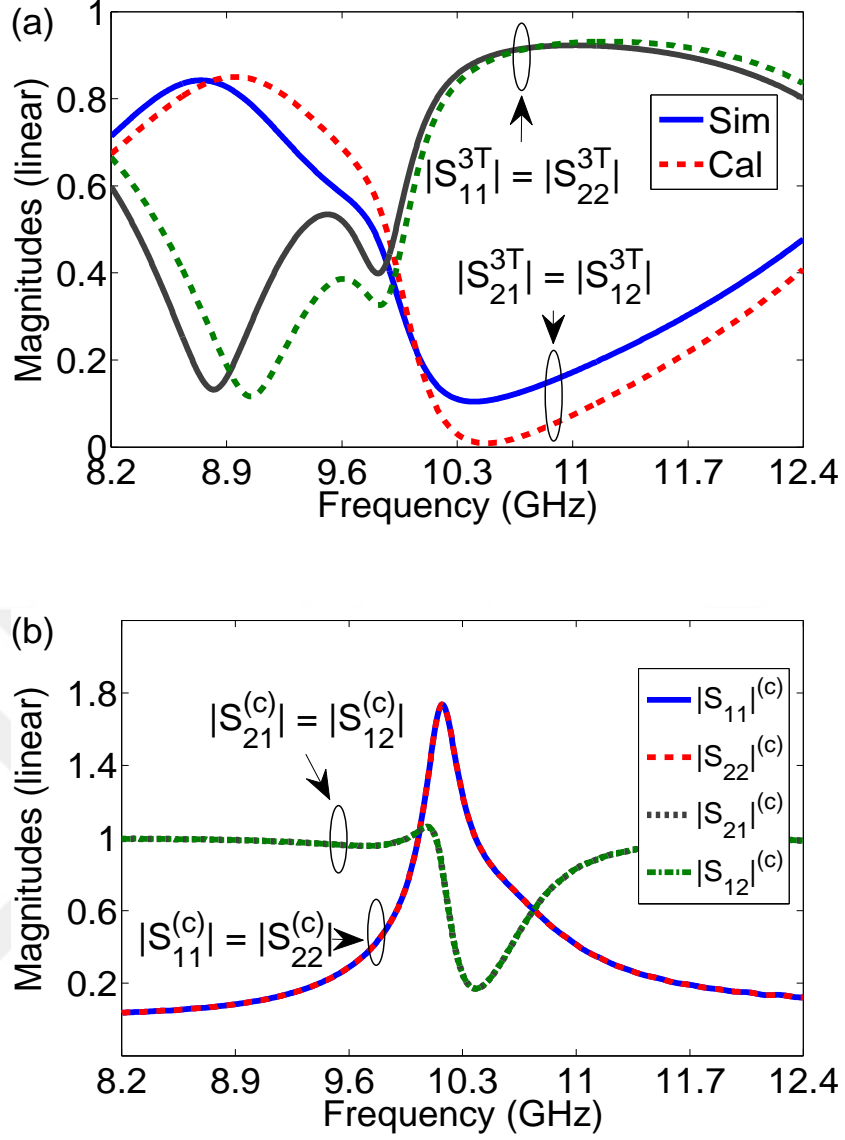


Figure 5.5 (a) Simulated (Sim) and calculated (Cal) $|S_{11}^{3T}|$, $|S_{21}^{3T}|$, $|S_{12}^{3T}|$, and $|S_{22}^{3T}|$ for cascaded two 4×7 MM slabs ($\delta_s = 0.025$) [In the calculation, we used $S_{11}^{(c)} = S_{22}^{(c)} = 0$ and $S_{21}^{(c)} = S_{12}^{(c)} = 1$], and (b) extracted $|S_{11}^{(c)}|$, $|S_{21}^{(c)}|$, $|S_{12}^{(c)}|$, and $|S_{22}^{(c)}|$ for cascaded two 4×7 MM slabs ($\delta_s = 0.025$) [81].

For coupling analysis of cascade connection of the 4×7 MM slab, the S-parameters $|S_{11}^{3T}|$, $|S_{21}^{3T}|$, $|S_{12}^{3T}|$, and $|S_{22}^{3T}|$ were calculated. For example, the S-parameters $|S_{11}^{3T}|$, $|S_{21}^{3T}|$, $|S_{12}^{3T}|$, and $|S_{22}^{3T}|$ for two cascaded 4×7 MM slabs with $\delta_s = 0.025$ were simulated and calculated as shown in Fig. 5.5(a). In our calculation analysis, we fixed $S_{11}^{(c)} = S_{22}^{(c)} = 0$ and $S_{21}^{(c)} = S_{12}^{(c)} = 1$. As seen from Fig. 5.5(a) that especially around the resonance regions ($\cong 10.3$ GHz), simulated and calculated $|S_{11}^{3T}|$, $|S_{21}^{3T}|$, $|S_{12}^{3T}|$, and $|S_{22}^{3T}|$ parameters differ from each other. This indicates coupling mechanism of between cascaded MM slabs.

In addition, coupling levels for the cascaded 4×7 MM slabs are evaluated by extracting $|S_{11}^{(c)}|$, $|S_{21}^{(c)}|$, $|S_{12}^{(c)}|$, and $|S_{22}^{(c)}|$ and the results are demonstrated in Fig. 5.5(b). Moreover, we note from Fig. 5.5(b) that extracted coupling transmissions $|S_{21}^{(c)}|$ and $|S_{12}^{(c)}|$ exceed one around the resonance regions while, around these regions the coupling reflections $|S_{11}^{(c)}|$ and $|S_{22}^{(c)}|$ increase considerably, indicating energy transfer between cascaded MM slabs in the propagation direction [80].

In order to clarify the investigation of coupling effects between MM slabs in the propagation direction, the magnitude of magnetic field intensity for the cascaded 4×7 MM slabs ($\delta_s = 0.025$) at 10.485 GHz was obtained and illustrated in Fig. 5.6(a). It is noted from those figures that for one period of two pairs of unit cells in propagation (z) direction and two cells in the y direction for each cascade connection of MM slabs are explicitly simulated and calculated.

Here, the maximum and minimum values are denoted by red and blue colors, respectively. Furthermore, as seen from Fig. 5.6(a) that only one of the pairs is active whereas the other one is inactive [71]. It can be considered that the first pair of the 4×7 MM slab is excited while its second pair remains inactive. The study [71] discusses the excitation selection in detail and the direction of the excitation for both pairs to be in either symmetric or antisymmetric ways which cause the different amplitude and phase responses.

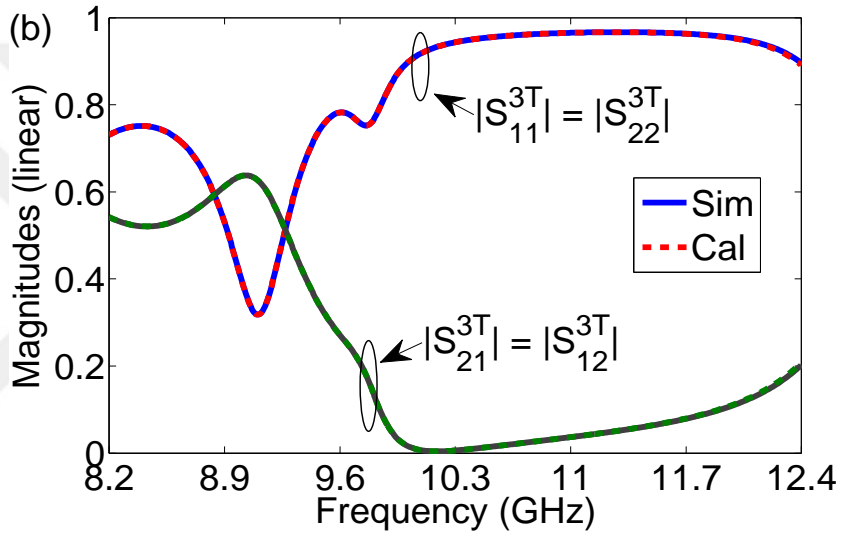
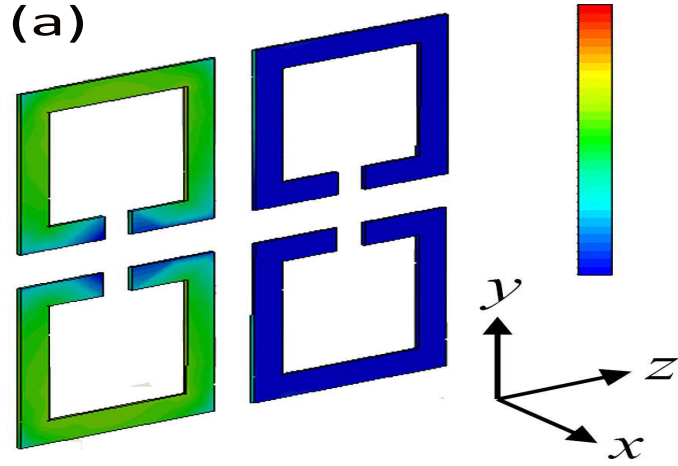


Figure 5.6 (a) Magnitude of magnetic field intensity over the SSRs for a cascade connection of two 4×7 MM slabs [Here, the dependencies are recorded when the highest field value is observed at resonance frequency 10.485 GHz. Red and blue colors on the color bar denote maximum (0 dB A/m) and minimum values (-40 dB A/m)], and (b) simulated (Sim) and calculated (Cal) $|S_{11}^{3T}|$, $|S_{21}^{3T}|$, $|S_{12}^{3T}|$, and $|S_{22}^{3T}|$ for (a) cascaded two 4×7 MM slabs ($\delta_s = 0.025$) when the slabs are separated by a 12 mm distance (filled by a FR4 sample) [Solid and dashed curves show simulated and calculated dependencies, respectively. In the calculation, we used $S_{11}^{(c)} = S_{22}^{(c)} = 0$ and $S_{21}^{(c)} = S_{12}^{(c)} = 1$] [81].

To improve the coupling phenomenon further, the distance between cascade connection of MM slabs was varied in various steps and our approach was applied. For example, for the MM slabs separated by a 12 mm distance between two 4×7 MM slabs ($\delta_s = 0.025$), simulated and calculated $|S_{11}^{3T}|$, $|S_{21}^{3T}|$, $|S_{12}^{3T}|$, and $|S_{22}^{3T}|$ are demonstrated in Fig. 5.6(b). In addition, the empty spaces inside the cross section of the X-band waveguide; that is, between the MM slabs is filled by a

FR4 sample. Furthermore, the relations $S_{11}^{(c)} = S_{22}^{(c)} = 0$ and $S_{21}^{(c)} = S_{12}^{(c)} = 1$ are assumed in the calculations. Besides, simulated and calculated $|S_{11}^{3T}|$, $|S_{21}^{3T}|$, $|S_{12}^{3T}|$, and $|S_{22}^{3T}|$ for adjacent two 4×7 MM slabs are nearly identical as seen from Fig. 5.6(b), this means that separating the slabs from each other considerably decreases coupling between the MM slabs.

To investigate coupling mechanism further, the S-parameters ($|S_{11}^{(c)}|$, $|S_{21}^{(c)}|$, $|S_{12}^{(c)}|$, and $|S_{22}^{(c)}|$) were extracted for cascaded two 4×7 MM slabs ($\delta_s = 0.025$) as illustrated in Fig. 5.7(a). We noted from the Fig. 5.7(a) that extracted transmissions $|S_{21}^{(c)}|$ (and $|S_{12}^{(c)}|$) are nearly one while reflections $|S_{11}^{(c)}|$ (and $|S_{22}^{(c)}|$) are zero over the whole range, indicating the coupling effect between nearby MM slabs is so weak (or negligible) in the propagation direction.

On the other hand, for the second case the MM slabs (for two 4×7 MM slabs ($\delta_s = 0.025$)) were separated by a 4 mm from each other and the dependencies of $|S_{11}^{(c)}|$, $|S_{21}^{(c)}|$, $|S_{12}^{(c)}|$, and $|S_{22}^{(c)}|$ are exhibited in Fig.5.7(b). It is noted from Fig. 5.7(b) that extracted $|S_{21}^{(c)}|$ (or $|S_{12}^{(c)}|$) values are slightly over one around the resonance region, indicating the existence of coupling phenomenon between MM slabs in propagation direction. From the dependencies in Figs. 5.5(b) and 5.7(b), we note that the level of coupling for separated MM slabs far away from each other is lower than the level of coupling between adjacent MM slabs with no separation.

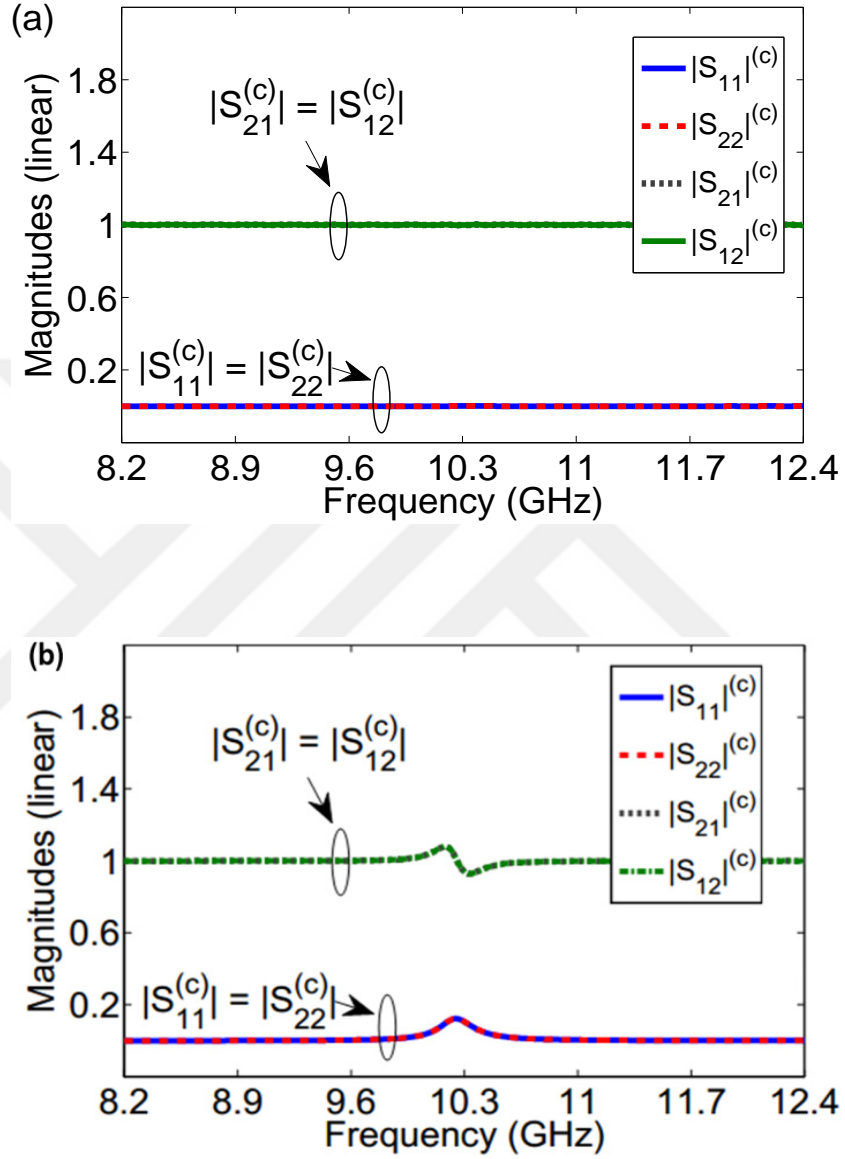


Figure 5.7 Extracted $|S_{11}^{(c)}|$, $|S_{21}^{(c)}|$, $|S_{12}^{(c)}|$, and $|S_{22}^{(c)}|$ for cascaded two 4×7 MM slabs ($\delta_s = 0.025$) when the slabs are separated by (a) a 12 mm distance (filled by a FR4 sample) and (b) a 4 mm distance (filled by a FR4 sample) [81].

CHAPTER 6

CONCLUSIONS AND FUTURE STUDIES

6.1 Conclusions

In this thesis, derivations, analyses, simulations, and a novel design of chiral MMs have been investigated. On the other hand, coupling effects of adjacent MM slabs has been investigated as one chapter. Briefly, two subjects have been proposed throughout this thesis for accurate retrieval of electromagnetic properties of MMs. These subjects can be classified as presenting a robust and accurate retrieval method for extraction of electromagnetic properties of chiral MM slabs taking into account of near-field effects, and the other subject is investigation of coupling phenomenon between nearby and distant MM slabs by considering substrate loss effect. Outcomes for each investigated subjects are presented in the following two subsections. Now, we will mention summary of the each chapters separately.

In the first chapter, the basic information about MMs are concerned especially for chiral MMs. In addition, historical backgrounds on MMs, definition of negative index MMs, literature review for chiral MMs, some terminologies and thesis motivation were presented.

In the second chapter, characterization and realization of chiral MMs has been discussed. Furthermore, starting from Maxwell's Equations all necessary equations were examined for the analysis of electromagnetic properties of chiral MMs. In addition, classification of bi-isotropic media was described and the concept of chirality properties was clarified in detail.

In the third chapter, analysis of near-field effects for chiral MM slabs has been considered. Previously, near-field effects for determining the electromagnetic properties of isotropic and bi-anisotropic MMs were examined in the literature. However, to our best knowledge, a retrieval method for chiral MMs by taking into account the near-field effects has not been incorporated until now. Therefore, the importance of near-field effects for retrieval methods especially for chiral MMs was discussed in detail throughout this chapter.

In the fourth chapter, a new type of crescent-shaped chiral MM configuration has been proposed and its optical activity and chirality properties are examined. In order to compare the properties of crescent-shaped chiral MM structure, different chiral configurations in the literature such as U-shaped and cross-shaped configurations have been utilized.

In the fifth chapter, the analysis of coupling of closely-located MM slabs was performed to examine the effect of this coupling on the overall response of stacked MM slabs in the propagation direction.

Toward this end, the coupling phenomenon between nearby resonating MM slabs was examined by applying the signal flow graph (SFG) technique.

In order to validate the appropriateness and usefulness of the SFG technique, we first considered an isotropic ordinary dielectric material (polyethylene sample). After validation, we next examined the effect of distance between resonating MM slabs and the effect of loss inside substrate materials in detail on the strength of coupling between MM slabs (C-shaped split ring resonator). Simulations were performed by CST-Microwave Studio at X-band (8.12-12.4 GHz).

6.1.1 Comments on Analysis of Near Field Effects for Chiral Metamaterials

A robust and accurate retrieval method for extraction of electromagnetic properties of chiral MM slabs taking into account of near-field effects was presented. The ray-tracing method was also applied in order to incorporate the near-field effects into scattering (S-) parameters of the MM slab. The method uses S-parameters of two identical chiral MM slabs with different lengths (different cell numbers) and determines the semi-infinite reflection coefficients from air to MM slab and from the MM slab to air.

By using S-parameters (simulated by CST Microwave Studio), we first validated our method for a Teflon sample then retrieved semi-infinite reflection coefficients of a chiral MM slab composed of U-shaped split-ring-resonators. From the retrieval analysis, we note that these reflection coefficients are different and independent of each other especially around resonance regions of the analyzed MM slab and demonstrating the importance of near-field effect in the extraction of electromagnetic properties of chiral MM slabs.

6.1.2 Comments on Analysis of Coupling Effect of Nearby Resonating Metamaterial Slabs

In this study, the coupling between nearby and distant MM slabs was investigated. To achieve our investigation, the SFG technique and transfer matrix method (ABCD parameters) were utilized. The analysis of coupling phenomenon in this study was separated into two parts. First, the calculated S-parameters and the simulated S-parameters of whole MM structure were compared in order to understand the coupling levels between resonating MM slabs. This was measured by the difference between simulated and calculated S-parameters. It is observed that as expected, there is no coupling effect between conventional slabs because difference between simulated and calculated S-parameters was almost zero.

Second, S-parameters of the coupling network (see Fig. 5.1(b)) between slabs by using ABCD parameters were extracted in order to be more suitable for cascaded networks. It is noted that coupling levels are decreasing when the distance of nearby MM slabs decreases. In addition, the effect of loss inside substrate materials and the distance between MM slabs were investigated in detail.

6.2 Future Studies

In the analyses of the near-field effects subject, the electric and magnetic surface susceptibilities at front and back surfaces of the chiral MM slab did not considered. As a future study, these surface susceptibilities can be calculated as was done for bi-anisotropic MMs in [44]. Additionally, the study of near-field effects can be extended to take into account the coupling analysis of chiral MMs. Toward this end, combining coupling analysis and near-field effects of chiral MMs can open a way to design and characterize exotic electromagnetic properties in the near future.





REFERENCES

- [1] Shelby, R. A., Smith, D. R., and Schultz, S. (2001). experimental verification of a negative index of refraction. *Science*, **292**, 77–79.
- [2] Veselago, V. G. (1968). The electrodynamics of substances with simultaneously negative values of ϵ and μ . *Phys. Usp.*, **10**, 509–514.
- [3] Pendry, J. B., Holden, A., Stewart, W., and Youngs, I. (1996). Extremely low frequency plasmons in metallic mesostructures. *Physical review letters*, **76**, 4773.
- [4] Pendry, J. B., Holden, A. J., Robbins, D. J., and Stewart, W. (1999). Magnetism from conductors and enhanced nonlinear phenomena. *IEEE transactions on microwave theory and techniques*, **47**, 2075–2084.
- [5] Smith, D. R., Padilla, W. J., Vier, D., Nemat-Nasser, S. C., and Schultz, S. (2000). Composite medium with simultaneously negative permeability and permittivity. *Physical review letters*, **84**, 4184.
- [6] Zheludev, N. I. (2010). The road ahead for metamaterials. *Science*, **328**, 582–583.
- [7] Zheludev, N. I. (2015). Obtaining optical properties on demand. *Science*, **348**, 973–974.
- [8] Ghodgaonkar, D. K., Varadan, V. V., and Varadan, V. K. (1990). Free-space measurement of complex permittivity and complex permeability of magnetic materials at microwave frequencies. *IEEE Transactions on Instrumentation and Measurement*, **39**, 387–394.
- [9] Chen, L. F., Ong, C. K., Neo, C. P., Varadan, V. V., and Varadan, V. K. (2004). *Microwave Electronics: Measurement and Materials Characterization*. Wiley.
- [10] Guoxin, C. (2015). Calibration-independent measurement of complex permittivity of liquids using a coaxial transmission line. *Rev. Sci. Instrum.*, **86**, 014704.
- [11] Caijun, Z., Quanxing, J., and Shenhui, J. (2011). Calibration-independent and position-insensitive transmission/reflection method for permittivity measurement with one sample in coaxial line. *IEEE Trans. Electromagn. Compat.*, **53**, 684–689.

- [12] Hasar, U. C., Muratoglu, A., Bute, M., Barroso, J. J., and Ertugrul, M. (2017). Effective Constitutive Parameters Retrieval Method for Bianisotropic Metamaterials Using Waveguide Measurements. *IEEE Trans. Microw. Theory Techn.*, **65**, 1488–1497.
- [13] Ogunlade, O., Pollard, R. D., and Hunter, I. C. (2006). A new method of obtaining the permittivity of liquids using in-waveguide technique. *IEEE Microw. Wireless Compon. Lett.*, **16**, 363–365.
- [14] Akhtar, M. J., Feher, L. E., and Thumm, M. (2006). A waveguide-based two-step approach for measuring complex permittivity tensor of uniaxial composite materials. *IEEE Trans. Microw. Theory Techn.*, **54**, 2011–2022.
- [15] Chen, H., Zhang, J., Bai, Y., Luo, Y., Ran, L., Jiang, Q., and Kong, J. A. (2006). Experimental retrieval of the effective parameters of metamaterials based on a waveguide method. *Opt. Express*, **14**, 12944–12949.
- [16] Engen, G. F. and Hoer, C. A. (1979). Thru-reflect-line: An improved technique for calibrating the dual 6-port automatic network analyzer. *IEEE Trans. Microw. Theory Techn.*, **27**, 983–987.
- [17] Hasar, U. C. and Inan, O. E. (2009). Elimination of the dependency of the calibration plane and the sample thickness from complex permittivity measurements of thin materials. *Microw. Opt. Technol. Lett.*, **51**.
- [18] Hasar, U. C. and Simsek, O. (2009). A calibration-independent microwave method for position-insensitive and nonsingular dielectric measurements of solid materials. *J. Phys. D: Appl. Phys.*, **42**.
- [19] Hasar, U. C. (2009). A self-checking technique for materials characterization using calibration-independent measurements of reflecting lines. *Microw. Opt. Technol. Lett.*, **51**, 129–132.
- [20] Hasar, U. C. (2008). A new calibration-independent method for complex permittivity extraction of solid dielectric materials. *IEEE Microw. Wireless Compon. Lett.*, **18**, 788–790.
- [21] Hasar, U. C. (2008). A calibration-independent method for accurate complex permittivity determination of liquid materials. *Rev. Sci. Instrum.*, **79**.
- [22] Hasar, U. C. (2008). Calibration-independent method for complex permittivity determination of liquid and granular materials. *Electron. Lett.*, **44**.
- [23] Jebbor, N., Bri, S., Sánchez, A. M., and Chaibi, M. (2013). A fast calibration-independent method for complex permittivity determination at microwave frequencies. *Measurement*, **46**, 2206–2209.
- [24] Schurig, D., Mock, J. J., Justice, B. J., Cummer, S. A., Pendry, J. B., Starr, A. F., and Smith, D. R. (2006). Metamaterial electromagnetic cloak at microwave frequencies. *Science*, **314**.
- [25] Chen, T., Li, S., and Sun, H. (2012). Metamaterials application in sensing. *Sensors*, **12**, 2742–2765.

- [26] Pendry, J. B. (2000). Negative refraction makes a perfect lens. *Phys. Rev. Lett.*, **85**.
- [27] Yoo, Y. J., Ju, S., Park, S. Y., Kim, Y. J., Bong, J., Lim, T., Kim, K. W., Rhee, J. Y., and Lee, Y. (2015). Metamaterial absorber for electromagnetic waves in periodic water droplets. *Scientific reports*, **5**, 14018.
- [28] Wang, J., Qu, S., Zhang, J., Ma, H., Yang, Y., Gu, C., Wu, X., and Xu, Z. (2009). A tunable left-handed metamaterial based on modified broadside-coupled split-ring resonators. *Prog. Electromagn. Res. Lett.*, **6**, 35–45.
- [29] Ekmekci, E., Topalli, K., Akin, T., and Turhan-Sayan, G. (2009). A tunable multi-band metamaterial design using micro-split srr structures. *Opt. Express*, **17**.
- [30] Ekmekci, E., Strikwerda, A. C., Fan, K., Keiser, G., Zhang, X., Turhan-Sayan, G., and Averitt, R. D. (2011). Frequency tunable terahertz metamaterials using broadside coupled split-ring resonators. *Phys. Rev. B*, **83**, 193103.
- [31] Navarro-Cia, M., Beruete, M., Falcone, F., Sorolla, M., and Campillo, I. (2010). Antenna directivity enhancement using a metamaterial parabolic lens. *Antennas and Propagation (EuCAP), 2010 Proceedings of the Fourth European Conference on*, pp. 1–3, IEEE.
- [32] Wang, Y., Sun, T., Paudel, T., Zhang, Y., Ren, Z., and Kempa, K. (2011). Metamaterial-plasmonic absorber structure for high efficiency amorphous silicon solar cells. *Nano letters*, **12**, 440–445.
- [33] Green, M. A. and Pillai, S. (2012). Harnessing plasmonics for solar cells. *Nature Photonics*, **6**, 130.
- [34] Dong, Z.-G., Lei, S.-Y., Li, Q., Xu, M.-X., Liu, H., Li, T., Wang, F.-M., and Zhu, S.-N. (2007). Non-left-handed transmission and bianisotropic effect in a π -shaped metallic metamaterial. *Phys. Rev. B*, **75**, 075117.
- [35] Li, Z., Mutlu, M., and Ozbay, E. (2013). Chiral metamaterials: from optical activity and negative refractive index to asymmetric transmission. *Journal of Optics*, **15**, 023001.
- [36] Zhao, R., Koschny, T., and Soukoulis, C. M. (2010). Chiral metamaterials: retrieval of the effective parameters with and without substrate. *Optics express*, **18**, 14553–14567.
- [37] Li, Z., Zhao, R., Koschny, T., Kafesaki, M., Alici, K. B., Colak, E., Caglayan, H., Ozbay, E., and Soukoulis, C. (2010). Chiral metamaterials with negative refractive index based on four “u” split ring resonators. *Applied Physics Letters*, **97**, 081901.
- [38] Zhou, J., Dong, J., Wang, B., Koschny, T., Kafesaki, M., and Soukoulis, C. M. (2009). Negative refractive index due to chirality. *Physical Review B*, **79**, 121104.

- [39] Tütüncü, B. and Torpi, H. (2017). Omega-shaped metamaterial lens design for microstrip patch antenna performance optimization at 12 ghz. *2017 10th International Conference on Electrical and Electronics Engineering (ELECO)*, Nov, pp. 987–990.
- [40] Chen, H., Ran, L., Huangfu, J., Zhang, X., Chen, K., Grzegorzcyk, T. M., and Kong, J. A. (2005). Negative refraction of a combined double s-shaped metamaterial. *Applied Physics Letters*, **86**, 151909.
- [41] Bute, M., Hasar, U. C., and Barroso, J. J. (2017). Retrieval parameters of chiral metamaterials with proposed crescent shaped split ring resonators. *2017 SBMO/IEEE MTT-S International Microwave and Optoelectronics Conference (IMOC)*, Aug, pp. 1–3.
- [42] Naskar, M. A., Tamrakar, M., and Thiripurasundari, D. (2017). Compact ‘v’ shaped metamaterial based resonator for wide band rejection. *2017 International Conference on Nextgen Electronic Technologies: Silicon to Software (ICNETS2)*, March, pp. 88–91.
- [43] Hasar, U. C., Barroso, J. J., Karacali, T., and Ertugrul, M. (2015). Semi-infinite reflection coefficients of bi-anisotropic metamaterial slabs including boundary effects. *IEEE Microwave and Wireless Components Letters*, **25**, 283–285.
- [44] Hasar, U. C., Barroso, J. J., Bute, M., Muratoglu, A., and Ertugrul, M. (2016). Boundary effects on the determination of electromagnetic properties of bianisotropic metamaterials from scattering parameters. *IEEE Transactions on Antennas and Propagation*, **64**, 3459–3469.
- [45] Chen, X., Wu, B.-I., Kong, J. A., and Grzegorzcyk, T. M. (2005). Retrieval of the effective constitutive parameters of bianisotropic metamaterials. *Phys. Rev. E*, **71**, 046610.
- [46] Marqués, R., Medina, F., and Rafia-El-Idrissi, R. (2002). Role of bianisotropy in negative permeability and left-handed metamaterials. *Phys. Rev. B*, **65**, 144440.
- [47] Delihacioglu, K. (1998). Power Reflection and Transmission Coefficients for a Chiral Slab and Meander Line Polarizer with Chiral Slab . *Gaziantep University.*, M.Sc. Thesis.
- [48] Uckun, S. (1998). Plane Wave Propagation Through a Uniaxial Chiral Slab and Transmission Coefficient. *Microwave Opt Technol Lett.* , **18**, 171–174.
- [49] Arago, D. F. (1881). Memoire sur une modification remarquable queprouvent les rayons lumineux dans leur passage a travers certains corps diaphanes et sur quelques autres nouveaux phenomenes d’optique. *Mem. Inst.*, **1**, 93–134.
- [50] Lindman, K. F. (1920). Uber eine durch ein isotropes System von spiralf ormigen Res- onatoren erzeugte Rotationspolarisation der elektromagnetischen Wellen. *Ann. Phys.*, **63**, 621–644.

- [51] Cory, H., and Rosenhouse, I. (1991). Electromagnetic Wave Propagation along a chiral Slab. *IEEE Proceedings Part H: microwave Antennas and Propagation.*, **39**, 676–677.
- [52] Margineda, J., Molina-Cuberos, G., Nunez, M., Garcia-Collado, A., and Martin, E. (2012). Electromagnetic characterization of chiral media. Kishk, A. (ed.), *Solutions and Applications of Scattering, Propagation, Radiation and Emission of Electromagnetic Waves*, chap. 1, IntechOpen.
- [53] Barba, I., Cabeceira, A., García-Collado, A., Molina-Cuberos, G., Margineda, J., and Represa, J. (2011). Quasi-planar chiral materials for microwave frequencies. *Electromagnetic Waves Propagation in Complex Matter*, InTech.
- [54] Sabah, C., Dincer, F., Karaaslan, M., Akgol, O., Demirel, E., and Unal, E. (2014). New-generation chiral metamaterials based on rectangular split ring resonators with small and constant chirality over a certain frequency band. *IEEE Trans. Antennas Propag.*, **62**, 5745–5751.
- [55] Wang, B., Zhou, J., Koschny, T., Kafesaki, M., and Soukoulis, C. M. (2009). Chiral metamaterials: simulations and experiments. *Journal of Optics A: Pure and Applied Optics*, **11**, 114003.
- [56] Ma, X., Pu, M., Li, X., Guo, Y., Gao, P., and Luo, X. (2017). Meta-chirality: Fundamentals, construction and applications. *Nanomaterials*, **7**, 116.
- [57] Kim, S., Kuester, E. F., Holloway, C. L., Scher, A. D., and Baker-Jarvis, J. (2011). Boundary effects on the determination of metamaterial parameters from normal incidence reflection and transmission measurements. *IEEE Transactions on Antennas and Propagation*, **59**, 2226–2240.
- [58] Kim, S., Kuester, E. F., Holloway, C. L., Scher, A. D., and Baker-Jarvis, J. R. (2012). Effective material property extraction of a metamaterial by taking boundary effects into account at te/tm polarized incidence. *Progress In Electromagnetics Research*, **36**, 1–33.
- [59] Hasar, U. C., Barroso, J. J., Buldu, G., Bute, M., Kaya, Y., Karacali, T., and Ertugrul, M. (2015). Reference-plane-invariant effective thickness and electromagnetic property determination of isotropic metamaterials involving boundary effects. *IEEE Journal of Selected Topics in Quantum Electronics*, **21**, 301–311.
- [60] Buriak, I., Zhurba, V., Vorobjov, G., Kulizhko, V., Kononov, O., and Rybalko, O. (2016). Metamaterials: Theory, classification and application strategies. *Journal of Nano-and Electronic Physics*, **8**, 4088–1.
- [61] Mayerhöfer, T. (2015). *www.researchgate.net*.
- [62] Grimberg, R. (2013). Electromagnetic metamaterials. *Materials Science and Engineering: B*, **178**, 1285 – 1295, selected Papers from the 9th International Conference on Physics of Advanced Materials (ICPAM9).

- [63] Pendry, J. B., Holden, A. J., Robbins, D. J., and Stewart, W. J. (1998). Low frequency plasmons in thin-wire structures. *Journal of Physics: Condensed Matter*, **10**, 4785–4809.
- [64] Hudlicka, M., Machac, J., and Nefedov, I. S. (2006). A triple wire medium as an isotropic negative permittivity metamaterial. *Progress In Electromagnetics Research*, **65**, 233–246.
- [65] Siddiqui, O. F., Mojahedi, M., and Eleftheriades, G. V. (2003). Periodically loaded transmission line with effective negative refractive index and negative group velocity. *IEEE Transactions on Antennas and Propagation*, **51**, 2619–2625.
- [66] Smith, D. R., Schultz, S., Markoš, P., and Soukoulis, C. M. (2002). Determination of effective permittivity and permeability of metamaterials from reflection and transmission coefficients. *Phys. Rev. B*, **65**, 195104.
- [67] Chen, X., Grzegorzczak, T. M., Wu, B.-I., Pacheco, J., and Kong, J. A. (2004). Robust method to retrieve the constitutive effective parameters of metamaterials. *Phys. Rev. E*, **70**, 016608.
- [68] Li, Z., Aydin, K., and Ozbay, E. (2009). Determination of the effective constitutive parameters of bianisotropic metamaterials from reflection and transmission coefficients. *Phys. Rev. E*, **79**, 026610.
- [69] Cohen, D. and Shavit, R. (2015). Bi-anisotropic metamaterials effective constitutive parameters extraction using oblique incidence s-parameters method. *IEEE Trans. Antennas Propag.*, **63**, 2071–2078.
- [70] Alù, A. (2011). First-principles homogenization theory for periodic metamaterials. *Phys. Rev. B*, **84**, 075153.
- [71] Penciu, R. S., Aydin, K., Kafesaki, M., Koschny, T., Ozbay, E., Economou, E. N., and Soukoulis, C. M. (2008). Multi-gap individual and coupled split-ring resonator structures. *Opt. Express*, **16**.
- [72] Gay-Balmaz, P. and Martin, O. J. F. (2002). Electromagnetic resonances in individual and coupled split-ring resonators. *J. Appl. Phys.*, **92**.
- [73] Katsarakis, N., Koschny, T., Kafesaki, M., Economou, E. N., , and Soukoulis, C. M. (2004). Electric coupling to the magnetic resonance of split ring resonators. *Appl. Phys. Lett.*, **84**.
- [74] García-García, J., Martín, F., Baena, J. D., Marqués, R., and Jelinek, L. (2005). On the resonances and polarizabilities of split ring resonators. *J. Appl. Phys.*, **98**.
- [75] Sersic, I., Frimmer, M., Verhagen, E., and Koenderink, A. F. (2009). Electric and magnetic dipole coupling in near-infrared split-ring metamaterial arrays. *Phys. Rev. Lett.*, **103**, 213902.
- [76] Lapine, M., Powell, D., Gorkunov, M., Shadrivov, I., Marqués, R., and Kivshar, Y. (2009). Structural tunability in metamaterials. *Appl. Phys. Lett.*, **95**.

- [77] Powell, D. A., Lapine, M., Gorkunov, M. V., Shadrivov, I. V., and Kivshar, Y. S. (2010). Metamaterial tuning by manipulation of near-field interaction. *Phys. Rev. B*, **82**, 155128.
- [78] Chowdhury, D. R., Singh, R., Taylor, A. J., and Chen, H. T. (2013). Ultrafast manipulation of near field coupling between bright and dark modes in terahertz metamaterial. *Appl. Phys. Lett.*, **102**.
- [79] Chowdhury, D. R., Azad, A. K., Zhang, W., and Singh, R. (2013). Near field coupling in passive and active terahertz metamaterial devices. *IEEE Trans. THz Sci. Technol.*, **3**.
- [80] Pozar, D. M. (2011). *Microwave Engineering*. Wiley.
- [81] Bute, M. and Hasar, U. C. (2016). Analyzing coupling effect of adjacent resonating metamaterial slabs. *2016 International Conference for Students on Applied Engineering (ICSAE)*, Oct, pp. 98–103.
- [82] Hasar, U. C. and Barroso, J. J. (2015). Scattering parameter analysis of cascaded bi-anisotropic metamaterials. *Optics Commun.*, **348**, 13–18.
- [83] Hasar, U. C. (2009). A new microwave method for electrical characterization of low-loss materials. *IEEE Microw. Wireless Compon. Lett.*, **19**, 801–803.
- [84] Hasar, U. C., Kaya, Y., Barroso, J. J., and Ertugrul, M. (2015). Determination of reference-plane invariant, thickness-independent, and broadband constitutive parameters of thin materials. *IEEE Trans. Microw. Theory Techn.*, **63**, 2313–2321.
- [85] Hasar, U. C., Bute, M., Barroso, J. J., Sabah, C., Kaya, Y., and Ertugrul, M. (2014). Power analysis of multilayer structures composed of conventional materials and bi-anisotropic metamaterial slabs. *J. Opt. Soc. Am. B*, **31**, 939–947.
- [86] Trang, F., Rogalla, H., and Popović, Z. (2015). Effective constitutive parameters of high-temperature superconducting split-ring resonator arrays. *IEEE Trans. Appl. Supercond.*, **25**, 1–7.
- [87] Hasar, U. C., Ozbek, I. Y., Cavusoglu, B., Karacali, T., Efeoglu, H., Ertugrul, M., and Barroso, J. J. (2015). Characterization of porous silicon fabry-perot optical sensors for reflectivity and transmittivity measurements. *IEEE Journal of Selected Topics in Quantum Electronics*, **21**, 174–183.



RESUME

1. General

Date of Arrangement	11/ 12 / 2018		
Title Name Surname :	Res. Ass. Musa BUTE		
Correspondence Address:	Gaziantep University, Department of Electrical and Electronics Engineering A-Block Z-01, 27310, Gaziantep, Turkey.		
Birth date and place:	15 / 06 / 1988, Adana / Turkey		
Phone:	+90 342 317 2115	GSM:	+90 555 701 7817
Email:	mbute@gantep.edu.tr	Fax:	+90 342 360 1103
Web:	http://www.gantep.edu.tr/akademik/index.php?ana=0&akadID=1000000330&bolum_id=102		

2. Education:

Education Period	Graduation	University	Department
2013 - 2018	Doctor of Philosophy- Ph.D.	Gaziantep University	Electromagnetic Fields and Microwave Techniques under Electrical and Electronics Engineering.
2011 - 2013	Master of Science - M. Sc.	Gaziantep University	Electromagnetic Fields and Microwave Techniques under Electrical and Electronics Engineering.
2006 - 2011	Bachelor - B. Sc.	Gaziantep University	Electrical and Electronics Engineering.

3. Dissertation

M.Sc. Thesis Title	Investigation of Propagation Characteristics of a Composite Material Composed of a Bianisotropic Metamaterial and an Isotropic Conventional Material
Supervisor	Prof. Dr. Uğur Cem Hasar http://www.gantep.edu.tr/en/akademik/index.php?ana=100&akadID=1000000492&bolum_id=102
Ph.D Dissert. Title	Investigation of Near Field Effects on Retrieval of Electromagnetic Properties of Chiral Metamaterials and Coupling Effects of Nearby Metamaterials
Supervisor	Prof. Dr. Uğur Cem Hasar http://www.gantep.edu.tr/en/akademik/index.php?ana=100&akadID=1000000492&bolum_id=102

4. Graduation Grade

Ph.D.	4.0	Master of Science	3.81 / 4
Language	Yökdil : 83,75	YDS : 80	

5. Journal Publications:

Authors	Title of Paper	Journal	Vol/no/page	Date
16) M.Bute and U. C. Hasar	Analysis of Near-Field Effects for Chiral Metamaterial Slabs	<i>IEEE Photonics Technology Letters</i>	Under Review	---
15) U. C. Hasar, G. Buldu, M. Bute and A. Muratoglu	Reference-plane-invariant waveguide method for electromagnetic characterization of bi-axial bi-anisotropic metamaterials	<i>Sensors and Actuators A: Physical</i>	Vol:283, p.141-150.	2018
14) U.C. Hasar and M. Bute	Electromagnetic Characterization of Thin Dielectric Materials from Amplitude-Only Measurements	<i>IEEE Sensors Journal</i>	Vol:17,no:16, 5093-5103	2017
13) U.C. Hasar and M. Bute	Error-Corrected Reflection and Transmission Scattering Parameters of a Two-Port Device	<i>IEEE Microwave Wireless Components Letters</i>	Vol:27, No:7, 681-683	2017
12) U.C. Hasar, A. Muratoglu, M. Bute, J.J. Barroso, and M. Ertugrul	Effective constitutive parameters retrieval method for bi-anisotropic metamaterials using waveguide measurements	<i>IEEE Transactions on Microwave Theory and Techniques</i>	Vol:65, no:5, 1488-1497	2017
11) U.C. Hasar and M. Bute	Reference-Invariant Permittivity and Thickness Measurement of Lossy Liquid Materials	<i>IET, Electronics Letters</i>	Vol:53, no:8, 544 - 546	2017
10) U. C. Hasar, Buldu, G, M. Bute and A. Muratoglu	Calibration-free extraction of constitutive parameters of magnetically coupled anisotropic metamaterials using waveguide measurements	<i>AIP, Review of Scientific Instruments</i>	Vol:88,No:10 104702	2017
9) U. C. Hasar, J. J. Barroso, M. Bute, A. Muratoglu, and M. Ertugrul	Boundary effects on the determination of electromagnetic properties of bi-anisotropic metamaterials from scattering parameters	<i>IEEE Transactions on Antennas and Propagation</i>	Vol:64, no:8, 3459-3469	2016
8) U. C. Hasar, J. J. Barroso, G. Buldu, M. Bute, Y. Kaya, T. Karacali, and M. Ertugrul	Reference-plane-invariant effective thickness and electromagnetic property determination of isotropic metamaterials involving boundary effects	<i>IEEE J. Sel. Topics on Quantum Electronics</i>	Vol:21, no: 4, 4700211	2015
7) U. C. Hasar, J. J. Barroso, M. Bute, Y. Kaya, M. E. Kocadagistan, and M. Ertugrul	Attractive method for thickness-independent permittivity measurements of solid dielectric materials	<i>Sens. Actuators A Phys.</i>	Vol:206, pp. 107-120,	2014
6) U. C. Hasar, M. Bute, J. J. Barroso, C. Sabah, Y. Kaya, and M. Ertugrul	Power analysis of multilayer structures composed of conventional materials and bianisotropic metamaterial slabs	<i>J. Opt. Soc. Am. B</i>	Vol:31, no: 5, pp. 939-947,	2014
5) U. C. Hasar, Y. Kaya, M. Bute, J. J. Barroso, and M. Ertugrul	Microwave Method for Reference-Plane-Invariant and Thickness-Independent Permittivity Determination of Liquid Materials	<i>Review of Scientific Instruments</i>	Vol:85, no:1, 014705	2014
4) U. C. Hasar, J. J. Barroso, Y. Kaya, M. Bute, and M. Ertugrul	Simple procedure for robust and accurate complex permittivity measurements of low-loss materials over a broad frequency band	<i>Journal of Electromagnetic Waves and Applications</i>	Vol:28, no:8, 903-915	2014

3) U. C. Hasar, J. J. Barroso, Y. Kaya, M. Bute , and M. Ertugrul	Two-step numerical algorithm for complex permittivity retrieval of dielectric materials from reflection measurements	<i>Applied Physics A: Materials Science and Processing</i>	Vol:116 no: 4, 1701-1710	2014
2) U. C. Hasar, G. Buldu, M. Bute , J. J. Barroso, T. Karacali, M. Ertugrul	Determination of constitutive parameters of homogeneous metamaterial slabs by a novel calibration-independent method	<i>AIP Advances</i>	Vol:4, p. 107116	2014
1) U. C. Hasar, J. J. Barroso, Y. Kaya, M. Ertugrul, and M. Bute	Reference-plane invariant transmission-reflection method for measurement of constitutive parameters of liquid materials	<i>Sensors and Actuators A: Physical</i>	Vol:23, p. 346-354	2013

6. Conference Proceedings:

Authors	Title of Paper	Journal	Place	Date
8) M. Bute , U. C. Hasar and J. J. Barroso	Retrieval Parameters of Chiral Metamaterials With Proposed Crescent Shaped Split Ring Resonators	IEEE, International Microwave and Optoelectronics Conference	27-30 Aug., Brazil	2017
7) M. Bute , U. C. Hasar and A. Muratoglu	Chiral Metamaterial Absorber Composed of New Crescent Shaped Split Ring Resonators	IEEE, 4th International EMC Turkey Conference	24-27 Sep, METU, Turkey	2017
6) U. C. Hasar, M. Bute and A. Muratoglu	Coupling Analysis of Resonating Metamaterial Slabs for The Role of EMC Problems	IEEE, 4th International EMC Turkey Conference	24-27 Sep, METU, Turkey	2017
5) M. Bute , U. C. Hasar and A. Muratoglu	New Approaches for Enhancements on Transmission of Electromagnetic Signals	IEEE 25th Signal Processing and Communications Applications Conference, SIU	15-18 May, Antalya, Turkey	2017
4) M. Bute and U. C. Hasar	Thickness-Invariant Permittivity Determination of Materials from Calibration Independent Measurements	IEEE, Middle East Conference on Antennas and Propagation (MECAP)	20-22 Sept., Beirut	2016
3) M. Bute and U. C. Hasar	Analyzing Coupling Effect of Adjacent Resonating Metamaterial Slabs	IEEE, International Conference for Students on Applied Engineering	20-21 Oct., Newcastle, UK	2016
2) U. C. Hasar, M. Bute , A. Muratoğlu, J. J. Barroso, T. Karacali and M. Ertugrul	Constitutive Parameters Determination of Bi-anisotropic Metamaterials using a Waveguide Method	IEEE, International Microwave and Optoelectronics Conference (IMOC)	03-06 NOV, Brazil	2015
1) M. Bute and U.C. Hasar	Electromagnetic properties of various pi-shaped bi-anisotropic composite metamaterials.	EMC 2013 Turkey Conference (National)	9-11 Sept., Istanbul, Turkey	2013

7. Participated Projects:

Project Name	Funding	Project No:	Job	Date
2) Novel approaches for improving the accuracy of reflection-transmission measurement techniques at microwave frequencies.	Scientific and Technological Research Council of Turkey, TUBITAK.	Project No: 114E495, Type: 1001	Student Researcher	2015 – 2017.
1) Unique determination of electromagnetic properties of various types of metamaterials using calibration-independent measurement techniques	Scientific and Technological Research Council of Turkey, TUBITAK.	Project No: 112R032, Type: 1001	Student Researcher	2013 - 2015.

8. Patents:

Authors	Title of Patent	Journal	Provisional Application Number	Date
3) M.Bute	Metamalzeme içeren bir solar enerji panel sistemi	Turkish Patent Office	2017/12/29	İnceleme Aşamasında.
2) U. C. Hasar, E. Kanca, and M.Bute	Anti-radyasyon Özelliğine Sahip bir Halı ve Üretim Yöntemi	Turkish Patent Office	2017/09/19	Araştırma Aşamasında.
1) M.Bute	Electronic Waistband for Infants to Relieve Their Gases	Turkish Patent Office	2014/15485	2014.